Materials Today 97 (2026) 103335

Contents lists available at ScienceDirect

Materials Today

journal homepage: www.elsevier.com/locate/mattod

Creep in multi-principal element materials — A review

Lia Amalia [a,1], Nathan Grain [a,1], Yanqing Su [b], Chelsey Z. Hargather [c], Shuozhi Xu [b,*], Peter K. Liaw [a,*]

[a] Department of Materials Science and Engineering, University of Tennessee, Knoxville, TN 37996, USA
[b] School of Aerospace and Mechanical Engineering, University of Oklahoma, Norman, OK 73019-1052, USA
[c] X Computational Physics Division, Los Alamos National Laboratory, Los Alamos, NM 87544, USA

A B S T R A C T

The ongoing push towards enhanced energy efficiency and reduced emissions has necessitated the creation of materials with superior performance, especially under extreme conditions. Modern industries, such as aerospace, energy production, and nuclear power, rely heavily on materials that can withstand elevated temperatures without compromising structural integrity. At these heightened temperatures, materials, even when subjected to mechanical stresses well below their yield strength, may experience slow deformation leading to eventual rupture — a phenomenon known as creep. With the expansive design space that comes with the high entropy concept and their reported excellent high temperature strength, multi-principal element materials (MPEMs) have attracted interest in the scientific community for high-temperature applications. This review offers a comprehensive examination of existing studies on creep in MPEMs, which includes multi-principal element−alloys, −bulk metallic glasses, −ceramics, and −superalloys, comparing published findings on MPEMs with pure elements, traditional alloys, bulk metallic glasses, and superalloys. The sub-topics covered include a comparison among different creep-testing methods, creep mechanisms, creep exponents, creep strain rates, activation volume, and creep-activation energy. Modeling efforts for predicting creep behavior of MPEMs are also reviewed. Methods for improving creep resistance by performing heat treatments and/or modifying microstructures are discussed. Overall, the current state of MPEMs has not yet surpassed the creep performance of commercial alloys. Finally, directions for future efforts are suggested, such as experimenting in various controlled environments, expanding the number of compositions tested, exploring advanced manufacturing techniques, and using machine-learning to predict creep properties based on compositions and microstructures.

Abbreviations: A, annealing; AG, aging; AI, artificial intelligence; AlN, aluminum nitride; AM, additive manufacturing; AMEA, amorphous medium-entropy alloy; AODR, argon-oxygen decarburization refining; B, Berkovich (indenter); B2, B2 ordered BCC phase; BCC, body-centered cubic; BM, ball milling; BMG(s), bulk metallic glass(es); BN, boron nitride; C, casting (fabrication); CALPHAD, CALculation of PHAse Diagrams; CCA(s), compositionally complex alloy(s); CNN, convolutional neural network; Com, compression; CONTIN, continuous regularization technique for inverse problems; CP, crystal plasticity; CR, cold rolling; CR80, cold rolling (80% reduction); CR90, cold rolling (90% reduction); CRSS, critical resolved shear stress; CSM, cooperative shear model; CSRO, chemical short-range order; CTC, cryogenic thermal cycling; d, diamond (Berkovich tip); DC, drop casting; DCMS, direct current magnetron sputtering; DFT, density functional theory; DMA, dynamic mechanical analysis; DS, directional solidification; DSR, directional structural relaxation; EAF, electric-arc furnace; FCC, face-centered cubic; GB(s), grain boundary/boundaries; GFA, glass-forming ability; H, homogenizing; HCP, hexagonal close-packed; HE, hot extrusion; HEA(s), high-entropy alloy(s); HESA, high-entropy superalloy; HF, hot forging; HIP, hot-isostatic pressing; HR, hot rolling; HPT, high-pressure torsion; kMC, kinetic Monte Carlo; L12, $L1_2$ ordered FCC phase; L21, $L2_1$ ordered phase; LCO, local chemical order; LF, ladle furnace; LPBF, laser powder bed fusion; MD, molecular dynamics; MEA, medium-entropy alloy; ML, machine learning; MLP, multi-layer perceptron; MPEA(s), multi-principal element alloy(s); MPEBMG(s), multi-principal element bulk metallic glass(es); MPEC(s), multi-principal element ceramic(s); MPEM(s), multi-principal element material(s); MPESA(s), multi-principal element superalloy(s); MS, magnetron sputtering; N, nanoindentation; ODS, oxide dispersion strengthening; PA, peak aging; PC, pour casting; PLB, power-law breakdown; RF, random forest; RMPEA(s), refractory multi-principal element alloy(s); RT, room temperature; s, sapphire (Berkovich tip); SA, solution annealing; SC, suction casting; SEM, scanning electron microscopy; SFE, stacking fault energy; SHL, superheated liquid; SHS, self-propagating high-temperature synthesis; SLM, selective laser melting; SOC, self-organized critical state; SPC, spark-plasma compacting; Sph, spherical (indenter); SPS, spark-plasma sintering; SRO, short-range order; SRC, stress reduction creep; SRJT, strain-rate-jump test; SRMS, single roller-melt spinning; SRT, stress relaxation test; ST, solution treatment; STZ, shear transformation zone; SWMS, single-wheel melt-spinning; T, tension; TFMG, thin-film metallic glass; T_g, glass transition temperature; TTZ, tension transformation zone; VAM, vacuum-arc melting; VIM, vacuum-induction melting; WSTZ, energy barrier of an STZ upon yielding; γ, gamma (matrix phase, FCC in γ/γ' superalloys); γ', gamma prime precipitate ($L1_2$ in γ/γ' superalloys).

* Corresponding authors.
E-mail addresses: shuozhixu@ou.edu (S. Xu), pliaw@utk.edu (P.K. Liaw).
[1] Co-first authors.

https://doi.org/10.1016/j.mattod.2026.103335
Received 27 December 2025; Received in revised form 27 March 2026; Accepted 13 April 2026

Introduction

Since 2004, the high-entropy alloys (HEAs), compositionally complex alloys (CCA), or multi-principal element alloys (MPEAs) concept, which was first introduced by Yeh [1] and Cantor [2] as a method to form random solid-solution materials, has gained popularity in research. Generally, MPEAs usually consist of three or more elements in concentrations ranging from 5 to 35 atomic percent, while systems described as HEAs have a configurational entropy larger than 1.5R, where R is the gas constant (R = 8.31 J/K-mol) [3]. In recent years, the design principles based on the high-entropy concept for alloy systems have evolved to a less restrictive definition, for example having non-equimolar compositions [4], consisting of three elements [5,6], and expanding from transition metals to refractory elements (called RMPEAs) [7,8] and other elemental groups [9–12]. The high-entropy concept has been expanded and applied to design multi-principal element ceramics (MPECs) to improve the high temperature performance [13–15]. The high-entropy concept is also utilized in designing multi-principal element superalloys (MPESAs) to optimize the strength, low density, and microstructural stability between matrix and precipitates [16–19]. Furthermore, in multi-principal element bulk metallic glasses (MPEBMGs), the high entropy concept is applied in bulk metallic glass (BMG) design to increase the ductility and maintain the strength [20–24]. For these reasons, multi-principal element materials (MPEMs) serve as a more inclusive term to classify the newly developed systems such as MPEAs, MPECs, MPESAs, and MPEBMGs.

The mechanical behavior of many types of MPEMs has been studied progressively since their inception in 2004 [1,2,20,25]. However, the studies on creep behavior of MPEMs are relatively scarce. Creep behavior is a crucial property to evaluate the lifetime of a material under certain applied stress and temperature conditions that ensure safety during service. Creep behavior can be tested by several methods, such as uniaxial tension and compression [26], stress relaxation [27], stepwise-loading [28], and nanoindentation techniques using different types of indenters [11,29–38]. For each test, stress is applied at a certain temperature until a sufficient material response is observed. In the case of nanoindentation, this is referred to as the holding time.

To demonstrate the rapidly expanding interest in creep of MPEMs, the number of relevant citations and publications is presented in Fig. 1. In the last several years, many publications reviewing MPEMs are focused on the high-entropy concept [8,39,40], computational work [41], mechanical behavior [25,42], corrosion behavior [43,44], high-temperature applications [45–48], and other applications [49–51]. However, the review on creep behavior of MPEMs has been limited to the CoCrFeMnNi system and/or its derivatives [42,52] and has not been expanded to other systems. A recent review paper on creep expanded the MPEAs covered to include alloys with face-center cubic, body-centered cubic, and multi-phase alloy systems but did not go beyond that [248]. In this review paper, the creep behavior of MPEMs, which include MPEAs, MPECs, MPEBMGs, and MPESAs, that has been reported over the past decade is summarized. Among the 86 reviewed compositions of MPEAs in this paper, only 7 of them are refractory element-based MPEAs. The rest are from the CoCrNi-family. As a result, the creep trends discussed in this review are most robust within CoCrNi-family space and extrapolation of conclusions to other MPEA families should be made with care. To increase comparability between material families, efforts were made to normalize the creep data. This work uniquely highlights the effects of material design on creep behavior under different testing methods. The creep mechanisms and the evidence discussed as proposed by the original reported studies were summarized in the present work. The large data set is broken into sections and compared based on the presented creep deformation mechanisms. Additionally, the creep data is organized based on the different creep testing techniques, and the effects are also discussed to give insight into the appropriate test methods for future creep experiments. This work also uniquely covers computational work on creep behavior and high-temperature deformation related to creep, providing insight on recent progress on computational approaches for high-temperature applications. Furthermore, this review is a timely response to the Genesis Mission announced by the US Department of Energy in November 2025 [249]. The Genesis Mission issued 26 challenges to the nation related to science and technology, with the goal of using artificial intelligence (AI) to connect experimental facilities, supercomputers, large datasets, and scientific experts. The data in this review has been tabulated and normalized in a way that responds to the need to accelerate materials discovery for energy-related applications. The data could be useful in enabling AI approaches to materials design.

Creep stages in MPEAs, MPESAs, and MPECs

Typical creep responses of metallic and ceramic materials include instantaneous deformation (Stage I), steady-state creep (Stage II), and accelerated creep (Stage III) [53]. By plotting creep strain versus time, the slope ($d\varepsilon/dt$) gives the creep strain rate, where $d\varepsilon/dt$ is the

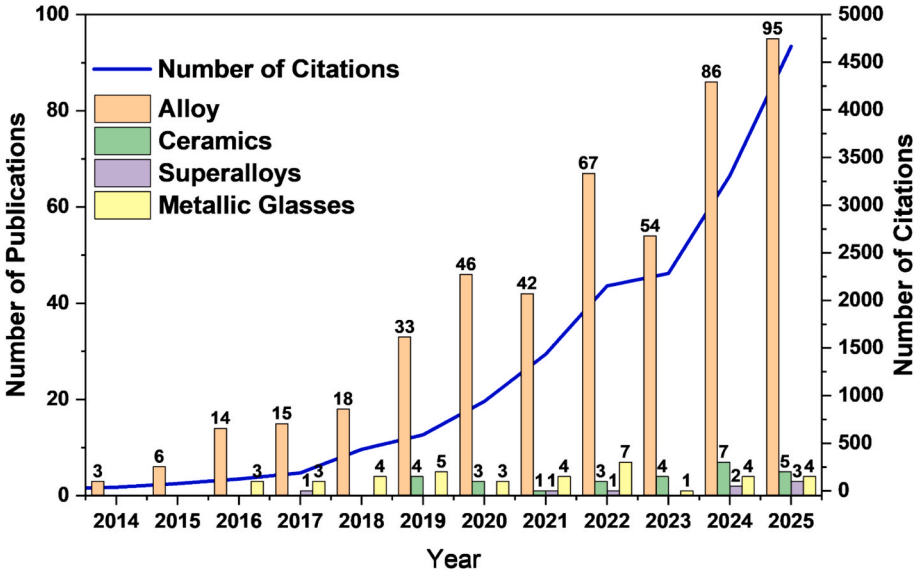

Fig. 1. Number of publications and citations of creep studies on MPEMs from 2011 to 2025 (obtained from Clarivate™ (Web of Science™) on March 23th, 2026).

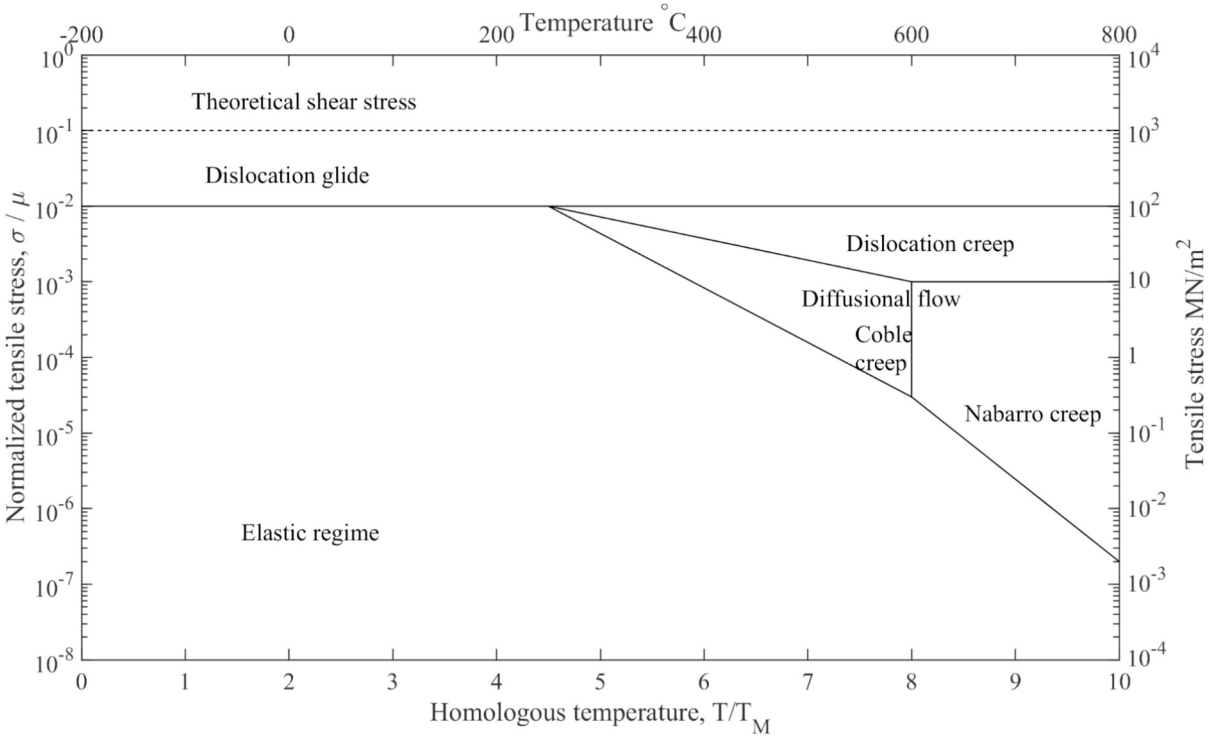

Fig. 2. Creep mechanism of typical crystalline material over a range of temperature and stress. [56].

instantaneous change in strain with respect to the instantaneous change in time. In Stage I, the creep rate increases then decreases as strain hardening occurs at the later stage of instantaneous deformation. In Stage II, a constant creep rate occurs due to a balance of strain hardening ($h = \partial\sigma/\partial\varepsilon$) and recovery by annihilation and rearrangement of dislocations ($r = -\partial\sigma/\partial t$), where $\partial\sigma/\partial\varepsilon$ is the instantaneous change in stress with respect to the instantaneous change in strain, and $\partial\sigma/\partial t$ is the instantaneous change in stress with respect to the instantaneous change in time. A constant creep rate occurs when the strain-hardening rate is low enough while the recovery rate is high enough ($\dot{\varepsilon} = r/h$), where $\dot{\varepsilon}$ is the creep strain rate. The average value of the creep rate during Stage II is known as the minimum creep strain rate or steady-state creep rate. The steady-state creep rate depends on the applied stress and temperature while both the applied stress and test temperature are kept constant as a function of increasing creep strain and time. For that reason, the minimum creep rate is important for designing materials for elevated-temperature applications [54,55]. Stage III occurs when there is a sufficient cross sectional area reduction due to necking or formation of internal voids [26]. The steady-state creep-strain rate is given by Eq. (1), where A is a constant, σ is the applied stress, E is the elastic modulus, n is the stress exponent, Q_c is the activation energy, k is Boltzmann constant, and T is the temperature [26].

$$\dot{\varepsilon} = A(\sigma/E)^n exp(-Q_c/kT) \quad (1)$$

Creep behavior is material-dependent and depends on the temperature and applied stress during the test. As illustrated in Fig. 2, creep typically occurs outside the elastic-deformation regime, which depends on the homologous temperature (T/T_m) and applied stress. The stress exponent (n) can be obtained by plotting log $\dot{\varepsilon}_s$ versus log σ of data from the same testing temperature. Meanwhile, the activation energy (Q_c) can be obtained by plotting ln $\dot{\varepsilon}_s$ versus $1/T$ of data from the same applied stress. The activation energy is the minimum energy required to activate a certain mechanism, which could vary in different materials. Based on the value of n and Q, the creep mechanism can be inferred. There are several classical creep mechanisms, such as the diffusional creep ($n = 1$), grain boundary (GB) sliding, or migration ($n = 2$), creep by dislocation interaction ($n = 3$ up to 8), and power-law-breakdown ($n > 7$), which deviates from the classical creep mechanisms. These creep mechanisms will be discussed further in the next sections.

Creep stages in MPEBMGs

Metallic glasses are supercooled liquids which form an amorphous structure. Metallic glasses are studied due to their high hardness, specific strength, corrosion resistance, oxidation resistance, and wear resistance [20]. However, due to their inability to undergo homogeneous plastic deformation, metallic glasses are very brittle under tensile load [20]. Due to their amorphous microstructure, metallic glasses deform by forming shear transformation zones (STZs) [57]. The multi-principal element alloy design was incorporated on metallic glasses to find a metallic glasses composition with high strength and ductility [22–24]. Table 1 summarizes the experimental conditions, composition, and resulting creep response of each metallic glass material tested.

At room temperature, all BMGs typically deform by STZs activation [58] and shear-band propagation due to the lack of long-range order [20]. This behavior is different from traditional metallic alloys where deformation is typically accommodated by dislocations. STZs then could cascade and align into planar shear bands. After an STZ is activated, the atom clusters distort under shear, absorbing energy to allow plasticity [58]. However, the distortion also softens nearby locations, making for easier crack formation and propagation [58]. Cracks in BMGs propagate by breaking up local atomic clusters. Under tensile loading, BMGs typically fail catastrophically after forming a single shear band. The shear band propagates rapidly due to the lack of distributed plasticity and the localized soft zones formed by activated STZs. Jiang et al. [59] proposed a tension transformation zone (TTZ) where the atomic clusters break directly under tensile loading. The break is due to a high stress near the crack tip, and the crack propagates faster than the plastic relaxation of the material. However, some studies that used high strain rates did not agree with this theory [60].

During elevated-temperature and creep deformation, typically above 0.6 of its glass transition temperature (T_g), BMGs deform by STZs

Table 1
Creep mechanisms of various MPEBMGs under different testing and fabrication methods.

Composition	Testing Method	Fabrication method	Phase	Grain size [μm]	Temperature range [K]	Stress range [MPa]	Minimum Creep Rate [/s]	Stress exponent	Strain rate sensitivity	Creep mechanism	Load Rate [μN/s]	Ref
Tension												
$Pd_{20}Pt_{20}Cu_{20}Ni_{20}P_{20}$	T	SWMP	Amorphous		503	25 – 125			0.78, 0.51, 0.83 for 3 stages at 100 MPa, over time	Anelastic deformation governed by activation of deformation units (tiny groups of atoms that can temporarily rearrange under stress and cause time-dependent, recoverable creep, same as STZ); influenced by aging.		[121]
$La_{30}Ce_{30}Ni_{10}Al_{20}Co_{10}$	T	VAM + SC + SRMS	Amorphous		358 373 388	25 – 100 25 – 100 25 – 100	4×10^{-6} to 1×10^{-5}	1.4 1.43 1.44		Three-stage power-law relaxation; STZ-based: stochastic activation −> interaction of STZs −> quasi-steady state. Increasing temperature: anelastic and transition to viscous-like quasi-steady-state creep, because isolated STZ become interacting STZ at higher T (403 K), causing permanent strain.		[63]
$La_{30}Ce_{30}Ni_{10}Al_{20}Co_{10}$	T	VAM + SRMS	Amorphous		363 K (~90 °C), below T_g (438 K)	100				Three-stage STZ activation: stochastic → contiguous interplay → quasi-steady-state permeation; affected by physical aging and cyclic loading. At short creep time, independent STZ activates. Then STZ interacts as time goes by and at long times, STZ network is formed, causing viscoplastic flow. Aging makes it harder to activate STZ.		[122]
$Al_{20}Ce20La_{20}Ni_{20}Y_{20}$	T	SWMS	Amorphous		303 – 483	80				Two-stage activation energy behavior modeled by Kelvin model. Creep is controlled by evolution and retardation of smaller internal defects due to activation of short relaxation times.		[129]
ZrTiCuNiBe (H1)	T (DMA, 5 MPa)	SC	Amorphous		Near T_g: ~691 – 732	5				High viscosity in supercooled region (~2.8×10^{10} Pa·s);		[138]

(*continued on next page*)

Table 1 (*continued*)

Composition	Testing Method	Fabrication method	Phase	Grain size [μm]	Temperature range [K]	Stress range [MPa]	Minimum Creep Rate [/s]	Stress exponent	Strain rate sensitivity	Creep mechanism	Load Rate [μN/s]	Ref
										higher fragility and crystallization activation energy than Vit1. Sluggish kinetics during reheating leads to high thermal stability.		
ZrTiHfCuNiBe (H2)	T (DMA, 5 MPa)	SC	Amorphous		Near T_g: ~681 – 743	5				High viscosity in the supercooled region; strong glass. Lower GFA than Vit1 despite higher thermal stability. Lower viscosity in the superheated region promotes crystallization upon cooling.		[138]
Composition	**Testing Method**	**Fabrication method**	**Phase**	**Grain size [μm]**	**Temperature range [K]**	**Stress range [MPa]**	**Minimum Creep Rate [/s]**	**Stress exponent**	**Strain rate sensitivity**	**Creep mechanism**	**Load Rate [μN/s]**	**Ref**
Compression												
$Ti_{16.7}Zr_{16.7}Hf_{16.7}Cu_{16.7}Ni_{16.7}Be_{16.7}$	Com	SC	Amorphous		657 – 681	Not specified (stress-jump and relaxation)	3×10^{-3} to 1×10^{-2}			Viscosity-controlled flow, Newtonian at low strain rate, non-Newtonian at high strain rate. Based on the free volume model. Stress relaxation is linked to atomic V* and heterogeneity.		[123]
Composition	**Testing Method**	**Fabrication method**	**Phase**	**Grain size [μm]**	**Temperature range [K]**	**Maximum Load [mN]**	**Minimum Creep Rate [/s]**	**Stress exponent**	**Strain rate sensitivity**	**Creep mechanism**	**Load Rate [μN/s]**	**Ref**
Nanoindentation												
$Ti_{41}Zr_{25}Be_{34}$	N	AM + SC	Amorphous		RT	5, 10			0.0115 – 0.0136	Smallest STZ volume and low activation energy leading to easily activated STZs. Higher creep compliance and displacement.	1,000	[120]
$Ti_{41}Zr_{25}Be_{28}Fe_6$	N	AM + SC	Amorphous		RT	5, 10			0.00853 – 0.0087	STZ volume and activation energy lead to better creep resistance due to higher WSTZ and possible bonding effects (negative heat of mixing with Ti/Zr).	1,000	[120]
$Ti_{41}Zr_{25}Be_{28}Al_6$	N	AM + SC	Amorphous		RT	5, 10			0.00627 – 0.0076	Largest STZ volume and highest activation energy leading to smallest creep strain rate sensitivity, creep displacement, and compliance. Highest T_g	1,000	[120]

(*continued on next page*)

Table 1 (*continued*)

Composition	Testing Method	Fabrication method	Phase	Grain size [μm]	Temperature range [K]	Stress range [MPa]	Minimum Creep Rate [/s]	Stress exponent	Strain rate sensitivity	Creep mechanism	Load Rate [μN/s]	Ref
										and Poisson's ratio leads to enhanced STZ barrier.		
$Ti_{41}Zr_{25}Be_{28}Ni_6$	N	AM + SC	Amorphous		RT	5, 10			0.0104 – 0.0123	STZ volume and activation energy lead to moderate free volume; less effective than Al, but better than Fe.	1,000	[120]
$Gd_{55}Co_{20}Al_{24.5}Si_{0.5}$	N	SC	Amorphous + Nano-crystals (post-CTC)	3 – 5 nm (nanocrystals after 20 × CTC)	RT	50				Nanoscale anelastic and viscoplastic deformation modeled by Maxwell-Voigt equations. Creep controlled by relaxation dynamics in structurally heterogeneous zones.		[125]
$Ti_{20}Zr_{20}Hf_{20}Be_{20}Cu_{20}$	N	SC	Amorphous		RT	5			6.02×10^{-3} to 9.61×10^{-3}	Indentation creep modeled by generalized Kelvin model; low m-values indicate strongly localized shear flow; free volume generation during loading contributes to deformation.	250 500 1,000	[126]
$Ti_{20}Zr_{20}Hf_{20}Be_{20}Cu_{10}Ni_{10}$	N	SC	Amorphous		RT	5			3.98×10^{-3} 4.37×10^{-3} 7.86×10^{-3}	Lower m-values than Cu_{20} alloy; enhanced creep resistance due to Ni alloying; increased ΔS_{mix}, δ, and E contribute to suppression of atomic motion and densified structure.	250 500 1,000	[126]
$Cu_{29}Zr_{32}Ti_{15}Al_5Ni_{19}$	N	SC	Amorphous		RT	100	7×10^{-5}			Kelvin model fit; transient and steady-state creep stages observed; creep attributed to viscoplastic flow; compliance increases with time due to structural softening.	5,000	[127]
$Ti_{16.7}Zr_{16.7}Hf_{16.7}Cu_{16.7}Ni_{16.7}Be_{16.7}$	N	DC	Amorphous		RT	50			1.96×10^{-3} 2.34×10^{-3} 4.5×10^{-3}	Plastic deformation is governed by shear band nucleation and STZ activation. Strain localization decreases with increasing loading rate. SOC behavior confirmed by stress drop and STZ volume analysis. Larger STZ volume and serration size at low strain rate.	500 5,000 50,000	[128]

(*continued on next page*)

Table 1 (*continued*)

Composition	Testing Method	Fabrication method	Phase	Grain size [μm]	Temperature range [K]	Stress range [MPa]	Minimum Creep Rate [/s]	Stress exponent	Strain rate sensitivity	Creep mechanism	Load Rate [μN/s]	Ref
TaTiZr (AMEA)	N	MS	Amorphous		RT	10				Creep response fitted with Maxwell-Voigt model. Increased annealing temperature leads to stronger bonding and structural heterogeneity. Relaxation time spectrum shifts to shorter times, with reduced soft defect activation. Creep resistance improves with annealing.	2,000	[130]
$Cu_{36}Zr_{48}Al_8Ag_8$	N	SC	Amorphous		RT	25		1.7 – 12		Stress exponent strongly affected by curve-fitting region, structural inhomogeneity, serrations, and displacement rate. Creep occurs via STZ-mediated homogeneous or serrated flow.	10	[131]
$Zr_{64.13}Cu_{15.75}Ni_{10.12}Al_{10}$	N	SC	Amorphous		RT	70				Low $\dot{\varepsilon}_s/P_{max}$ suggests moderate resistance. Pop-in distribution used to derive WSTZ and STZ volume.		[132]
$Fe_{68}Mo_4Cr_1Y_5B_{22}$	N	SC	Amorphous		RT	175				High hardness and shear modulus. Very low $\dot{\varepsilon}_s/P_{max}$, WSTZ, STZ volume.		[132]
$Co_{39.78}B_{26.2}Ni_{21.42}Si_{7.8}Ta_{4.8}$	N	SC	Amorphous		RT	230				Similar to Fe-BMG; very low J and m. WSTZ and STZ volume. High creep resistance due to large WSTZ and small m.		[132]
$(Zr_{0.6336}Cu_{0.1425}Ni_{0.1012}Al_{0.12})_{97.4}Er_{2.6}$	N	SC	Amorphous		RT	4 – 10				Higher cooling rate introduces more free volume, enhancing shear band activity. Indentation size effect observed. Material softens with increasing cooling rate due to excess free volume.	500	[133]
$Zr_{50}Cu_{40}Al_{10}$	N	PC	Amorphous		RT	200			0.031	Plasticity originates from delayed plasticity and flow defect softening. Higher free volume leads to faster creep depth accumulation. Lower	1,500 12,000 100,000	[134]

(*continued on next page*)

Table 1 (*continued*)

Composition	Testing Method	Fabrication method	Phase	Grain size [μm]	Temperature range [K]	Stress range [MPa]	Minimum Creep Rate [/s]	Stress exponent	Strain rate sensitivity	Creep mechanism	Load Rate [μN/s]	Ref
										STZ volume, higher T_c and creep depth h_0 than relaxed state.		
$Zr_{50}Cu_{40}Al_{10}$	N	PC + annealed	Amorphous		RT	200			0.018	Higher hardness and STZ volume after relaxation. Less delayed plasticity, shorter relaxation time, and smaller creep depth. Soft zones reduced, showing denser packing and higher viscosity.	1,500 12,000 100,000	[134]
$(Co_{0.7}Fe_{0.3})_{0.68}B_{0.219}Si_{0.051}Nb_{0.05}$ (Cu_0)	N	CM	Amorphous		RT	50		29 19 13 11 7 5 6		High stress exponent at low rate indicates inhomogeneous plastic flow. Localized shear bands with higher pile-up; excess free volume trapped locally, impeding homogeneous creep.	100 500 1,000 5,000 10,000 50,000 100,000	[135]
$(Co_{0.7}Fe_{0.3})_{0.68}B_{0.219}Si_{0.051}Nb_{0.05}$ + 0.5 at.% Cu ($Cu_{0.5}$)	N	CM	Amorphous + nanoscale Co(Fe)-rich clusters		RT	50		19 14 12 6 5 4 3		Cu induces weakly bonded regions that enhance free volume generation. More homogeneous creep with multiple shear bands and lower pile-up. High loading-rate sensitivity; stable flow enabled by structural heterogeneity.	100 500 1,000 5,000 10,000 50,000 100,000	[135]
$La_{57}Co_{18}Al_{25}$	N	MS	Amorphous		RT	0.75			0.022 – 0.385	Primary creep governed by STZs with high WSTZ and U; steady-state creep at long holding time shows more homogeneous deformation. Larger m at long holding time indicates increased deformation stability. High creep rate and displacement.		[136]
$Zr_{55}Cu_{15}Ni_{13}Al_{17}$	N	MS	Amorphous		RT	1.3			0.18 – 0.29	Intermediate creep stability. WSTZ/kT and STZ volume decrease with holding time. Creep becomes more homogeneous with time.		[136]
$Ni_{60}Nb_{40}$	N	MS	Amorphous		RT	3.1			0.10 – 0.22	Moderate STZ volume and activation energy; smaller creep rate and higher H, reduced deformation instability		[136]

(*continued on next page*)

Table 1 (*continued*)

Composition	Testing Method	Fabrication method	Phase	Grain size [μm]	Temperature range [K]	Stress range [MPa]	Minimum Creep Rate [/s]	Stress exponent	Strain rate sensitivity	Creep mechanism	Load Rate [μN/s]	Ref
										with increasing holding time.		
$W_{68}Ru_{25}B_7$	N	MS	Amorphous		RT	2.5			0.09 – 0.20	Highest hardness and modulus; lowest creep rate; STZ volume drops below 0.25 nm^3 at long holding time; very stable creep deformation with high resistance to strain localization.		[136]
$Zr_{50}Cu_{40}Al_{10}$	N	CM	Amorphous		RT	10		6.4	0.156	Intermediate creep rate; moderate microstructural heterogeneity. Creep fits Kelvin model with h0 = 81.05 nm, Tc = 1.62 s. STZ volume ~ 2.02 nm^3. Displacement bursts moderately apparent.	100	[137]
$Zr_{50}Cu_{40}Al_{10}$	N	CM + annealed	Amorphous		RT	10		7.1	0.141	Lowest creep rate and STZ activity. Most pronounced displacement bursts, clustered dynamics.	100	[137]
$Zr_{50}Cu_{40}Al_{10}$ (CR80)	N	CM + Cold rolling 80%	Amorphous		RT	10		6.1	0.164	Increased creep depth. Microstructure shows more heterogeneity, smaller displacement bursts, clustered dynamics.	100	[137]
$Zr_{50}Cu_{40}Al_{10}$ (CR90)	N	CM + Cold rolling 90%	Amorphous		RT	10		6	0.167	Highest creep depth (h0 = 87.22 nm), Tc = 2.22 s. STZ volume ~ 1.78 nm^3. Displacement bursts are dense but smallest. Microstructure is highly heterogeneous.	100	[137]

Table 2
Summary of results which show the lattice diffusion or grain boundary diffusion creep mechanisms (n ≈ 1).

Composition	Testing Method	Fabrication method	Phase	Grain size [μm]	Temperature range [K]	Stress range [MPa]	Minimum Creep Rate [/s]	Stress exponent	Creep mechanism	Ref
Compression										
Multiprincipal Element Alloys (MPEA)										
MoNbTaVW	Com	VAM	BCC	138	973	130 – 520	4×10^{-9} to 2×10^{-8}	1.2	Dislocation pipe diffusion-controlled creep at lower temperatures and lattice diffusion controlled by Mo at higher temperatures.	[119]
					1,023	130 – 520	9×10^{-9} to 4×10^{-8}	1.3		
					1,073	130 – 520	2.5×10^{-8} to 1.1×10^{-7}	1.2		
					1,123	130 – 400	1×10^{-7} to 4×10^{-7}	1.3		
					1,173	130 – 400	6×10^{-7} to 1.5×10^{-6}	1		
CoCrFeMnNi + ODS (Y_2O_3 + Ti)	Com	BM − SPC	FCC + oxides	0.4	973	32 – 48	1×10^{-9} to 2×10^{-9}	1.8	Lattice diffusion at low stresses and dislocation controlled by oxide interaction at high stresses after subtracting with threshold stress.	[68]
					1,023	30 – 35	2×10^{-9} to 2.5×10^{-9}	1.8		
					1,073	10 – 32	9×10^{-10} to 7.5×10^{-9}	1.8		
Composition	**Testing Method**	**Fabrication method**	**Phase**	**Grain size [μm]**	**Temperature range [K]**	**Maximum Load [mN]**	**Minimum Creep Rate [/s]**	**Stress exponent**	**Creep mechanism**	**Ref**
Nanoindentation										
Multiprincipal Element Alloys (MPEA)										
CoCrFeMnNi	N	VAM + DC + HIP ¼ turn	FCC	0.049	RT	10, 50, 100	10^{-9}	1.03	GB diffusion	[104]
CoCrFeMnNi	N	VAM + DC + HIP 2 turns	FCC	0.033	RT	10, 50, 100	10^{-9}	1.3	GB diffusion	[104]
$Ni_{34.1}Co_{33.9}Cr_{20.9}Mo_{10.2}Ti_{0.9}$ (NG-42)	N	mechanical grinding	FCC	0.042	973	80 – 90	10^{-4}	1.3	Diffusional creep	[72]

activation [61]. With increasing temperature, more STZs and free volumes are activated and created, respectively, which enables more homogeneous and viscoelastic flow. The creep curves of BMGs (strain versus time) generally exhibit three stages, including a transient stage (a high creep rate), secondary stage (a quasi-steady-state creep), and tertiary stage (an accelerated creep and then failure) [61]. At lower stresses or moderate temperatures, the tertiary stage may be absent because of the limited structural relaxation.

In the transient creep stage, the STZs with the lowest activation energy will activate first. Due to STZs activation, each local shear event causes local changes in the structure where the structure relaxes and reconfigures to a lower energy state, which means a reduction of free volume [62]. This process will eventually use up the available STZs, leading to a creep-rate reduction, and the creep process will enter the secondary creep stage. During the secondary creep stage, the rate of STZ activation and relaxation will be at a dynamic equilibrium, leading to a quasi-steady-state creep [63]. At this stage, STZs may interact with other STZs, which will affect the creep behavior [63]. During this stage, excess free volumes might be created, which could become the initiation site for a crack to form, and the creep process would enter the tertiary stage [61].

Creep mechanisms in multi-principal element material systems

The creep mechanisms of commercial materials and their multi-principal element material counterparts follow the same mechanisms, which are diffusion, GB sliding, dislocation controlled, and power-law breakdown. The creep mechanism of bulk metallic glasses is different from other materials such as alloys and ceramics because they are amorphous and deform by STZs as has been discussed in the previous section. The following subsections summarize the reported stress exponents and creep mechanisms from the literature. These values and reasonings may have been obtained using different experimental methods, e.g., uniaxial creep, stress relaxation, and nanoindentation creep, which probe different stress state and deformation volumes. Therefore, the creep exponent values and mechanisms discussed below are presented as method-specific reported descriptors and are used to organize trends within each testing method rather than to imply direct quantitative equivalence between nanoindentation and uniaxial creep parameters.

Lattice diffusion (Nabarro-Herring creep) and GB diffusion (Coble creep)

Creep by self-diffusion in the lattice is widely known as Nabarro-Herring creep [64–66]. Lattice-diffusion creep usually occurs at relatively high temperatures (around $> 0.65T/T_m$) and low applied stresses ($\sigma/\mu < 10^{-4}$, μ is the shear stress). An applied stress creates excess vacancies along the GBs perpendicular to the load in the tensile direction while vacancy depletion occurs on the GBs undergoing a compressive load. The result is that vacancies flow from the tensile-loaded region to compression-loaded region [64]. Diffusion also occurs in the GBs and is usually faster due to more open lattice sites than in the lattice. Creep dominated by GB diffusion is known as Coble creep [67]. Typically, lattice diffusion and GB diffusion creep have a stress exponent of $n = 1$. Results that show this creep mechanism in MPEAs are summarized in Table 2. Notably, none of the MPECs or MPESAs reviewed reported a stress exponent of $n \approx 1$.

Dobes et al. [68] and Hadraba et al. [69] reported the effect of oxide-dispersion strengthening (ODS) on CoCrFeMnNi, using compression and tension creep tests, respectively. As reported by Dobes et al. [68], the incorporation of ODS lowers the creep rate and alters the creep mechanism of CoCrFeMnNi-ODS ($n = 1.8$, lattice diffusion) [68] especially at stress levels of 10 to 50 MPa compared to CoCrFeMnNi ($n = 6.3$, dislocation motion) [68]. At an applied stress of 40 to 100 MPa, creep

Table 3
Summary of results which show the grain boundary sliding creep mechanism (n ≈ 2).

Composition	Testing Method	Fabrication method	Phase	Grain size [μm]	Temperature range [K]	Stress range [MPa]	Minimum Creep Rate [/s]	Stress exponent	Strain rate sensitivity	Creep mechanism	Load Rate [μN/s]	Ref
Tension/Compression												
Multiprincipal Element Alloys (MPEA)												
$Al_{0.4}CoCrFeMnNi$	T	VIM − H − CR	FCC + BCC	30 – 85	923	80 – 130	2×10^{-8} to 7×10^{-8}	1.6		Viscous glide		[82]
					973	40 – 110	1.8×10^{-8} to 2×10^{-7}	2.2				
CoCrFeMnNi	T	VAM + DC + CR + A	FCC + Mn_3O_3 and MnO_2 (oxides in deformed only)	12 – 32	1,123	7 – 31	6.41×10^{-7} to 7×10^{-6}	2		Dislocation climb at high strain rates (Ni diffusion rate-controlled process), solute drag at low strain rates.		[101]
HfNbTaTiZr	T	VAM − DC − H − CR	BCC	98	1,253	10 – 60	1.1×10^{-7} to 8×10^{-6}	2		Coble creep		[113]
					1,373	5 – 20	6×10^{-7} to 2×10^{-5}	2				
Multi principal element ceramic (MPEC)												
(Hf-Ta-Zr-Nb)C	T	BM + SPS	Fm-3 m (NaCl-type structure)	5 – 25, ~12 average	1673 – 1873	150 – 300	2.18×10^{-9} to 7.56×10^{-8}	2.34 – 2.89		GB sliding/cracking, dislocation glide and climb, diffusion-controlled creep.		[14]
$(Hf_{0.2}Ta_{0.2}Ti_{0.2}Nb_{0.2}Zr_{0.2})C$	Com	SHS + SPS + A 2000C	Single phase with NaCl-type structure	4.03 – 5.24	1673 – 1873	200 – 300	4.97×10^{-9} to 6.13×10^{-8}	2.01 – 2.90		Combination of atomic diffusion, GB sliding, and dislocation slip. Dominant: dislocation slip.		[13]
$(Hf_{0.2}Ta_{0.2}Ti_{0.2}Nb_{0.2}Zr_{0.2})C$	Com	SHS + SPS + A 2100C	Single phase with NaCl-type structure	6.13 – 8.59	1673 – 1873	150 – 300	3.61×10^{-9} to 5.38×10^{-8}	2.14 – 2.59		Combination of atomic diffusion, GB sliding, and dislocation slip. Dominant: dislocation slip.		[13]
(Ti-Zr-Nb-Ta-Mo)C	Com	HP	Single − phase FCC carbide	3.66, 4.27 (crept)	1673 – 1873	200 – 300	2.13×10^{-8} to 2.74×10^{-6}	2.76 ± 0.31		Dominated by dislocation glide, GB sliding, and atom diffusion. C and Mo atoms contribute to diffusion. Sluggish lattice diffusion and high Peierls stress limit climb and enhance creep resistance.		[15]
Composition	**Testing Method**	**Fabrication method**	**Phase**	**Grain size [μm]**	**Temperature range [K]**	**Maximum Load [mN]**	**Minimum Creep Rate [/s]**	**Stress exponent**	**Strain rate sensitivity,**	**Creep mechanism**	**Load Rate [μN/s]**	**Ref**
Nanoindentation												
Multiprincipal Element Alloys (MPEA)												
$Al_{0.3}CoCrFeNi$	N	VAM	FCC	15 – 20	RT	150	2×10^{-4}	1.71	0.0048 0.0123 0.0213	Sluggish-diffusion and cooperative motion of several atoms induced by atomic size difference, retarding the velocity of dislocation glide.	0.2 1 5	[29]
CoCrFeMnNi	N	VAM − HPT 3	FCC	0.025	RT	20	10^{-4} to 10^{-5}	2.3		GB sliding	5,000	[38]

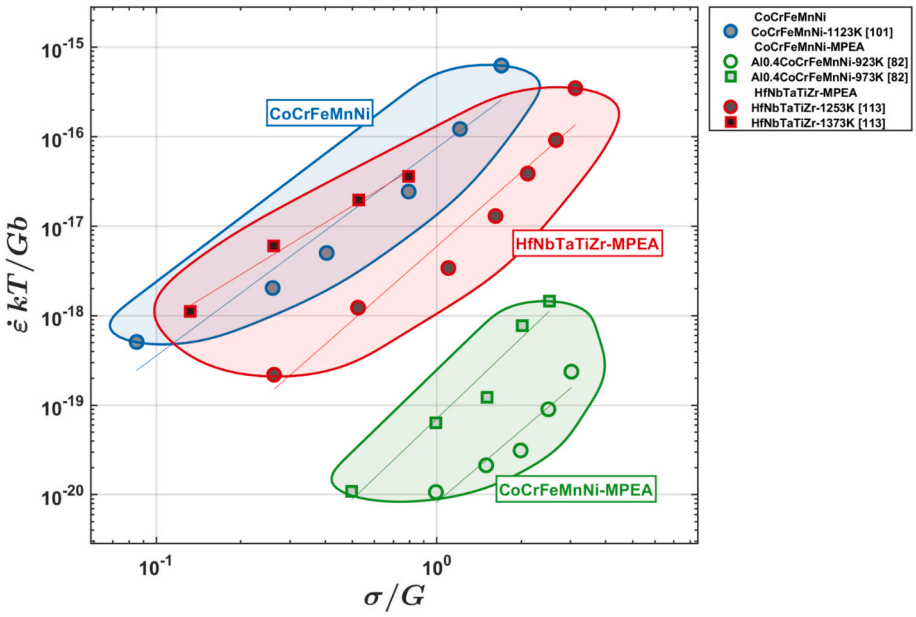

Fig. 3. Creep comparison of MPEAs with creep exponent, n = 2, obtained from uniaxial tension load.

behavior of CoCrFeMnNi-ODS (n = 13.2) involves the interactions between oxides with high-angle and low-angle dislocations, individual dislocations, and high-angle GBs, lowering the deformation kinetics, which improves creep resistance. Under tension, creep resistance of CoCrFeMnNi-ODS (n = 1.84) [69 50] is 99% lower than CoCrFeMnNi (n = 5.96) [69] at 30 MPa.

Grain-boundary sliding

GB sliding occurs when voids are formed due to a shear stress acting on the GBs [26]. Recovery occurs at the regions around the GBs because of the localization of high strain energy, which softens this region before further regions are affected [26,64]. Further deformation can be formed in the regions around the GBs, which results in the sliding of GBs. Creep by GB sliding typically has a stress exponent of $n = 2$ [26,64,70]. MPEAs and MPECs found to have $n \approx 2$ are summarized in Table 3 below. No MPESA reviewed reported a stress exponent in the range to indicate GB sliding as the primary creep mechanism. Fig. 3 plots the data from Table 3 that was able to be normalized. This includes normalizing the applied stress by the shear modulus and normalizing the creep strain rate by the test temperature, shear modulus, and Burgers vector.

Zhou et al. [38] reported the effect of high-pressure torsion (HPT) on the creep behavior of CoCrFeMnNi tested through nanoindentation containing a Berkovich diamond tip with each experiment repeated at five different positions. The stress exponent changes with the loading rate and decreases with increasing the rotation of HPT. The creep behavior changes from only dislocation creep to dislocation creep and GB sliding on HPT samples. The creep behavior changes due to the grain size changing from micro-sized to nano-sized grains after HPT. The strain rate and applied stress relationship can be described by Eq. (2) [71], and the empirical power-law-creep equation is given by Eq. (3) [37,71], with the applied stress given by Eq. (4) [37,71], where h is the instantaneous indenter displacement, B is a constant, Q is the activation energy, and P is the indentation load. Note that $24.5h^2$ is the area of the indenter.

$$\dot{\varepsilon} = 1/h\frac{dh}{dt} \tag{2}$$

$$\dot{\varepsilon} = B\sigma^n(-Q/RT) \tag{3}$$

$$\sigma \approx P/24.5h^2 \tag{4}$$

Then, using Eqs. (2) to (4), the creep exponent is calculated with Eq. (5).

$$ln\dot{\varepsilon} = nln(P/24.5h^2) + lnC \tag{5}$$

Zhang et al. [72] reported the effect of a surface-mechanical-grinding treatment on $Co_{33.9}Cr_{20.9}Mo_{10.2}Ni_{34.1}Ti_{0.9}$ to refine a surface-layer grain size to 42 nm and 9 nm. Creep tests using a Berkovich nanoindentation experiment at 873, 973, and 1,023 K revealed that having sufficiently small grain sizes such that in $Co_{33.9}Cr_{20.9}Mo_{10.2}Ni_{34.1}Ti_{0.9}$ with the 9 nm grain size ($n \geq 100$) could effectively stabilize GB networks and suppress GB sliding, making $Co_{33.9}Cr_{20.9}Mo_{10.2}Ni_{34.1}Ti_{0.9}$ with the 9 nm grain size capable of creep rates up to 9.5×10^{-7} /s at 1,036 MPa and 700 °C. Meanwhile $Co_{33.9}Cr_{20.9}Mo_{10.2}Ni_{34.1}Ti_{0.9}$ with the 42 nm grain size (n = 1.3) deformed by diffusional creep and has significantly higher creep rates of up to 5.6×10^{-4} /s at 100 MPa and 700 °C due to having larger ordinary high-angle GB density. $Co_{33.9}Cr_{20.9}Mo_{10.2}Ni_{34.1}Ti_{0.9}$ with the 9 nm grain size has a significantly lower GB diffusion coefficient of 2.2×10^{-19} m^2/s compared to $Co_{33.9}Cr_{20.9}Mo_{10.2}Ni_{34.1}Ti_{0.9}$ with the 42 nm grain size with diffusion coefficient of 0.81×10^{-15} m^2/s, tested in tension at 973 K for 100 h [72].

Fig. 3 shows the different creep behavior of creep tested with uniaxial tension method, taking into account the temperature normalized to the shear modulus and the Burgers vector versus the applied stress normalized to shear modulus. The lowest creep rate within this data population is exhibited by Al_xCoCrFeMnNi [82] alloys. This alloy system was creep tested at lower stress (40 – 120 MPa) and temperature range of 923 – 973 K and exhibited a creep exponent of n = 1.6 to 2, which is usually associated with grain boundary sliding mechanism. However, it was reported that due to the large grain size of 30 – 85 μm and TEM observations showing dilute density of straight dislocation segments, viscous glide mechanism is more likely to be the dominant creep mechanism in this creep test conditions.

The studies on MPECs that reported n all identified GB sliding as a creep mechanism [13–15]. For $(Hf_{0.2}Ta_{0.2}Ti_{0.2}Nb_{0.2}Zr_{0.2})C$, cracks forming at the grain boundaries are indicative of GB sliding, and additionally, dislocation slip was observed [13]. The resulting n is between 2.01 and 2.90 [13] for the different temperature ranges, meaning the combined creep mechanism calculated matches the observed microstructural effects. Similarly, (Hf-Ta-Zr-Nb)C was found to have a

Table 4
Summary of results which show the dislocation creep mechanisms ($3 < n < 8$).

Composition	Testing Method	Fabrication method	Phase	Grain size [μm]	Temperature range [K]	Stress range [MPa]	Minimum Creep Rate [/s]	Stress exponent (n)	Creep mechanism	Load Rate [μN/s]	Ref
Tension											
Multiprincipal-Element Alloys (MPEA)											
$Al_{0.15}CoCrFeNi$	SRT	VIM	FCC		923	80 – 140	2×10^{-8} to 1.3×10^{-7}	4.98	Cross-slip controlled dislocation creep		[189]
					948	75 – 125	1×10^{-8} to 2×10^{-7}	5.66			
					973	60 – 130	8×10^{-9} to 1×10^{-6}	6.03			
$Al_{0.3}CoCrFeNi$	T	VIM − HIP	FCC	303	973	65 – 110	1.8×10^{-9} to 9×10^{-9}	3	Dislocation glide slowed by $L1_2$ and B2 precipitates		[76]
					1003	50 – 110	1.5×10^{-9} to 4×10^{-8}	4.52			
					1033	40 – 110	2.2×10^{-9} to 9×10^{-7}	6.53			
$Al_{0.4}CoCrFeMnNi$	T	VIM − H − CR	FCC + BCC	30 – 85	873	120 – 300	2.5×10^{-9} to 1.5×10^{-7}	4.2	Dislocation climb		[82]
					923	130 – 240	7×10^{-8} to 3×10^{-7}	4.8			
					973	110 – 200	2×10^{-7} to 3×10^{-6}	4.9			
$Al_{0.5}CoCrFeMnNi$	T	VAM-A-HIP	FCC + Al,Ni-rich BCC precipitates	250	1,023	40 – 120	3×10^{-8} to 1.1×10^{-5}	4 – 6	dislocation climb		[31]
					1,098	25 – 100	5×10^{-8} to 6×10^{-5}	3	Solute drag creep		
					1,173	10 – 50	4×10^{-8} to 2×10^{-5}	3	Solute drag creep		
$Al_{0.6}CoCrFeMnNi$	T	VIM − H − CR	FCC + BCC	30 – 85	873	170 – 350	1×10^{-7} to 3.4×10^{-6}	5.8	Viscous glide (lower stress); dislocation-climb (high stress)		[82]
					923	80 – 230	1.7×10^{-7} to 1×10^{-5}	3.5			
$AlCoCrFeNi_{2.1}$	T	VAM	eutectic $L1_2$ + B2		973 – 1,073	50 – 240	6.67×10^{-8} to 4.96×10^{-6}	3.48	Dislocation gliding under moderate stress and temperature		[75]
					1,073 – 1,173	20 – 150	2.33×10^{-6} to 3.33×10^{-8}	4.1 – 4.4	Dislocation climbing for low stress and high temperature		
CoCrFeMnNi	T	VAM − H − CR − A	FCC	21.7	808	48 – 97	2×10^{-8} to 2×10^{-7}	2.6	Climb controlled		[73]
					873	25 – 97	1.6×10^{-8} to 2×10^{-6}	3.2, 5.9	Climb to glide controlled with increasing stress		
					923	22 – 97	7×10^{-8} to 7×10^{-5}	3.1, 5.8			
CoCrFeMnNi	T	VIM − HR − A	FCC	26.1	923	50 – 200	1.9×10^{-9} to 6.9×10^{-6}	5.94	dislocation creep, Sigma phase formation, worsen creep resistance		[97]
					948	50 – 150	1.2×10^{-8} to 2.8×10^{-6}	5.05			
					973	50 – 150	$5.6 \times 10.$ to 5.6×10^{-6}	4.13			

(*continued on next page*)

Table 4 (*continued*)

Composition	Testing Method	Fabrication method	Phase	Grain size [μm]	Temperature range [K]	Stress range [MPa]	Minimum Creep Rate [/s]	Stress exponent (n)	Creep mechanism	Load Rate [μN/s]	Ref
CoCrFeMnNi	T	VIM − H − CR − A	FCC	25	773	200 – 320	1.6×10^{-9} to 2×10^{-8}	5	Stress-assisted dislocation climbs controlled by lattice diffusion		[98]
					823	155 – 260	4×10^{-9} to 1×10^{-7}	6			
					873	130 – 200	2×10^{-8} to 3×10^{-7}	5.6			
CoCrFeMnNi	T	VIM − H − HF − A	FCC	18	848 – 923	103.4 – 206.8	10^{-1} to 10^{-3}	6.2	Transgranular with intergranular secondary cracking, vacancy diffusion-controlled dislocation climb		[99]
CoCrFeMnNi	T	VAM − DC − CR	FCC	140 – 150	973	50 – 110	6×10^{-9} to 7×10^{-7}	6	Dislocation climb		[78]
CoCrFeMnNi	T	VAM − DC − H − CR − A	FCC	24	1,023 – 1,173	40 – 130	10^{-4} to 7×10^{-8}	3.6 – 3.8	Controlled by dislocation lattice and dislocation–dislocation interactions		[100]
CoCrFeMnNi	T	VAM + DC + CR + A	FCC + Mn_3O_3 and MnO_2 (oxides in deformed only)	12 – 32	1,023	39 – 260	6.41×10^{-7} to 8.013×10^{-4}	3, 5	Dislocation climb at high strain rates (Ni diffusion rate-controlled process), solute drag at low strain rates characteristic of solid-solution alloys,		[101]
					1,048	23 – 223	6.41×10^{-7} to 8.013×10^{-4}	3, 5			
					1,073	16 – 189	6.41×10^{-7} to 8.013×10^{-4}	3, 5			
					1,123	31 – 140	7×10^{-6} to 8.013×10^{-4}	5			
CoCrFeMnNi	T	BM + SPC	FCC	0.8	1,073	10 – 30	10^{-6} to 4×10^{-9}	5.96			[69]
CoCrFeMnNi	SRC	VAM − DC − H − CR − A	FCC	21	1,073	60 – 160	2×10^{-4} to 10^{-6}	3.66	Forest dislocation interaction with solute		[105]
$(CoCrFeMnNi)_{98.5}C_{1.5}$	SRT	VAM − CR − HT	FCC	60	873	175 – 325	7×10^{-8} to 4×10^{-9}	3.03 – 6.99	Dislocation glide controlled, mediated with impurities (C and O), causing serrated flow		[107]
CoCrFeNi	T	VIM-PC-H	FCC + oxides	22.5	296 – 1,073	52 – 190	2.7×10^{-5} to 2.7×10^{-7}	6.31	Dislocation mediated creep with micro void initiation and coalescence		[109]
CoCrFeNi	T	VAM − DC − CR	FCC	140 – 150	973	50 – 140	3×10^{-6} to 10^{-8}	5.4	Dislocation climb		[78]
CoCrFeNi	T	VIM − HR − A	FCC	39.4	923	100 – 200	1.39×10^{-8} to 1.67×10^{-6}	6.75	Enhanced creep resistance compared to CoCrFeMnNi due to solid solution strengthening and suppressed second-phase formation		[97]
					948	50 – 150	5.56×10^{-9} to 3.06×10^{-6}	5.83			
					973	50 – 150	2.78×10^{-8} to 8.89×10^{-6}	5.36			
CoCrNi	T	VAM − DC − H − CR	FCC	149	973	50 – 130	2.6×10^{-9} to 7×10^{-7}	4.8	Dislocation climbs with low stacking fault energy and local chemical ordering may be		[77]
					1,023	40 – 110	1.3×10^{-8} to 2×10^{-6}	5.2			

(*continued on next page*)

Table 4 (*continued*)

Composition	Testing Method	Fabrication method	Phase	Grain size [μm]	Temperature range [K]	Stress range [MPa]	Minimum Creep Rate [/s]	Stress exponent (n)	Creep mechanism	Load Rate [μN/s]	Ref
					1,073	30 – 70	2×10^{-8} to 1.8×10^{-6}	5.5	possible reason for better creep resistance		
CoCrNi + ODS	T	LPBF	FCC + Y_2O_3	23.8	1,023	80 – 200	2×10^{-8} to 9×10^{-6}	6.7	Y_2O_3 suppresses GB creep void coalescence, as well as slow dislocation motion, failed from GB failure		[112]
					1,073	60 – 200	4×10^{-8} to 7×10^{-5}	6.5			
					1,123	60 – 200	2×10^{-7} to 5×10^{-4}	6.5			
					1,173	60 – 200	9×10^{-7} to 2×10^{-3}	6.4			
HfNbTaTiZr	T	VAM − DC − H − CR	BCC	98	1,253	60 – 110	7×10^{-6} to 2×10^{-4}	4.2	GB diffusion		[113]
$Ni_2Co_1Fe_1V_{0.5}Mo_{0.2}$	T	VIM − HF − A	FCC	>1000	973 – 1,073	150 – 200	1.9×10^{-8} to 3.88×10^{-6}	3.1	Dislocation climb		[116]
Multi-principal element superalloys (MPESAs)											
C-263: $Ni_{50.7}Cr_{22.42}Co_{19.5}Mo_{3.49}Ti_{2.48}Al_{0.9}Fe_{0.27}C_{0.24}$	T	VAM + HR + SA + PA	FCC + $L1_2$ + minor carbides $M_{23}C_6$ and MC at GBs	70	840 – 920	60 – 80	1.33×10^{-7} to 3.16×10^{-8}	4.9	Dislocation climb; cutting of γ′ at creep minimum; transition to climb-controlled creep in secondary stage.		[16]
C-264: $Ni_{45.31}Cr_{27.37}Co_{19.06}Mo_{3.33}W_{0.17}Ti_{2.02}Al_{2.21}Fe_{0.24}C_{0.29}$	T	VAM + HR + SA + PA	FCC + $L1_2$ + η + minor carbides	70	860 – 950	60 – 80	3.24×10^{-7} to 1×10^{-7}	4.4	Higher activation energy due to higher $L1_2$ volume fraction, inducing higher back stress. TiN formed during creep due to high solubility of N in Cr, detrimental to long term creep.		[16]
$Ni_{48}Co_{16.9}Cr_{7.5}Fe_{8.9}Mo_{0.9}W_{0.5}Ti_{5.8}Al_{10.3}Nb_{1.2}$	T	DS + ST + PA + SA	FCC (γ) + $L1_2$ (γ′)	Single crystal	1033	500 – 600	5.56×10^{-6} to 2.89×10^{-5}	9.6	Bypass and climb motion of dislocations in primary creep; paired dislocation shearing in secondary/rupture. The lattice rotates into ⟨100⟩, causing elongated γ′ precipitates via multi-slip. Secondary γ′ precipitates do not affect creep behavior due to bypassing mechanisms.		[19]
MatrixCMSX-3	T	DS + H	FCC	Single crystal	1253	15 – 75	2.02×10^{-5} to 9.85×10^{-4}	6.1	Solid solution strengthening		[141]
MatrixCMSX-4	T	DS + H	FCC	Single crystal	1253	15 – 75	7.01×10^{-7} to 2.30×10^{-5}	5.6	Increased Solid solution strengthening due to Re		[141]
CMSX-3	T	DS + ST + PA + SA	FCC + $L1_2$	Single crystal	1253	170 – 300	3.10×10^{-8} to 1.89×10^{-7}	6.6	Precipitate strengthening; γ′ shearing and dislocation bypass		[141]
Composition	**Testing Method**	**Fabrication method**	**Phase**	**Grain size [μm]**	**Temperature range [K]**	**Stress range [MPa]**	**Minimum Creep Rate [/s]**	**Stress exponent (n)**	**Creep mechanism**	**Load Rate [μN/s]**	**Ref**
Compression											
MPEA											
$Al_{0.5}CoCrFeMnNi$	Com	VAM-A	FCC + BCC	547.3	1,023	296 – 447	1×10^{-3} to 10	7	Solute drag at low strain rate and high temperature;		[10]

(*continued on next page*)

Table 4 (*continued*)

Composition	Testing Method	Fabrication method	Phase	Grain size [μm]	Temperature range [K]	Stress range [MPa]	Minimum Creep Rate [/s]	Stress exponent (n)	Creep mechanism	Load Rate [μN/s]	Ref
					1,098	188 – 447	1×10^{-3} to 10	7	dislocation creep and power law breakdown (PLB) at high strain rate		
					1,173	125 – 418	1×10^{-3} to 10	5, 7			
					1,248	95 – 302	1×10^{-3} to 10	5			
					1,323	45 – 288	1×10^{-3} to 10	3			
AlCoCrFeMnNi	Com	VAM	BCC + B2	118	1,173 – 1,373	68.9 – 386.2	10^{-3} to 10	7	From solute-drag creep to dislocation-climb creep and power law breakdown in similar temperature and strain rate range.		[93]
$AlNbTiVZr_{0.25}$	Com	VAM	B2 + Zr_5Al_3 precipitates	1.55	1,073	100 – 500	8×10^{-7} to 3×10^{-5}	3	Viscous glide; Nb_2Al −type sigma phase formation at Zr_5Al/B2 interface		[96]
CoCrFeMnNi	Com	BM-SPC	FCC	0.8	973 – 1,073	10 – 90	7×10^{-10} to 10^{-6}	6.3	Dislocation motion		[68]
CoCrFeMnNi	Com	SLM	Fcc + oxide (Mn-based)	12.93 – 15.66	873	150 – 325	8×10^{-9} to 3×10^{-7}	3.45, 6.45	Viscous glide (low stress); dislocation climb (high stress)		[102]
CoCrFeMnNi-BN	Com	SPS	FCC	1.53	973	30 – 150	1.1×10^{-8} to 1.7×10^{-5}	3.1, 7.3	Viscous motion of dislocation (solute drag) at high stress		[28]
					1,073	12 – 40	1×10^{-8} to 1×10^{-5}	4.0, 7.9			
MoNbTaVW	Com	VAM	BCC	138	1,123	400 – 520	4×10^{-7} to 1.1×10^{-6}	4.3	Dislocation pipe diffusion-controlled creep at lower temperatures and lattice diffusion controlled by Mo at higher temperatures.		[119]
					1,173	400 – 520	1.5×10^{-6} to 4×10^{-6}	3.6			
Multi-principal element superalloys (MPESAs)											
$Co_{29}Fe_{29}Ni_{29}Al_{4.3}Ti_{4.3}V_{4.3}$	Com	LPBF + H + AG	FCC + $L1_2$ (γ + γ′)	50 – 100	1123	45 – 120	7.8×10^{-8} to 2×10^{-5}	3.9	Dislocation creep, Limited creep resistance due to low γ′ fraction (~33%)		[140]
Composition	**Testing Method**	**Fabrication method**	**Phase**	**Grain size [μm]**	**Temperature range [K]**	**Maximum Load [mN]**	**Minimum Creep Rate [/s]**	**Stress exponent (n)**	**Creep mechanism**	**Load Rate [μN/s]**	**Ref**
Nanoindentation											
MPEA											
$Al_{0.3}CoCrFeNi$	Micro-indentation	VAM-A	FCC		RT	325	2.1×10^{-5}	5.6	Dislocation mechanisms that are sensitive to loading depth; pre compression promotes creep resistance		[91]
CoCrFeMnNi	N	VAM − CR-A	FCC	20 – 30	573	1000		8	Dislocation climb or glide	20,000	[32]
CoCrFeMnNi	N	VAM − HPT 5	FCC	0.018	RT	20	10^{-5} to 10^{-4}	steady state: 6.7	Collective effect of GB sliding and dislocation creep	7.5	[38]
CoCrFeMnNi (111)	N	DC	FCC	50	573	3	10^{-6} to 10^{-2}	3.8	Dislocation climb	0	[108]
					773	3	10^{-6} to 10^{-2}	4.3			
CoCrFeMnNi-Al (111)	N	DC	FCC + BCC	10	573	3	10^{-6} to 10^{-2}	5	Dislocation climb	0	[108]
					773	3	10^{-6} to 10^{-2}	4.3			
$Al_{33}Ti_{33}V_{34}$	N	VAM − DC	BCC + B2	80	300 – 873	3	10^{-4}	4.1	Dislocation glide and climb	300	[118]

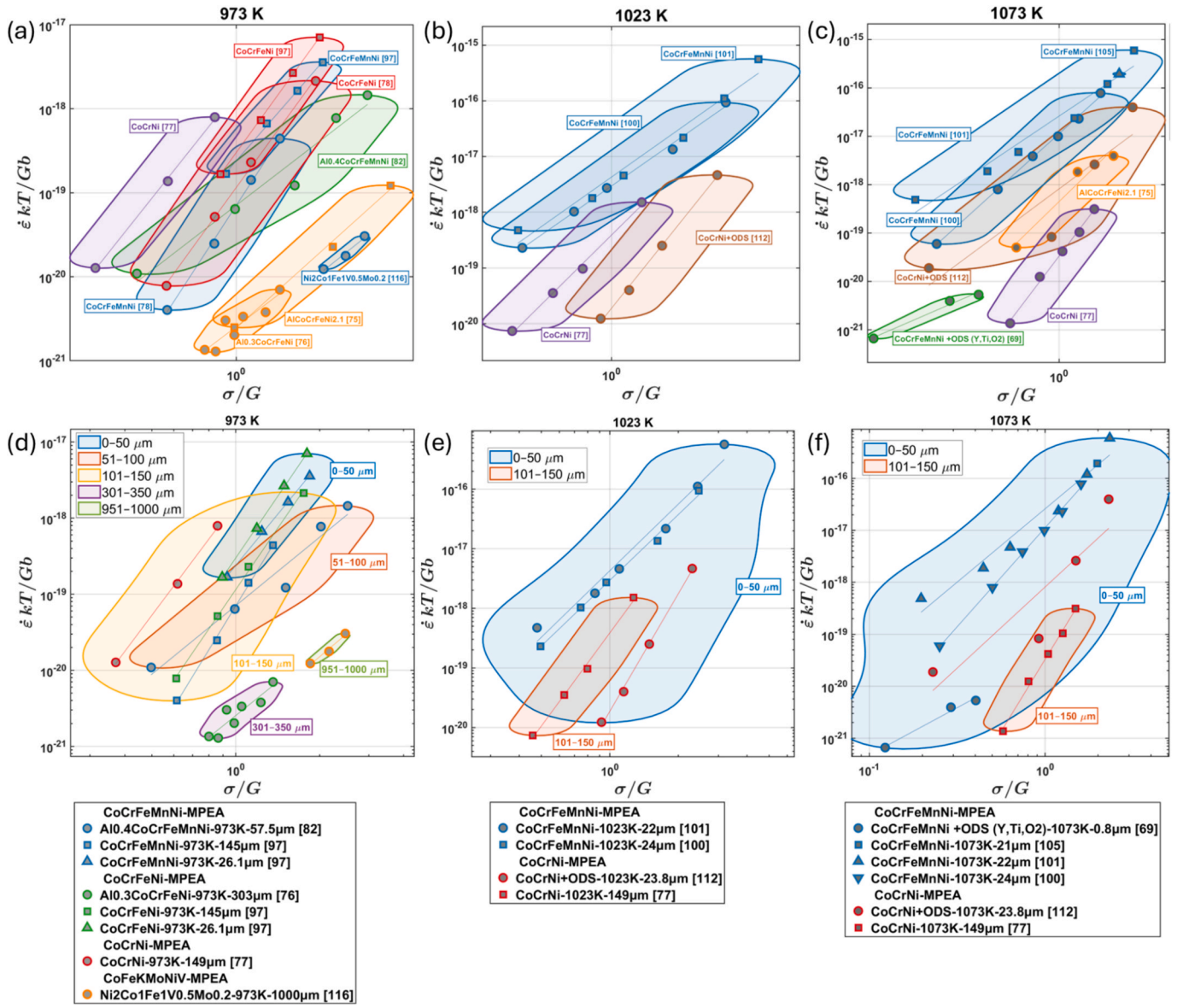

Fig. 4. The effect of composition (a, b, c) and grain size (d, e, f) within the MPEAs with creep exponent of n = 3 – 8, represented by the available creep data population at (a, d) 973 K, (b, e) 1023 K, and (c, f) 1073 K.

microstructure that results from GB sliding and dislocation glide [14]. Lastly, (Ti-Zr-Nb-Ta-Mo)C shows carbide precipitates forming at GB after creep in addition to a looped dislocation structure that originates at the GB [15]. All three MPECs show a combination of cracking at GBs with dislocation motion within the grains. Therefore, improvements to the creep properties of these ceramic systems would have to be towards slowing the dislocation motion as well as preventing crack nucleation at GBs. The cracks nucleating at GBs could be mitigated by increasing the grain size in the MPEC as all three reported systems have similar sizes between 3.66 and 25 μm.

Dislocation creep

Dislocation creep usually occurs at applied stresses of $\sigma/\mu > 10^{-4}$ and at moderate temperatures of $0.2 < T/T_m$, in which the dislocation-creep process is based on the hardening and recovery during creep [26,64]. There are several types of creep by dislocation interactions, such as dislocation–dislocation interaction, dislocation-particle interaction (solute-drag or viscous glide mechanism), dislocation climb, and dislocation glide [26,64]. Interactions between dislocations involve the formation of jogs or kinks, which require energy [26]. Jogs can be formed through thermal activation or due to dislocation intersections. Because there are more jog creations coming from dislocation intersections, the formation due to thermal energy of a jog is negligible. Dislocation climb is a process where an edge dislocation moves from one slip plane to another through vacancy movements while the dislocation glide is a process where dislocation moves within the same slip plane [26]. Vacancies are generally found on jogs and edge dislocations. Therefore, the vacancies participate in the dislocation-climb process [26].

The solute-drag or viscous glide mechanism is the competing mechanism against the dislocation climb [26,64]. Viscous glide depends on the solute atoms. Solute atoms function as obstacles to dislocation motion. Small atoms are attracted to compressive stress while larger atoms tend to move to tensile-stress regions, which are above and below the dislocation, respectively. The rate of dislocation movement is proportional to the diffusion rate of the solute atoms [26]. A recent study uncovered that while viscous glide may result from atom segregation at dislocations, it may also occur due to short-range ordering and chemical interactions between atoms and stacking faults [73,74]. Creep mediated

Table 5
Summary of results which show the power law breakdown and the expected creep mechanisms (n ≳ 8).

Composition	Testing Method	Fabrication method	Phase	Grain size [μm]	Temperature range [K]	Stress range [MPa]	Minimum Creep Rate [/s]	Stress exponent	Creep mechanism	Load Rate [μN/s]	Ref
Tension/Compression											
Multi-Principal Element Alloy (MPEA)											
$Al_{0.6}CoCrFeNi$	SRT	VIM	FCC + BCC		853	125 – 240	8×10^{-9} to 1×10^{-5}	10.63	Higher Al content and BCC phase increase SFE allowing for easier dislocation creep via cross-slip.		[89]
					898	85 – 185	1.6×10^{-8} to 8×10^{-6}	8.76			
					923	75 – 170	1.1×10^{-8} to 7×10^{-6}	8.46			
					948	70 – 155	8×10^{-9} to 8×10^{-6}	8.28			
					973	60 – 140	1.3×10^{-8} to 1.1×10^{-5}	7.98			
CoCrFeMnNi	T	VIM − H − CR − A	FCC	25	773	320 – 400	2×10^{-8} to 1.4×10^{-7}	14	Stress-assisted dislocation climbs controlled by lattice diffusion		[98]
					823	260 – 350	2×10^{-8} to 3×10^{-6}	10			
					873	200 – 320	3×10^{-7} to 1×10^{-5}	8.9			
CoCrFeMnNi + ODS (Y_2O_3 + Ti)	Com	BM-SPC	FCC + oxides	0.4	973	48 – 100	2×10^{-9} to 1×10^{-5}	13.2	Lattice diffusion at low stresses and dislocation controlled by oxide interaction at high stresses after subtracting with threshold stress		[68]
					1,023	35 – 82	2.5×10^{-9} to 3×10^{-5}	13.2			
					1,073	32 – 65	7.5×10^{-9} to 4.5×10^{-5}	13.2			
CoCrFeMnNi-AlN	Com	SPS	FCC	0.43	973	35 – 90	1×10^{-8} to 7×10^{-5}	9.53	Climb-controlled dislocation motion		[28]
					1,073	18 – 41	1.7×10^{-8} to 3×10^{-5}	9.36			
Multi-principal element superalloys (MPESAs)											
$Ni_{48}Co_{16.9}Cr_{7.5}Fe_{8.9}Mo_{0.9}W_{0.5}Ti_{5.8}Al_{10.3}Nb_{1.2}$	T	DS + ST + PA + SA	FCC (γ) + $L1_2$ (γ′)	Single crystal	1033	500 – 600	5.56×10^{-6} to 2.89×10^{-5}	9.6	Bypass and climb motion of dislocations in primary creep; paired dislocation shearing in secondary/rupture. The lattice rotates into ⟨1 0 0⟩, causing elongated γ′ precipitates via multi-slip. Secondary γ′ precipitates do not affect creep behavior due to bypassing mechanisms.		[19]
CMSX-4	T	DS + ST + PA + SA	FCC + $L1_2$	Single crystal	1253	170 – 300	3.20×10^{-9} to 6.64×10^{-7}	12.5	Precipitate + Re solid solution strengthening; very high internal back stress		[141]
Nanoindentation											
Multi Principal Element Alloy (MPEA)											
Composition	**Testing Method**	**Fabrication method**	**Phase**	**Grain size [μm]**	**Temperature range [K]**	**Maximum Load [mN]**	**Minimum Creep Rate [/s]**	**Stress exponent**	**Creep mechanism**	**Load Rate [μN/s]**	**Ref**
$Al_{0.3}CoCrFeNi$	N	VAM − H	FCC	400 – 1000	RT	3		48	Dislocation climb and slip	1,000	[37]
						9	1.31×10^{-4}	90		1,000	
$Al_{0.3}CoCrFeNi$	Micro-indentation	VAM − A	FCC		RT	75	1.4×10^{-5}	13.1	Creep behavior is dislocation mechanisms and are sensitive to loading depth; pre compression promotes creep resistance.		[91]
						150	1.3×10^{-5}	13.7			
						225	1.8×10^{-5}	10.7			

(*continued on next page*)

Table 5 (*continued*)

Composition	Testing Method	Fabrication method	Phase	Grain size [μm]	Temperature range [K]	Stress range [MPa]	Minimum Creep Rate [/s]	Stress exponent	Creep mechanism	Load Rate [μN/s]	Ref
$Al_{0.5}CoCrCuFeNi$	N	VAM + DC			RT 473	100 100	3.3×10^{-3} 5.2×10^{-3}	121 96.6	Serrated flow due to interactions between moving dislocations and obstacles	10^4 10^4	[92]
CoCrFeMnNi	N	VAM − CR − A	FCC	20 – 30	298	500 – 1000		32, 15	Dislocation climb or glide	2×10^4	[32]
					423	500 – 1000		36, 10		2×10^4	
					573	500		30		2×10^4	
CoCrFeMnNi	N	SLM	FCC	46	RT	5–50	10^{-5}	16.67 – 27.03	Dislocation motion dominated	500	[36]
CoCrFeMnNi	N	VAM	FCC	50	RT	20	10^{-4} to 10^{-5}	transient state: 109 – 136; steady state: 29.8 – 32	Dislocation controlled	75 – 5,000	[38]
		VAM − HPT 3	FCC	0.025	RT	20	10^{-4} to 10^{-5}	transient state: 76.6 – 103.8	Collective effect of GB sliding and dislocation creep	75 – 5,000	
		VAM − HPT 5	FCC	0.018	RT	20	10^{-4} to 10^{-5}	transient state: 58.3 – 61; steady state: 10.3	Collective effect of GB sliding and dislocation creep	75 – 5,000	
$(CoCrFeMnNi)_{98.6}C_{0.6}N_{0.8}$	N	VIM + HR + H	FCC		RT	5	9.5×10^{-4} to 6×10^{-4}	2 – 180	From diffusion mediated to dislocation controlled with increasing stress exponent	200	[9]
CoCrNi	N	VAM − CR − A	FCC	20 – 30	298	500 – 1000		90, 85	Dislocation climb or glide	2×10^4	[32]
					423	500 – 1000		25, 40		2×10^4	
					573	500 – 1000		38, 35		2×10^4	
HfTaTiVZr	N	VAM	BCC	250	298	1 – 5		122, 56	Dislocation dominated deformation, sluggish diffusion, and severe lattice strain	2×10^4	[33]
					423	1 – 5		70, 60		2×10^4	
					573	1 – 5		20, 45		2×10^4	
$MoTaNbV_{0.25}Ti$	Dynamic indentation test	VAM	BCC + HCP laves		RT	45 – 550	10^{-4} to 10^{-3}	38 – 44.57	Lattice distortion increased with increasing V, reducing n		[115]
$MoTaNbV_{0.5}Ti$	Dynamic indentation test	VAM	BCC + HCP laves		RT	47 – 550	10^{-4} to 10^{-3}	27.8 – 44	Lattice distortion increased with increasing V, reducing n		[115]
$MoTaNbV_{0.75}Ti$	Dynamic indentation test	VAM	BCC + HCP laves		RT	37 – 550	10^{-4} to 10^{-3}	30.7 – 38	Lattice distortion increased with increasing V, reducing n		[115]
$Ni_{34.1}Co_{33.9}Cr_{20.9}Mo_{10.2}Ti_{0.9}$ (SNG-9)	N	mechanical grinding treatment	FCC	0.009 – 0.03	973	900 – 1000	10^{-7}	>100	Lack of dislocation in extreme fine grain suppressed GB migration and sliding. Stable GB networks		[72]
TaTiVWZr	N	VAM	BCC1 + BCC2		298	$1 \times 10^{-3} - 5 \times 10^{-3}$		145, 65	Dislocation dominated deformation, sluggish diffusion, and severe lattice strain	2×10^4	[33]
					423			70, 60		2×10^4	
					573			50, 55		2×10^4	

by dislocations typically have a stress exponent value of $n = 3$ to 8. From the collected literature used in this review, the creep behavior of the most studied alloy systems has base compositions of CoCrNi, CoCrFeNi, and CoCrFeMnNi, which are controlled by dislocation interactions. All of the reviewed literature that reported $3 < n < 8$ are summarized in Table 4. This includes just MPEA and MPESA and are sorted by the testing method and material type. The MPECs reviewed showed a combination of GB sliding and dislocation creep and were discussed in the previous section.

Dobes et al. [68] reported that at stress levels of 40 to 100 MPa, CoCrFeMnNi-ODS has $n = 13.2$ and a creep mechanism by dislocations controlled by oxide interactions. Typically, $n > 10$ deviates from classical creep mechanisms. However, microstructural investigations indicate that a creep mechanism is indeed affected by oxide interactions with dislocations. By incorporating a threshold stress, the reported creep mechanism can be rationalized [68]. Particles in secondary-phase-strengthened materials obstruct dislocation glide [75]. Therefore, the stress that controls the velocity of a dislocation is reduced by subtracting the applied stress with the necessary stress (referred to as a threshold stress) to move past the particles. Then, the steady-state creep-rate dependence on the applied stress changes from a general term (Eq. (6) [75]) to a more specific term (Eq. (7) [75]), where D is the diffusion coefficient, G is the shear modulus, E is the elastic modulus, d is the grain size, p is the inverse grain size, A is a dimensionless constant, and σ_0 is the threshold stress produced by the second-phase particles.

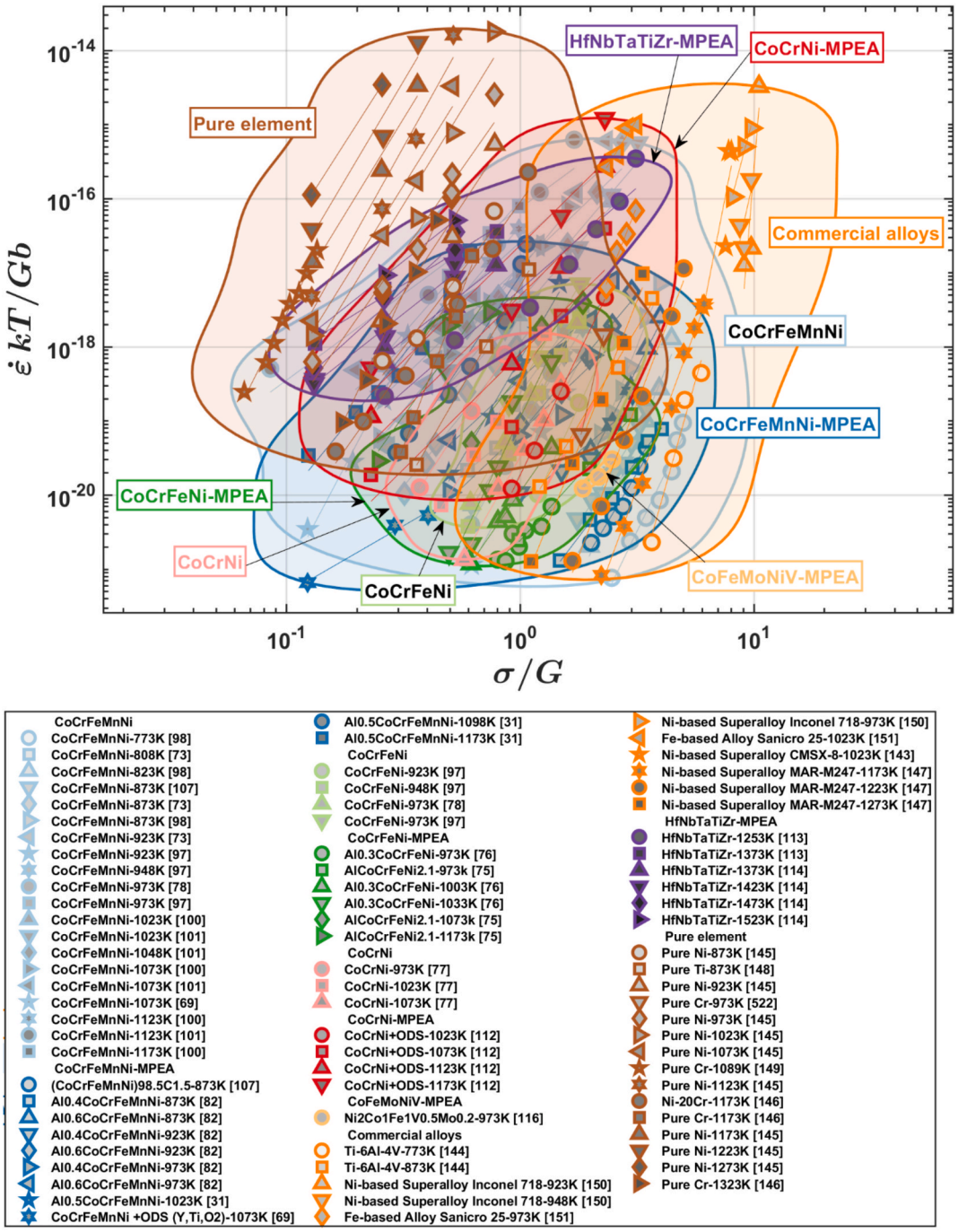

Fig. 5. Creep strain rate normalized to shear modulus (G) and Burgers vector, taking into account the temperature versus applied stress normalized to G, obtained by the tension-creep tests of MPEAs and RMPEAs compared with pure elements and commercial alloys [143–151].

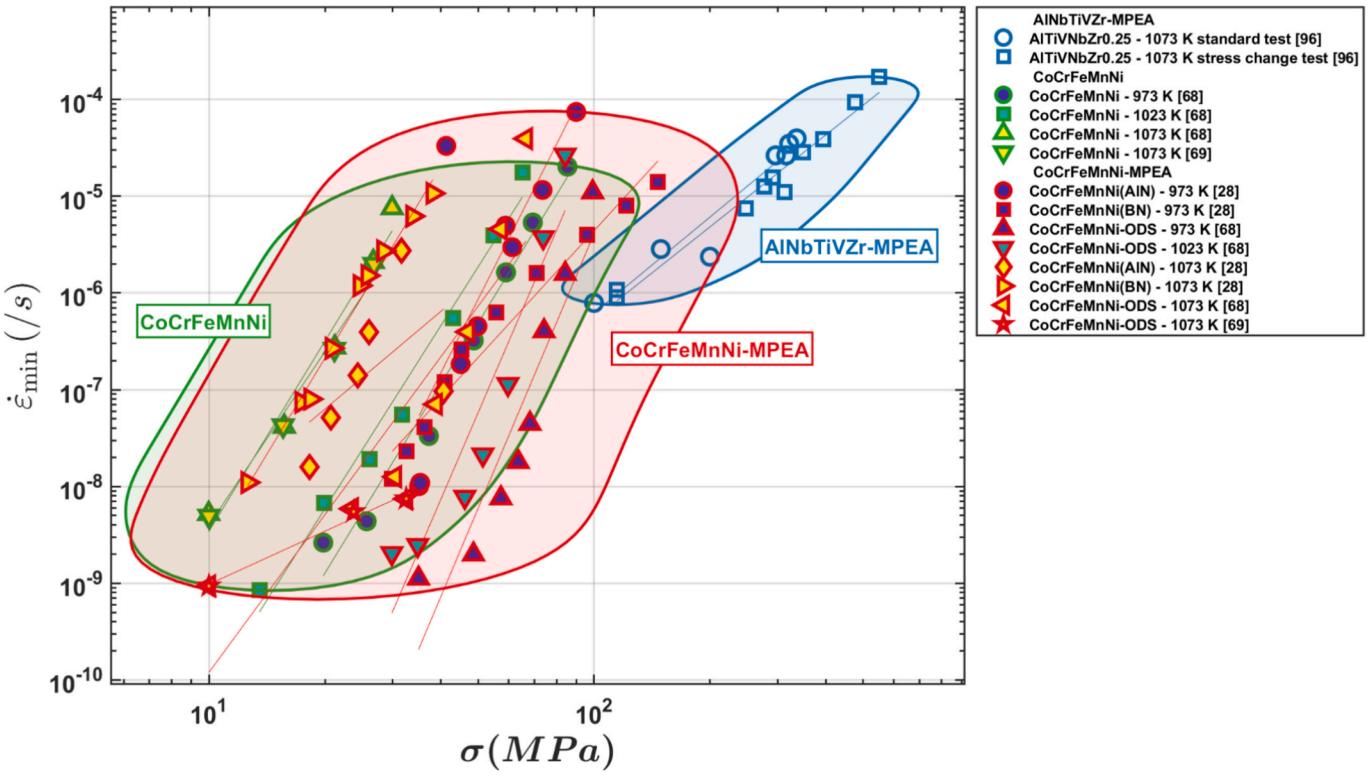

Fig. 6. Creep strain rate versus stress of MPEAs under compressive loads.

$$\dot{\varepsilon} = (ADGb/kT)(b/d)^p(\sigma/G)^n = (ADEb/kT)(b/d)^p(\sigma/E)^n \quad (6)$$

$$\dot{\varepsilon} = (ADGb/kT)(b/d)^p((\sigma - \sigma_0)/G)^n \quad (7)$$

Chen et al. [76] reported the creep behavior of $Al_{0.3}$CoCrFeNi (n = 3 to 6.53) where the face-centered cubic (FCC) phase decomposes into $L1_2$ and B2 phases at earlier (creep time of 50 h) and later (creep time of 250 h) parts of stage II creep, respectively. The $L1_2$ phase functioned as obstacles towards dislocations along with dislocation glide at 973 K, while at a later stage of creep, the B2 phase served as obstacles toward the dislocation motion, significantly enhancing creep resistance.

Chu et al. [27] reported the creep behavior of CoCrFeMnNi through stress-relaxation tests (SRT). The primary finding based on the calculated activation volume ($12-62b^3$) was that a dislocation glide mediated by impurities is the governing creep mechanism. However, microstructural evidence was not presented.

Xie et al. [77] studied the creep behavior of the medium-entropy CoCrNi (n = 5.3) tested at temperatures of 973 to 1,073 K. In their work, the dislocation-climb mechanism is proposed to be dominant, while a low stacking fault energy (SFE) is the possible reason for the increased creep resistance, compared to CoCrFeMnNi. The climb-dislocation mechanism is also reported for CoCrFeNi (n = 5.4) and CoCrFeMnNi (n = 6), tested at 973 K [78], although the creep behavior of these compositions is not enhanced by the low SFE as it is in CoCrNi.

The climb to glide creep mechanism of CoCrFeMnNi (n = 2.6 to 5.9) tested from 808 K to 923 K was reported by Kang et al. [73], where the viscous glide is more favorable at applied stress values > 40 MPa in this system [37,73,74,79,80]. It is suggested that the transition from the climb to glide mechanism is due to the influence of the configurational entropy and the strain-energy tradeoff [37,73,81]. If the reduction of strain energy is more than the reduction of the configurational entropy, then the segregation of atoms at a dislocation is favored, and dislocation climb is preferred [73]. On the other hand, if the increase of the strain energy is more than the increase of the configurational entropy, then the dislocation will glide due to a dragging stress [73]. An atomic-size misfit is also suggested to play an important role on the climb to glide transition where it was found that Cr is the most influential element of the viscous glide in the CoCrFeMnNi system [74]. A dislocation climb to glide transition is also reported on $Al_{0.6}$CoCrFeNi (n = 2.8 to 5.8) by Cao et al. [82]. A dislocation-climb mechanism occurred at 873 K, which was then transitioned to a viscous glide mechanism at higher temperatures of 923 to 973 K [82].

The transition from a dislocation glide to dislocation climb at different temperatures was reported in $AlCoCrFeNi_{2.1}$ by Li et al. [75], where from 973 to 1,073 K (n = 3.48), the creep deformation is by dislocation glide. At higher temperatures from 1,073 to 1,173 K (n = 4.10 to 4.40), the creep deformation is governed by dislocation climb. In this system, precipitation strengthening enhanced creep resistance where the precipitate size increased with increasing temperature, increasing precipitation strengthening at 1,173 K compared to the one tested at 1,073 K. The transition from a glide to climb mechanism is hypothesized to be caused by the generation of precipitates at higher temperatures. Jeong et al. [31] reported the transition of the creep mechanism of $Al_{0.5}$CoCrFeNi from a solute drag (n = 3) to dislocation climb (n = 5) to power-law breakdown (n = 7) by increasing the applied stress and test temperature. This system has body-centered cubic (BCC) particles due to the addition of Al in the CoCrFeNi system. However, it is not as effective as the alloy system that was strengthened by ODS [69].

Fig. 4 highlights the effect of composition and grain size at 973 K, 1023 K, and 1073 K with reported creep exponent, n = 3 to 8, across different MPEA compositions. Within the same stress range, the lower creep rate was achieved by altering the composition with addition of alloying elements such as Al, Mo, and V, addition of particles such as ODS, or lowering the SFE of the alloy system [77] as discussed above. Within the creep temperature shown in Fig. 4 (d) to (f), within the similar stress range, the lower creep rate was achieved by the materials with larger grain size, which is within the expectation due to the reduction of the fast diffusion path via grain boundary.

Power-law breakdown

The power-law breakdown is the mechanism where the creep behavior deviates from the classical power-law creep characteristics, which has been discussed in the previous section [83]. At temperatures below about $0.6T_m$, an accelerated creep rate is observed, leading to a higher creep exponent ($n \geq 8$). The power-law breakdown is expressed phenomenologically as Eq. (8) [84,85], where A_1 is a constant,α_1 is an empirical fitting parameter, and n equals 5.

$$\dot{\varepsilon} = A_1 exp[-Q_C/kT][sinh\alpha_1(\sigma/E)]^n \quad (8)$$

There are several theories about the power-law breakdown. First, it was theorized that in the power-law breakdown, there is a change in the mechanism controlling the rate of a steady-state flow from the dislocation climb to dislocation glide. However, this theory is sometimes based on the presence of an internal stress, which might not be reasonable because the long-range internal stresses seem to be low in both the power-law and power-law breakdown regimes [86]. Second, it was recently discovered that the level of vacancy oversaturation from plasticity is sufficient to create higher creep rates in the power-law breakdown regime [87,88]. Third, it was observed that the changes in the diffusion coefficient to dislocation-pipe diffusion coefficient with large strain plasticity in the testing condition within the power-law breakdown regime might contribute independently to the power-law breakdown [88]. The reported MPEAs and MPESAs with $n \geq 8$ are summarized in Table 5.

Power-law breakdown was observed in an $Al_{0.5}CoCrFeMnNi$ [10]. However, the reported experiment was conducted with high-temperature compression tests instead of compression-creep tests. At lower strain rates (10^{-3} to 10^{-2} /s), the reported deformation mechanism is a dislocation glide with solute drag with a stress exponent ($n = 3$) and activation energy of 251.9 kJ/mol. A power-law breakdown was found at higher strain rates ($\dot{\varepsilon} > 10^{-2}$ /s) where the n and Q increase to $n > 5$ and 306.6 kJ/mol, respectively. It was suggested that the dislocation climb mechanism was activated at higher strain rates in this system, which enables stress relaxation and leads to power-law breakdown.

Lastly, many indentation tests report $n \geq 8$. Although this feature falls in the power-law breakdown regime, this may be due to the often low testing temperatures and very high localized stresses for short time frames. Additionally, many reported creep mechanisms conflict with creep mechanisms expected from the reported stress exponent. These reported experiments are also included in Table 5 below.

Creep behavior of MPEMs

Multi-pincipal element alloys

Comparison of tension-creep behavior of MPEAs at several temperatures

Fig. 5 presents the collected tensile creep strain from the scientific literature, taking into account the temperature normalized to the shear modulus and the Burgers vector versus the applied stress normalized to shear modulus. The temperature range of the tensile creep tests performed is from 773 to 1,523 K, while the applied stress ranges from 5 to 400 MPa. Generally, the creep behavior of CoCrFeMnNi and some variations of CoCrFeMnNi, such as $(CoCrFeMnNi)_{98}C_{1.5}$ and $Al_xCoCrFeMnNi$, are comparable to commercial alloys, notably Ti-6Al-4 V at lower temperatures. Although HfNbTaTiZr was tested at higher temperatures (1,253 – 1,523 K), the creep rate is more comparable to pure elements.

One of the lowest creep rates in MPEAs at 873 K occurs in $(CoCrFeMnNi)_{98.5}C_{1.5}$ (6×10^{-8} to 4×10^{-9} /s at 175 – 325 MPa) [107] and is comparable to Ti-6Al-4 V [144]. This creep behavior was found to be attributed to the stable subgrains due to heterogeneously structured grains, dislocation network, and uniform carbide formation at GBs and sub-GBs. The stable subgrains caused the formation of serrated GBs, strengthening the subgrains, and suppressing recrystallization during creep. $Al_{0.4}CoCrFeMnNi$ (0.5×10^{-7} to 2×10^{-9} /s from 120 to 320 MPa) showed comparable creep behavior to $(CoCrFeMnNi)_{98.5}C_{1.5}$ at similar applied stresses due to solution strengthening and strengthening from the formation of a secondary phase. However, adding more Al was found to be detrimental due to higher SFE, allowing easier cross-slips in $Al_{0.6}CoCrFeMnNi$ and increasing creep rates (4×10^{-6} to 7×10^{-8} /s at 120 to 320 MPa).

ODS CoCrNi (2×10^{-3} to 2×10^{-8} /s from 80 to 200 MPa) [112] has the lowest minimum creep rate at the temperature of 1,023 K compared to other MPEAs reviewed in this study. ODS CoCrNi creep behavior is attributed to the dislocation and oxide interactions. At 1,073 K, CoCrFeMnNi + ODS [69] demonstrated the lowest minimum creep rate at a lower applied stress while CoCrNi (10^{-6} to 2×10^{-8} /s from 30 to 60 MPa) [77] exhibited the lowest minimum creep rate at a higher applied stress. This is reportedly due to oxides acting as obstacles for CoCrFeMnNi + ODS and a lower SFE for CoCrNi.

HfNbTaTiZr [113] decomposes into Zr- and Hf-rich precipitates during creep at 1,253 K [113 10] meanwhile, HfNbTaTiZr's [114] creep behavior is inferred to likely have been controlled by a solute-drag mechanism where the creep rates were controlled by diffusivity of Ta.

Table 6
Summary of Activation Energy of some MPEAs. The creep-activation energy and stress exponent are listed for each composition and test method. For Q's and n's listed as a range, the reference used many stresses and temperatures, resulting in many calculated values. Specific single values listed refer to one temperature or stress for the stress exponent and creep-activation energy, respectively. Q and n listed with a family of planes {*hkl*} means that the orientation of the grain was checked before the experiment. Otherwise, the Q and n refer to an average across many orientations.

Composition	Test Method	Creep Activation Energy (Q) [kJ/mol]	Stress Exponent (n)	Ref
Multi-Principal Element Alloy (MPEA)				
$Al_{0.3}CoCrFeNi$	T	390.5 – 548.2	3 – 6.53	[76]
$Al_{0.4}CoCrFeMnNi$	T	258, 348	1.6 – 4.9	[82]
$Al_{0.6}CoCrFeMnNi$	T	188	3.2	[82]
$AlCoCrFeNi_{2.1}$	T	54.26 – 431.96	3.48 – 4.40	[75]
CoCrFeMnNi	T	9.45 – 66.136	N/A	[27]
CoCrFeMnNi	T	249 – 319	2.6 – 5.9	[73]
CoCrFeMnNi	T	210 – 508	4.13 – 5.94	[97]
CoCrFeMnNi	T	260 – 275, 372 – 410	5.5, 10.6	[98]
CoCrFeMnNi	T	394	6.2	[99]
CoCrFeMnNi	T	284, 333	2 – 3, 4 – 5	[101]
CoCrFeMnNi	T	218.7 – 235.9	3.6 – 3.8	[100]
CoCrFeNi	T	375 – 430	5.36 – 6.75	[97]
CoCrFeNi	T	363	6.31	[109]
CoCrNi	T	335 – 367	6.5	[112]
CoCrNi	T	370	5.5	[77]
HfNbTaTiZr	T	273 ± 15	2.5 – 2.8	[114]
$Al_{0.5}CoCrFeMnNi$	Com	251 – 306.6	3.9 – 5.3	[10]
CoCrFeMnNi	Com	246 – 704	6.3	[68]
CoCrFeMnNi	Com	335	3.45	[102]
CoCrFeMnNi + ODS (Y_2O_3 + Ti)	Com	210 – 580	1.75	[68]
CoCrFeMnNi-AlN	Com	530	9.5	[28]
CoCrFeMnNi-BN	Com	524, 350	7.8, 3.1	[28]
MoNbTaVW	Com	150 – 335	1.2 – 3.6	[119]
CoCrFeMnNi	N, B-d	259 {111}, 239 {100}	3.8 – 4.3	[108]
CoCrFeMnNi-Al	N, B-d	260	4.3 – 5	[108]
AlTiV	N, B-s	250	4.1	[118]
CoCrFeMnNi	N, B-s	400	15 – 90	[32]
CoCrNi	N, B-s	25	15 – 30	[32]
HfTaTiVZr	N, B-s	925	20 – 120	[33]
TaTiVWZr	N, B-s	1000	20 – 140	[33]
$Al_{0.15}CoCrFeNi$	SRT	387.1 – 418.3	4.98 – 6.03	[89]
$Al_{0.6}CoCrFeNi$	SRT	293.1 – 338.2	7.46 – 10.63	[89]

T = tension; Com = compression; N = nanoindentation; B = Berkovich (d = diamond, s = sapphire); SRT = stress relaxation test.

At 1,373 K for HfNbTaTiZr, Liu et al. [114] reported a slightly lower minimum creep rate of 7×10^{-6} to 3×10^{-7} /s compared to Gadelmeier et al. [113] with creep rates of 8×10^{-4} to 3×10^{-6} /s. The slightly lower minimum creep rate reported by Liu et al., even at higher temperature could be attributed to a larger grain size of 1 mm versus the smaller grain size of 100 μm reported by Gadelmeier et al.

Looking at the big picture, the lowest reported creep rates are not solely governed by the composition alone but are often influenced by microstructures and specific stress–temperature windows, which makes direct ranking across systems difficult. Overall, the apparent conflicts in reported creep rate and inferred mechanisms across similar compositions can often be rationalized by the differences in the microstructural stability during test and the initial microstructures, such as different grain sizes, precipitation existence, and phase fractions.

Comparison of compression-creep behavior of MPEAs at several temperatures

Fig. 6 presents the compression-creep strain rate from the collected scientific literature versus the applied stress for a variety of MPEAs. At temperatures of 973 and 1,023 K, CoCrFeMnNi-ODS (2.04×10^{-9} /s at 30 MPa and 1,023 K) [68] has lower minimum creep rates at similar applied stresses, compared with CoCrFeMnNi (4.54×10^{-9} /s at 30 MPa and 1,023 K) [68], CoCrFeMnNi-AlN (1.01×10^{-8} /s at 33 MPa and 973 K) [28], and CoCrFeMnNi-BN (2.3×10^{-8} /s at 33 MPa and 973 K) [28]. CoCrFeMnNi-ODS (0.4 μm) [68] was reportedly deformed by lattice diffusion creep at 10 to 50 MPa. At higher applied stresses (50 to 100 MPa), the creep rate of CoCrFeMnNi-ODS [68] has to be adjusted to take into account the threshold stress. The creep behavior at a higher applied stress in this system is dislocation controlled by oxide interactions. The addition of AlN to CoCrFeMnNi did not change the minimum creep rate at the applied stress from 10 to 50 MPa, while the addition of BN lowered the minimum creep rates from 50 to 150 MPa to 0.5×10^{-5} /s from 7×10^{-5} /s at 100 Ma [28]. The creep behavior of CoCrFeMnNi-AlN and −BN is argued to be controlled by viscous motion of dislocations. One of the reasons for the difference in behavior could be because of the different grain sizes, where CoCrFeMnNi-AlN (0.43 μm) has a smaller grain size than CoCrFeMnNi-BN (1.53 μm). The difference in creep behavior was reported to have been caused by phenomena affecting the dislocation climb to glide transition, such as an atomic size misfit, SFE, and sub-grain size stability.

At a temperature of 1,073 K, CoCrFeMnNi-ODS (3×10^{-5} to 10^{-9} /s) [68,69] also had significantly lower minimum creep rates compared to CoCrFeMnNi (10^{-5} to 4×10^{-9} /s) [68,69], CoCrFeMnNi-AlN (3×10^{-5} to 0.5×10^{-8} /s), and −BN (10^{-5} to 9.5×10^{-8} /s) [28] at similar applied stresses (10 – 100 MPa). $AlTiVNbZr_{0.25}$ [96] was tested at higher applied stresses (100 – 500 MPa). However, it could potentially have a similar

Table 7
Summary of Activation Volume (V^*) of some MPEAs. Most reported V^* values are given in terms of the Burgers vector cubed (b^3) although some are listed as volumes. These values can be converted by knowing the Burgers vector for the material. V^* listed with a family of planes {*hkl*} means that the orientation of the grain was checked before the experiment, otherwise the V^* refers to an average across many orientations. Two V^* values were reported in terms of m^3/mol without a mass or mole listed in the reference to converting the units to m^3.

Composition	Test Method	Activation Volume (V*)	Burgers Vector [nm]	Stress Exponent (n)	Ref
Multi Principal Element Alloy (MPEA)					
CoCrFeMnNi	Com	300 – 800 b^3	0.255	6.3	[68]
CoCrFeMnNi(high stress region)	Com	52.9 b^3	0.255	6.45	[102]
CoCrFeMnNi(low stress region)	Com	41.2 b^3	0.255	3.45	[102]
$Al_{2.5}$CoCrCuFeNi	N, B	0.51 nm^3	–	–	[11]
CoCrCuFeNi	N, B	0.08 nm^3	–	–	[11]
CrFeNi	N, B	31.8 b^3	0.254	–	[30]
CrFeNi(aged 1 hr)	N, B	29.5 b^3	0.254	–	[30]
CrFeNi(aged 10 hr)	N, B	16.6 b^3	0.254	–	[30]
CrFeNi(aged 100 hr)	N, B	12.3 b^3	0.254	–	[30]
CrFeNi(aged 1,800 hr)	N, B	28.6 b^3	0.254	–	[30]
CrFeNi(aged 485 hr)	N, B	32.8 b^3	0.254	–	[30]
$Ti_{30}Al_{25}Zr_{25}Nb_{20}$	N, B	0.004 – 0.048 nm^3	–	9.89	[117]
CoCrFeMnNi	N, B-d	10 – 18 b^3	0.252	–	[103]
CoCrNi	N, B-d	11 b^3	0.225	–	[111]
CoCrNi	N, B-d	9 – 17 b^3	0.225	–	[103]
CoCrNi (600 °C anneal)	N, B-d	15 b^3	0.225	–	[111]
CoCrNi (700 °C anneal)	N, B-d	20 b^3	0.225	–	[111]
CoCrNi (800 °C anneal)	N, B-d	29 b^3	0.225	–	[111]
CoCrFeMnNi	N, B-d	56 – 180 b^3 {111}, 56 – 241 b^3 {100}	–	3.8 – 4.3	[108]
CoCrFeMnNi-Al	N, B-d	50 – 198 b^3	–	4.3 – 5	[108]
CoCrFeMnNi	N, Sph	~4.6 b^3	0.225	1.03 – 2.91	[104]
HfTaTiVZr	N, B-s	0.5 ± 0.11 nm3 (~20 b^3)	1/2 a [111] (~0.34 nm)	30 – 125	[33]
TaTiVWZr	N, B-s	0.4 ± 0.09 nm^3 (~16 b^3)	1/2 a [111] (~0.34 nm)	40 – 140	[33]
Pure W	N, B-s	0.25 ± 0.1 nm^3 (~13 b^3)	1/2 a [111] (~0.31 nm)	30 – 50	[33]
CoCrFeMnNi	SRC	114 – 153 b^2	N/A	3.66	[105]
$Al_{0.4}$CoCrFeMnNi	T	1.4 – 2.03 × 10^{-4} [m^3/mol]	–	1.6 – 2.2, 4.2 – 4.9	[82]
$Al_{0.6}$CoCrFeMnNi	T	1.8 – 2.41 × 10^{-4} [m^3/mol]	–	5.8, 2.8 – 3.5	[82]
CoCrFeMnNi	T	12 – 62 b^3	0.255	N/A	[27]
CoCrFeMnNi	T	112 b^3	a/2 < 110> (a = 3.5991Å)	6	[78]
CoCrFeMnNi	T	38.3 – 123.6 b^3	0.255	2 – 3, 4 – 5	[101]
CoCrFeNi	T	123 b^3	a/2 < 110> (a = 3.5715Å)	5.4	[78]
CoCrNi	T	100 – 200 b^3	0.225	5.5	[77]
CoCrNi	T	88 b^3	a/2 < 110> (a = 3.5590Å)	5.5	[78]

T = tension; Com = compression; N = nanoindentation; B = Berkovich (d = diamond, s = sapphire); Sph = spherical.

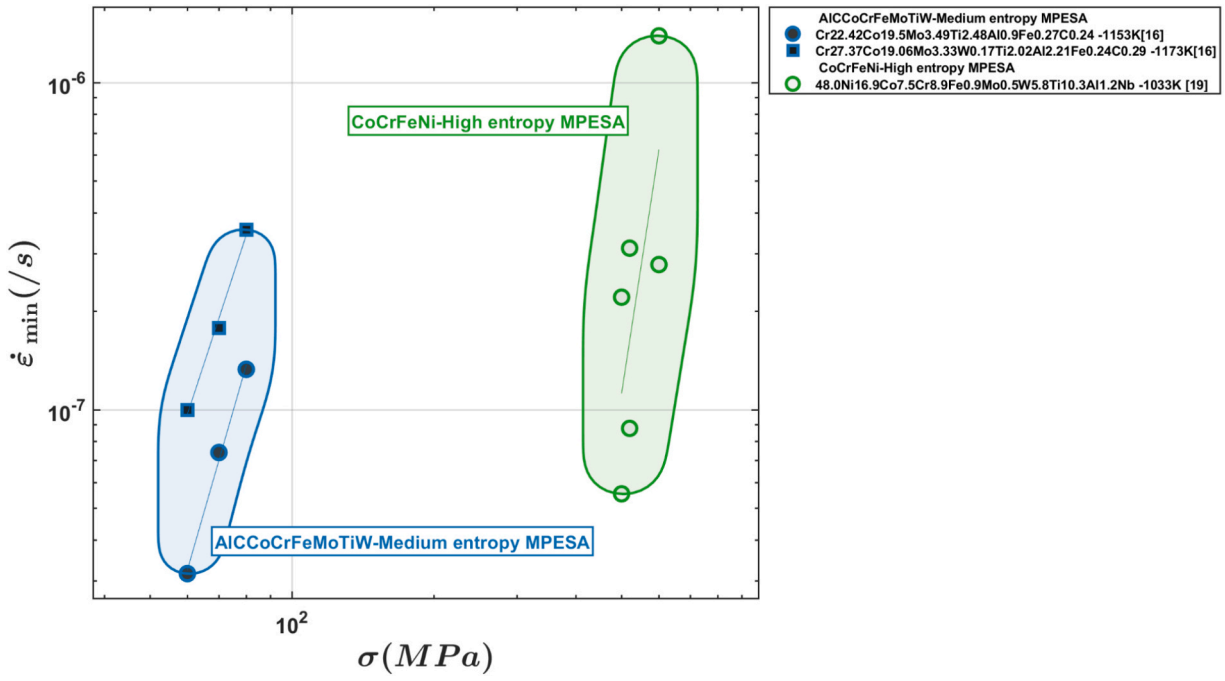

Fig. 7. Creep strain rate versus stress of MPESAs in tensile load.

minimum creep rate with CoCrFeMnNi-ODS [68] at lower applied stresses. $AlTiVNbZr_{0.25}$ [96] was initially composed of the B2 phase, and Zr_5Al_3 particles had decomposed to an Nb_2Al-type sigma phase during creep testing. The creep behavior was argued to be controlled by viscous glide and dislocation interactions.

Overall, within the population of reviewed MPEAs creep tested in compression, the creep resistance of CoCrNi-based MPEAs was enhanced due to the introduction of strong and stable obstacles that impede deformation. Meanwhile, the creep behavior of non-CoCrNi-based MPEA further emphasizes that the creep response of MPEAs can be highly affected by the phase stability and microstructural evolution during creep.

Activation energy of MPEAs

The activation energy, Q, refers to the minimum energy required for a specific process to occur. For creep, Q is related to the deformation mechanism that occurs where a higher Q requires more energy for the mechanism to take place, leading to lower creep rates [10,28,68,73,75–77,82,99–101,108,109,116,119]. Since one material system can undergo deformation in a variety of ways with ranges of applied temperatures and/or stresses [28,76,82,89,101], Q can vary greatly. Frequently, a combination of the deformation mechanism, microstructural imaging, and other insights into the material is needed to fully understand the contributions to the activation energy. The activation energy of MPEAs is summarized in Table 6.

The activation energy is typically determined by calculating the slope of an Arrhenius plot of the creep-strain rate versus the inverse temperature [10,32,33,68,73,75–77,82,89,97,98,100–102,108,109,112,114,116,118,119]. This calculation holds the applied stress, through multiple experiments, constant in Eq. (1). Only a few materials had reported $n \approx 1$, such as MoNbTaVW [119] and CoCrFeMnNi + ODS (Y2O3 + Ti) [68], although the latter had an n closer to 2. Dobeš et al. suggested that diffusion is the creep mechanism because the activation energy is close to the lattice diffusion coefficient of Ni in CoCrFeMnNi [68]. This is likely due to the possible sluggish diffusion characteristic of MPEAs [152]. Interestingly, MoNbTaVW was shown to have an increase in the activation energy with an increased temperature; at the higher temperatures (1,123 – 1,173 K), the activation energy is similar to the calculated lattice diffusion process determined using Eq. (9) [119] below.

$$Q_{average} = \sum_{i=1}^{5} c_i Q_i \tag{9}$$

Where the average activation energy ($Q_{average}$) is the sum of the atomic fraction (c_i) times the lattice diffusion activation energy (Q_i) of the individual atomic species, i, in the MPEA [119].

When $n \approx 2$, the activation energy is related to GB sliding [32,33,75,82,102,118]. Interestingly, some MPEAs like $Al_{0.4}$CoCrFeMnNi [82] and CoCrFeMnNi + ODS (Y2O3 + Ti) [68] have $n \approx 2$, but the large grain size of the MPEAs suggests that the creep mechanism is still diffusion [68,82]. In both cases, the creep activation energy is similar to the calculated diffusion activation energy of the elements in the respective MPEA system [68,152]. In the case for $Al_{0.4}$CoCrFeMnNi, the large grain size (30 – 85 μm) suggests that the creep mechanism is not GB sliding [82].

For the cases of CoCrFeMnNi [73,101] and HfNbTaTiZr [114], again $n \approx 2$ but additional information shows that the materials follow dislocation glide. The grain size (12 – 30 μm) [101] and microstructural analysis [114] suggest that the activation energy should be understood from a different perspective. For GB sliding to be considered, the grain size should be less than 2 μm for MPEAs [101,153].

When $n \approx 3$, the creep-activation energy is related to the energy required for the dislocations to glide (called dislocation glide or solute-drag creep) [10,32,33,73,75–77,82,98,100,102,114,116,118]. This creep-deformation mechanism is common in solid solutions and thus is often the mechanism found in MPEAs due to them being solid solutions. The creep-activation energy is related to the diffusion activation energy of the solute atom although in equiatomic or near-equiatomic MPEAs, the specific species may be difficult to identify [101]. To help isolate the limiting element, Eq. (10) [101,102] can be used to calculate the diffusivity of each species [101].

$$\dot{\varepsilon}_{ss} \approx (\pi(1-\nu)kTD/6e^2Cb^5G)(\sigma/G)^3 \tag{10}$$

where $\dot{\varepsilon}_{ss}$ is the steady-state strain rate, ν is Poisson's ratio, D is the solute-diffusion coefficient, e is the solute–solvent size distribution, C is the solute concentration, and b is the Burgers vector [101]. Eq. (10) is

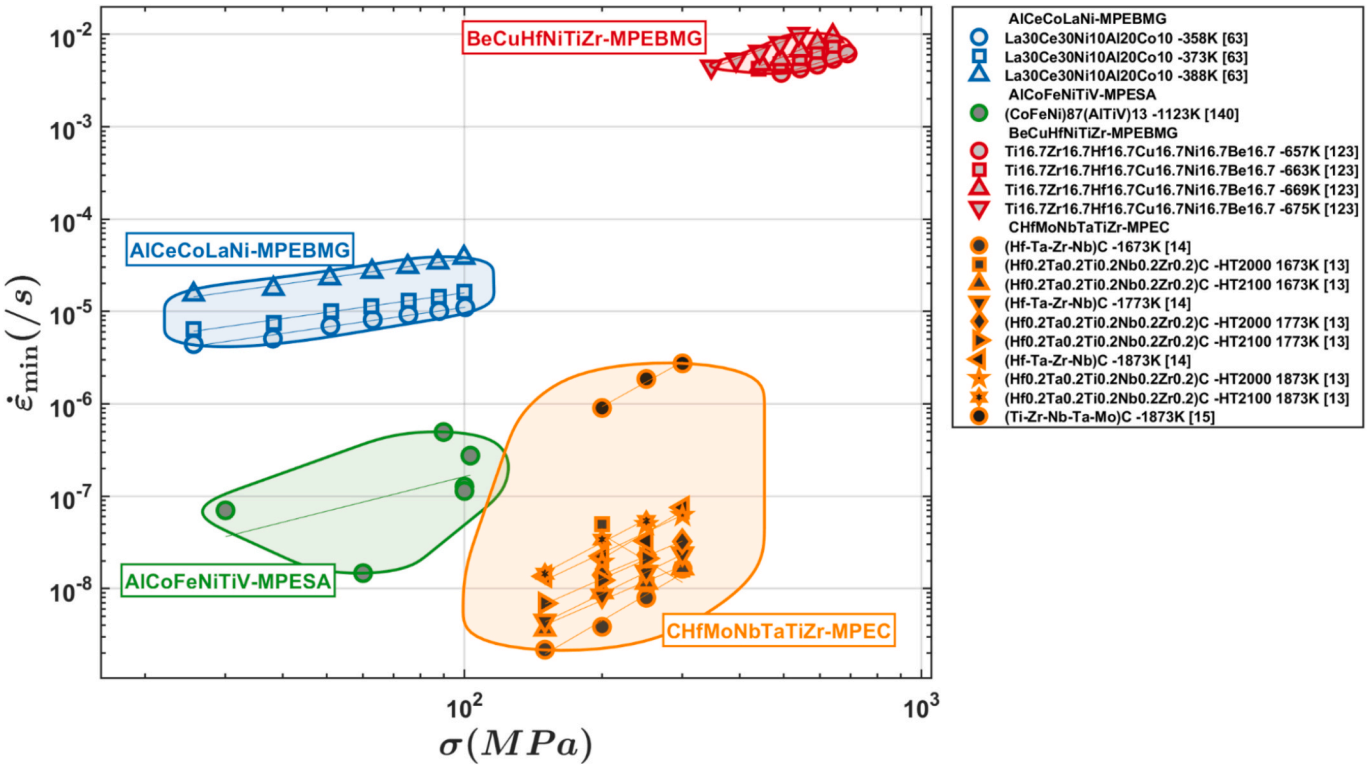

Fig. 8. Creep strain rate versus stress in compressive load for MPEBMGs, MPESAs, and MPECs.

Table 8
Summary of Activation Energy of some MPEBMGs and MPECs.

Composition	Test Method	Creep Activation Energy (Q) [kJ/mol]	Stress Exponent (n)	Ref #
Multi-principal-element bulk metallic glass (MPEBMG)				
$Zr_{64.13}Cu_{15.75}Ni_{10.12}Al_{10}$	N	$W_{STZ}/kT \approx 28.9$	—	[132]
$Zr_{46}(CuAg)_{46}Al_8$	N	29.6	—	[132]
$Cu_{46}Zr_{46}Al_8$	N	29.2	—	[132]
$La_{65}Al_{14}(CuAgNiCo)_{11}$	N	27.8	—	[132]
$La_{66}Al_{14}Cu_{10}Ni_{10}$	N	27.9	—	[132]
$La_{55}Al_{25}Ni_5Cu_{10}Co_5$	N	27.7	—	[132]
$Fe_{68}Mo_4Cr_1Y_5B_{22}$	N	30.6	—	[132]
$Co_{39.78}B_{26.2}Ni_{21.42}Si_{7.8}Ta_{4.8}$	N	30.5	—	[132]
(Ti-Zr-Nb-Ta-Mo)C	Com	486.3 ± 58.3	2.76 ± 0.31	[15]
$Ti_{16.7}Zr_{16.7}Hf_{16.7}Cu_{16.7}Ni_{16.7}Be_{16.7}$	Com	114.8 (1.19 eV)	—	[123]
$Al_{20}Ce_{20}La_{20}Ni_{20}Y_{20}$	T	3.9 (≲110 °C), 35.4 (>110 °C)	—	[129]
$Ni_{47.9}Al_{10.2}Co_{16.9}Cr_{7.4}Fe_{8.9}Ti_{5.8}Mo_{0.9}Nb_{1.2}W_{0.4}C_{0.4}$	T	290	—	[142]
$La_{57}Co_{18}Al_{25}$	N	397 – 50 (decreases with increasing holding time, 50 to 2000 s)	m = 0.022 – 0.385 (↑ with hold time)	[136]
$Zr_{55}Cu_{15}Ni_{13}Al_{17}$	N	923 – 104 (decreases with increasing holding time, 50 to 2000 s)	m = lower than La-Co-Al	[136]
$Ni_{60}Nb_{40}$	N	1149 – 104 (decreases with increasing holding time, 50 to 2000 s)	m = lower than La-Co-Al	[136]
$W_{68}Ru_{25}B_7$	N	1264 – 151 (decreases with increasing holding time, 50 to 2000 s)	m = lower than La-Co-Al	[136]
$Zr_{41.2}Ti_{13.8}Cu_{12.5}Ni_{10}Be_{22.5}$	T	17.3	—	[138]
$Be_{20}Cu_{20}Ni_{20}Ti_{20}Zr_{20}$ (H1)	T	13.9 (viscous flow in SHL)	—	[138]
$Ti_{16.7}Zr_{16.7}Hf_{16.7}Cu_{16.7}Ni_{16.7}Be_{16.7}$ (H2)	T	15.7 (viscous flow in SHL)	—	[138]
$Ti_{41}Zr_{25}Be_{34}$	N	32.7	m = 0.015 – 0.018	[120]
$Ti_{41}Zr_{25}Be_{28}Fe_6$	N	48.84	m = 0.012 – 0.014	[120]
$Ti_{41}Zr_{25}Be_{28}Al_6$	N	53.38	m = 0.008 – 0.010	[120]
$Ti_{41}Zr_{25}Be_{28}Ni_6$	N	35.66	m = 0.013 – 0.015	[120]
Multi-principal element ceramic (MPEC)				
C-263	T	400 ± 50	4.9 ± 0.1	[16]
C-264	T	550 ± 50	4.4 ± 0.7	[16]
$(Hf_{0.2}Ta_{0.2}Ti_{0.2}Nb_{0.2}Zr_{0.2})C$ (HT2000)	Com	177.3 – 194.8	2.0 1– 2.90	[13]
$(Hf_{0.2}Ta_{0.2}Ti_{0.2}Nb_{0.2}Zr_{0.2})C$ (HT2100)	Com	169.0 – 199.1	2.14 – 2.59	[13]
(Ta-Hf-Zr-Nb)C	Com	184 – 237	2.34 – 2.89 (1400 – 1600 °C)	[14]
$La_{30}Ce_{30}Ni_{10}Al_{20}Co_{10}$	T	ΔE = 35.7 – 44.2 (from ln(t) fit)	Power-law decay with exponents $\gamma_1 = 0.60$, $\gamma_2 = 0.40$, $\gamma_3 = 0.86$	[122]
$La_{30}Ce_{30}Ni_{10}Al_{20}Co_{10}$	T	$E_{creep} = 0.40$ eV ≈ 38.6 kJ/mol	n ≈ 1.40 – 1.44 (358 – 388 K)	[63]

T = tension; Com = compression; N = nanoindentation; STZ = shear transformation zone; W_{STZ} = energy barrier of an STZ upon yielding; SHL = superheated liquid.

used in this case to account for the various differences in solute versus solvent size while also accounting for the concentration of the solute atoms. These effects are not accounted for in Eq. (6) and (7) [154]. For each element in the MPEA, D can be used to determine Q using Eq. (11) [75,102,108].

$$D = D_i exp(-Q_i/RT) \tag{11}$$

where D_i is the diffusion coefficient, and Q_i is the activation energy of atom, i. Determining the lowest Q_i will give the limiting element of the overall activation energy. In many cases, Ni is the rate-controlling species [68,101,108].

Tension and compression experiments produce different creep-activation-energy results. For example, HfNbTaTiZr is lower in compression (226 ± 20 kJ/mol) [155] than it is for tension (273 ± 15 kJ/mol) [114] with only a small variation in n (2.8 for tension versus 3.3 for compression).

When systems have $n \approx 5$, the creep-activation energy is dictated by a dislocation climb [73,76,77,82,98,100–102,108]. For the material family of CoCrFeMnNi, the diffusion-activation energies for individual elements in the alloy system have been reported [152], so Q values larger than those reported values frequently refer to the activation energy for dislocation motion [77,99,109]. Dislocation climb is limited by the diffusion rate of vacancies to dislocations as well as dislocations interacting during cross slip [109].

For MPEAs with $n > 10$, the method of failure or deformation mechanism is not related to high-temperature creep. The determination of the activation energy does not contribute substantial insight into the deformation mechanisms occurring. Some researchers assert that the linear relationship does not break down for large values of n, since recrystallization could occur. This trend would result from significant diffusion, allowing for easier GB sliding [98]. Additionally, dynamic precipitation may occur, which leads to the calculated activation energy to be convoluted from the recrystallization and precipitation [98].

On the other hand, when indentation experiments were performed, large n and Q values were reported. Frequently, these experiments were done at room temperature and/or the load was only applied for a short period of time. In cases where the activation energy was reported, loading times of 120 s were applied at low temperatures (298 – 573 K) [32,33]. Although the CoCrFeMnNi and CoCrNi systems had realistic activation energies of 25 and 400 kJ/mol, respectively, their n values were high, ranging from 15 to 30 and from 15 to 90, respectively [32]. For the case of HfTaTiVZr and TaTiVWZr, both the n and Q were exceptionally large, being 20 – 120 and 20 – 140 and having activation energies of 925 and 1,000 kJ/mol, respectively [33]. Typical creep-activation energies of other MPEA materials range from 10 to 400 kJ/mol [10,27,28,68,73,75–77,82,89,97–102,108,109,112,114,116,119].

When n is only slightly greater than 10, utilizing the threshold stress can contribute to more accurate n and Q calculations. Eq. (12) [28] shows the modification below.

$$\dot{\varepsilon} = A(\sigma - \sigma_0)^{n'} exp(-Q'/RT) \tag{12}$$

where σ_0 is the threshold stress, and Q' is the adjusted activation energy. In these situations, multiple compounding effects could increase the activation energy to unrealistically high levels of 359 – 410 kJ/mol [98].

In some cases, the elastic moduli's effect on creep can be determined, which is done using the Garofalo equation [Eq. (8)] previously defined and explained in the previous section [10,118]. The creep-activation energy should not change when comparing Eq. (1) to (8) [10,28] since the stress is held constant in both cases.

The addition of particles, boron-nitride (BN), in the MPEA matrix may only have limited impact on the creep response of the material. At high stresses, the creep-activation energy is greater than the lattice-diffusion-activation energy of the individual element in the CoCrFeMnNi-BN system [28]. This trend suggests that the BN particles play a role in increasing the system's creep-activation energy. Similarly, in the $Al_{0.3}$CoCrFeNi system, B2 precipitates form at high temperatures and slows the dislocation motion. The precipitate formation results in an increase of the creep-activation energy [76].

Interestingly, in the Al_xCoCrFeNi system, a slight decrease in the creep-activation energy from the $Al_{0.15}$CoCrFeNi system is claimed to be the result of the BCC phase existing before the creep experiments begin [89]. Likely, the formation versus the pre-existence of the BCC phase

Table 9
Summary of Activation Volume (V^*) or STZ volume of some MPEBMGs.

Composition	Test Method	STZ Volume [nm^3]	Burgers Vector [nm]	Stress Exponent (n)	Ref #
Multi-principal element bulk metallic glass (MPEBMG)					
$Ti_{16.7}Zr_{16.7}Hf_{16.7}Cu_{16.7}Ni_{16.7}Be_{16.7}$	N	5.96	—	m = 0.00523 – 0.00597	[124]
$Zr_{50}Cu_{40}Al_{10}$ (As-cast)	N	1.80	—	m = 0.031	[134]
$Zr_{50}Cu_{40}Al_{10}$ (Relaxed)	N	2.44	—	m = 0.018	[134]
$Zr_{64.13}Cu_{15.75}Ni_{10.12}Al_{10}$	N	1.58 ± 0.28	—	—	[132]
$Zr_{46}(CuAg)_{46}Al_8$	N	1.42 ± 0.27	—	—	[132]
$Cu_{46}Zr_{46}Al_8$	N	1.75 ± 0.31	—	—	[132]
$La_{65}Al_{14}(CuAgNiCo)_{11}$	N	2.06 ± 0.36	—	—	[132]
$La_{66}Al_{14}Cu_{10}Ni_{10}$	N	1.94 ± 0.29	—	—	[132]
$La_{55}Al_{25}Ni_5Cu_{10}Co_5$	N	1.82 ± 0.24	—	—	[132]
$Fe_{68}Mo_4Cr_1Y_5B_{22}$	N	0.56 ± 0.09	—	—	[132]
$Co_{39.78}B_{26.2}Ni_{21.42}Si_{7.8}Ta_{4.8}$	N	0.67 ± 0.20	—	—	[132]
$Ti_{16.7}Zr_{16.7}Hf_{16.7}Cu_{16.7}Ni_{16.7}Be_{16.7}$	C	0.0277 – 0.0327	—	—	[123]
$Ti_{16.7}Zr_{16.7}Hf_{16.7}Cu_{16.7}Ni_{16.7}Be_{16.7}$	N	0.0137 – 0.0180	—	m = 0.00196 – 0.00450	[128]
$Ti_{16.7}Zr_{16.7}Hf_{16.7}Cu_{16.7}Ni_{16.7}Be_{16.7}$	Com	0.291 – 0.383	—	— (serrated flow studied qualitatively)	[128]
$Ta_{30.1}Ti_{36.8}Zr_{33.1}$ (AMEA)	N	6.17 – 10.94	—	m decreases w/ annealing	[130]
$Ta_{30.1}Ti_{36.8}Zr_{33.1}$ (AMEA)	N	0.0145 – 0.0182	—	m decreases w/ annealing	[130]
$La_{57}Co_{18}Al_{25}$	N	2 → 0.25 (↓ w/ t)	—	m = 0.022 – 0.385 (↑ with hold time)	[136]
$Zr_{55}Cu_{15}Ni_{13}Al_{17}$	N	2 → 0.20 (↓ w/ t)	—	m = 0.022 – 0.199 (↑ with hold time)	[136]
$Ni_{60}Nb_{40}$	N	1.3 → 0.15 (↓ w/ t)	—	m = 0.022 – 0.180 (↑ with hold time)	[136]
$W_{68}Ru_{25}B_7$	N	1.1 → 0.15 (↓ w/ t)	—	m = 0.021 – 0.106 (↑ with hold time)	[136]
$Zr_{50}Cu_{40}Al_{10}$	N	2.6 – 5.5	—	n decreases with energy state: Relaxed > As-cast > CR80 > CR90	[137]
$Ti_{41}Zr_{25}Be_{34}$	N	3.24	—	m = 0.015 – 0.018	[120]
$Ti_{41}Zr_{25}Be_{28}Fe_6$	N	4.98	—	m = 0.012 – 0.014	[120]
$Ti_{41}Zr_{25}Be_{28}Al_6$	N	6.02	—	m = 0.008 – 0.010	[120]
$Ti_{41}Zr_{25}Be_{28}Ni_6$	N	3.62	—	m = 0.013 – 0.015	[120]

Com = compression; N = nanoindentation; STZ = shear transformation zone; AMEA = amorphous medium-entropy alloy; ↑ = increases; ↓ = decreases; w/ t = with time.

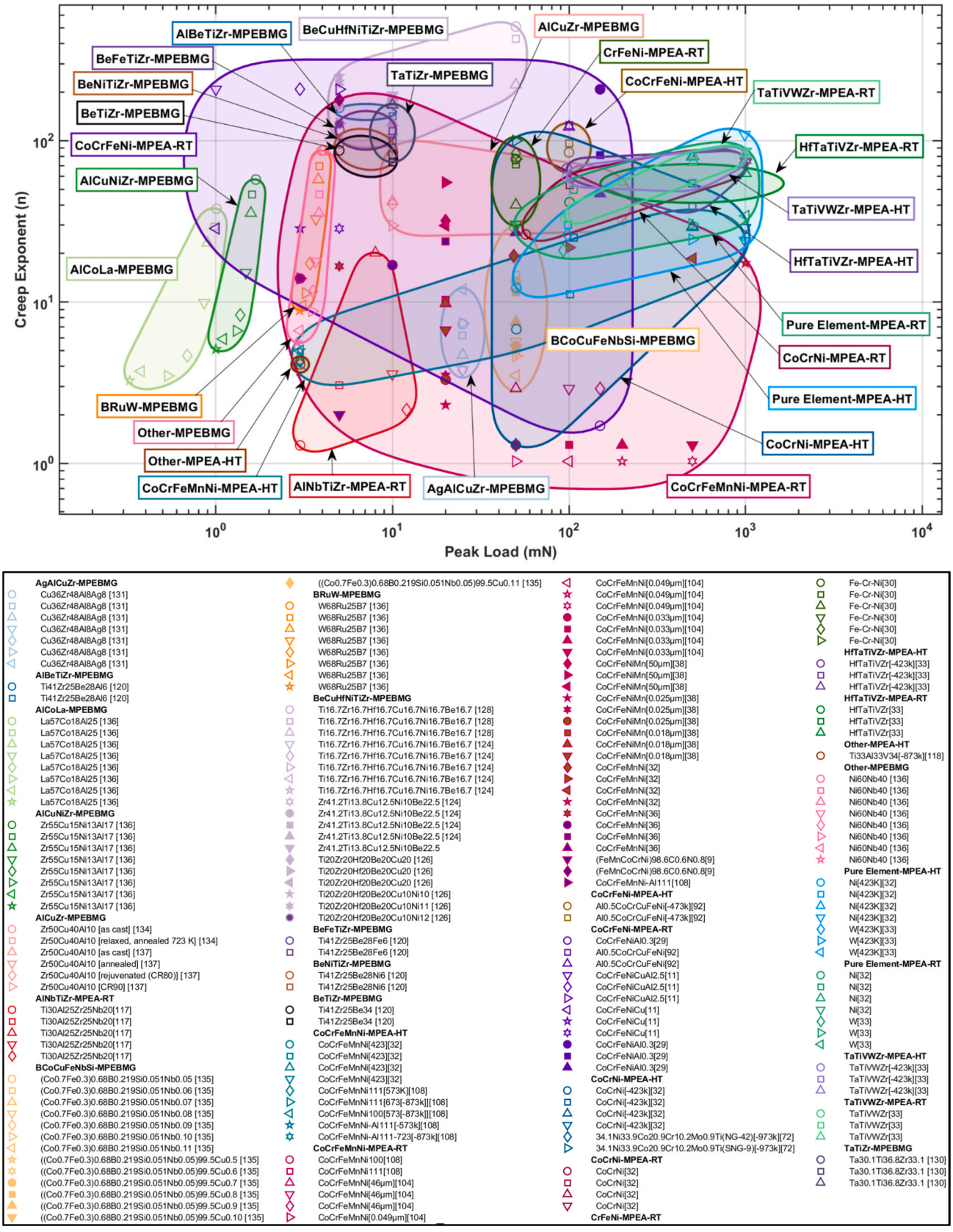

Fig. 9. Stress exponent versus maximum load of various MPEAs and MPEBMGs compared with pure elements, at room and elevated temperatures.

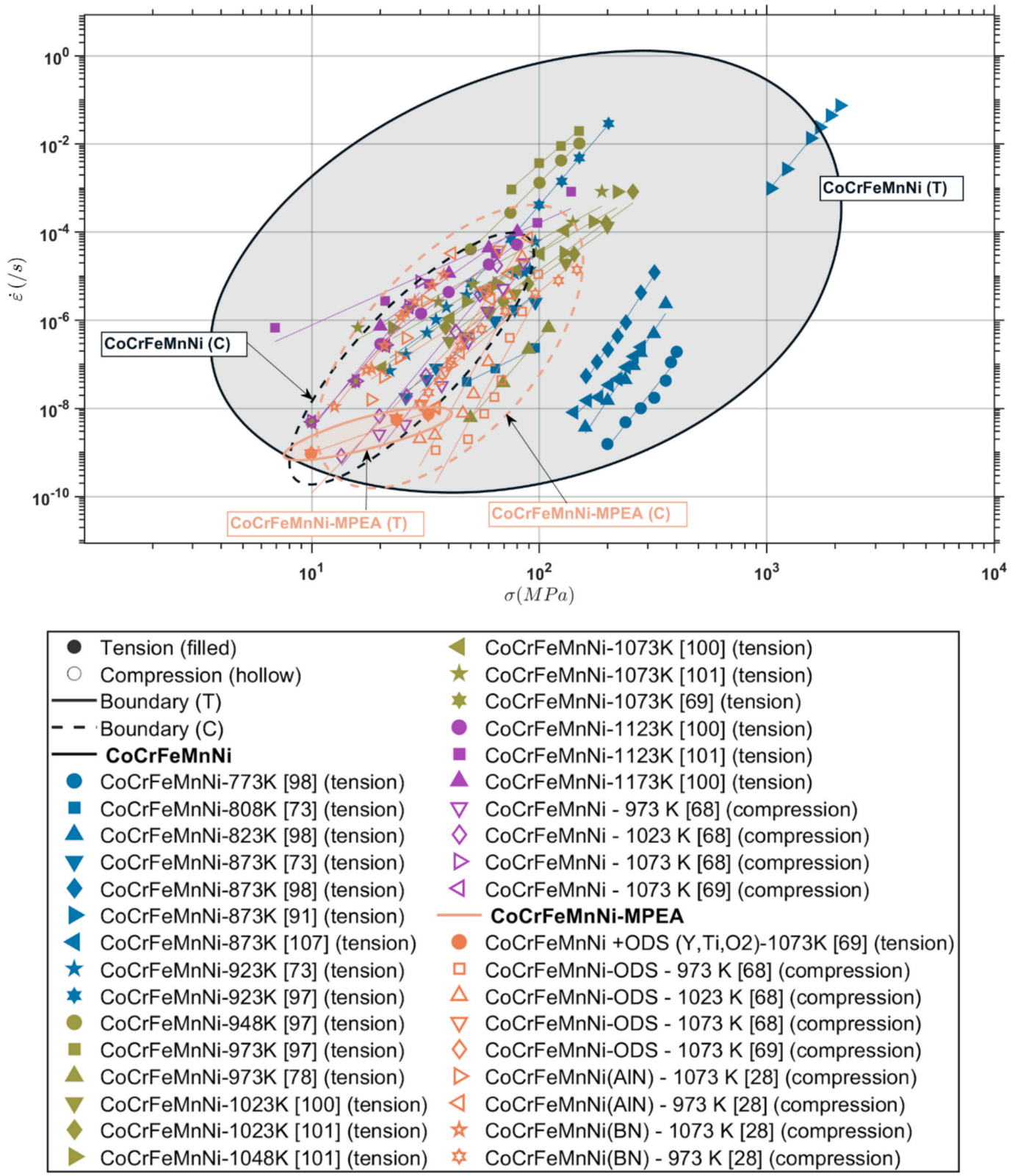

Fig. 10. Comparison of minimum creep rates obtained from tension and compression creep test for MPEAs. Only CoCrFeMnNi was included because it was the only composition tested in both tension and compression. Other compositions were not plotted to avoid over generalization.

directly affects the creep mechanism and therefore, the creep activation energy of the respective system.

Some MPEAs show a change in the creep-activation energy at a certain temperature regardless of the applied stress. The MoNbTaVW system has a $Q \approx 130$ kJ/mol at low temperatures (973 – 1,073 K) and a $Q \approx 330$ kJ/mol at high temperatures (1,073 – 1,173 K) and over a range of applied stresses from 130 – 520 MPa [119]. This result implies a change in the creep-deformation mechanism, regardless of the stress in

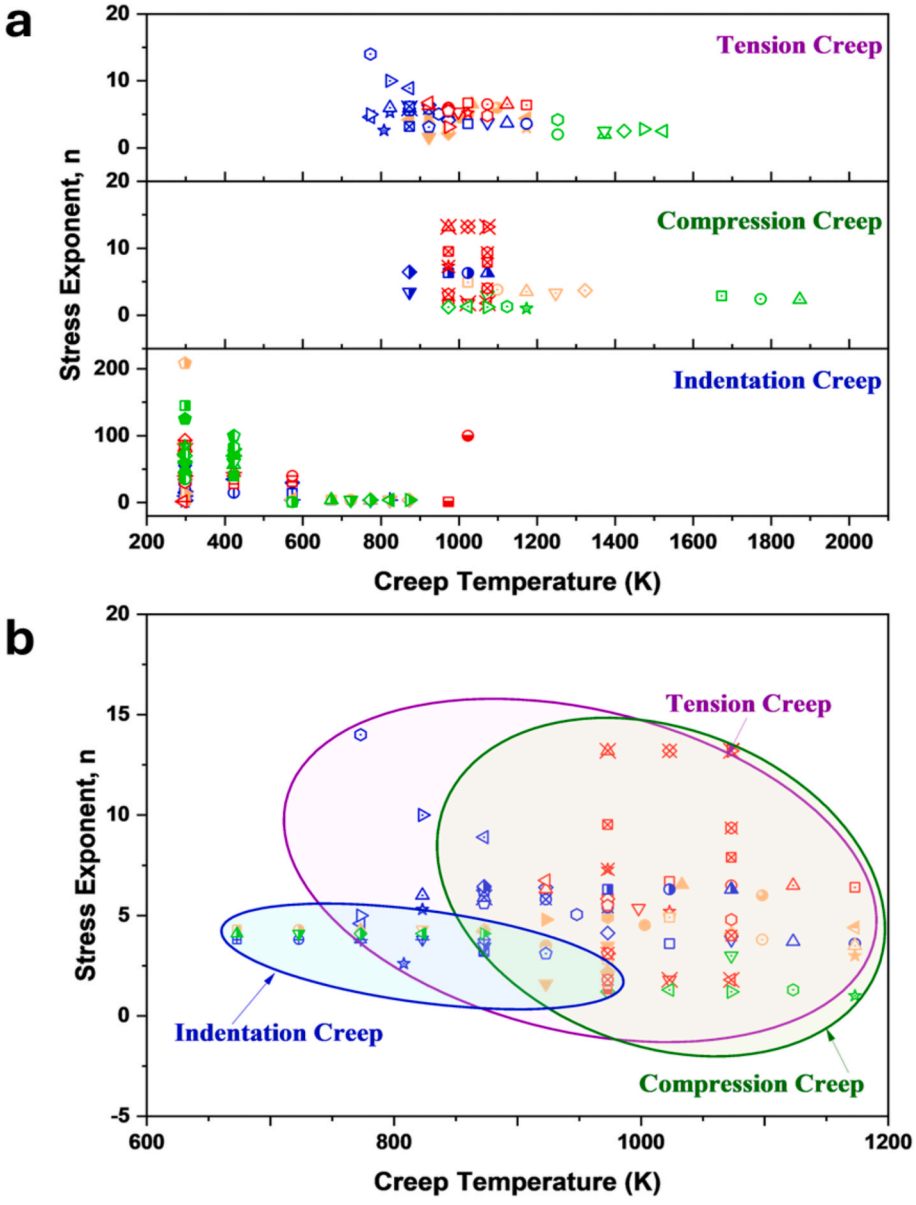

Fig. 11. Comparison of stress exponents of MPEAs obtained from tension, compression, and Berkovich-tip-nanoindentation creep tests.

Fig. 11. (*continued*).

the material, being entirely linked to the temperature of the experiment.

In many alloy compositions, phase changes or order–disorder transitions can limit the information that the creep activation energy can provide [75]. $L1_{2II}$ and $B2_{II}$ from the matrix likely affect the creep-activation energy as particles nucleate during the experiments [75], but the exact significance was not determined.

Regardless of the method of deformation, generally the higher the creep-activation energy, the better the creep resistance [32,112]. When compared to pure elements, lattice distortions, and slow diffusion in MPEAs lead to more dislocation interactions requiring a higher activation energy for them to move [33,97]. Additionally, since in MPEAs there is no single principal element, the slowest diffusing element should correspond to the activation energy of the entire alloy [82,108,153,156].

Creep-activation volumes of MPEAs

The activation volume (V^*) is the rate that the activation enthalpy decreases with respect to the stress at a given temperature [11,27,30,33,68,77,78,82,93–95,102,103,105,107, 108,111,117,157,158]. V^* affects the dislocation-rate-controlling mechanisms of plastic-creep deformation [42] and is calculated using Eq. 13 [27,68,77,102,108].

$$V^* = RT(\partial ln\dot{\varepsilon}/\partial\sigma) \text{ or } V^* = \sqrt{3}kT(\partial ln\dot{\varepsilon}/\partial\sigma) \quad (13).$$

where all variables were previously defined. V^* is related to the activation energy and stress exponent, but V^* is more closely related to microstructural-irreversible deformation [68]. V^* is typically presented when multiplied by the b^3 [27,30,33,68,77,78,101–105,111,117] but can also be given as a volume [11,33,108,117] or volume per mole [82]. All reference literature with a reported creep activation volume is summarized in Table 7.

For compression tests, two distinct V^* values were reported separately, both for the CoCrFeMnNi MPEA. One has a V^* ranging from 300 to 800 b^3 [68] while the other reported a V^* ranging from $41.2 - 52.9\ b^3$ [102]. In both cases, the Burgers vector is estimated to be 0.255 nm.

For tension experiments, the V^* is also calculated using Eq. 13. In the $Al_{0.6}$CoCrFeMnNi and $Al_{0.4}$CoCrFeMnNi systems, a larger V^* is correlated with a higher creep rate of $Al_{0.6}$CrCoFeMnNi [82]. In a different study, the V^* was used to eliminate possible creep-deformation methods [27]. In this case, V^* and Q increase as the temperature of the experiments increases, resulting from dislocation-pinning and depinning occurring on impurity particles [27]. For all the MPEAs in the CoCrFeMnNi family, a V^* between 100 and 1,000 b^3 is a reasonable value for forest-dislocation hardening, implying a dislocation-mediated creep-deformation mechanism [27,77,82]. A larger V^* implies that a larger volume of the material contributes to the thermal-activation process, leading to a longer rupture time [78].

In the nanoindentation experiments, a higher V^* was reported. It is mentioned that MPEAs have a more complicated diffusion process leading to slightly higher activation energies compared to conventional Ni-superalloys [108]. When considering the grain size, V^* increased when the grain size was decreased, meaning that when GBs dominate creep processes, there will be a lower resulting V^*. On the other hand, when dislocations dominate the creep process, there will be a higher V^* [111]. This effect was also seen in the CoCrNi system when nanocrystalline grains result in a small V^* ($\sim 0.8\ b^3$) versus the coarse grain samples having a large V^* ($\sim 4.6\ b^3$) [104].

Similarly, in the CrFeNi MPEA system, V^* shows an initial decrease (from $\sim 30\ b^3$ to $\sim 15\ b^3$) then returns to values around 30 b^3 as a function of aging time [30]. Unlike in previously mentioned materials, this is a result of secondary phases/precipitates changing in the size, morphology, and distribution [30]. After an aging time of 100 hr, the precipitates become too large to effectively pin dislocations although further aging results in new carbide precipitates forming to effectively pin the dislocation again [30].

V^* in the $Ti_{30}Al_{25}Zr_{25}Zr_{25}Nb_{40}$ MPEA varies based on the maximum load and loading rate of the indenter [117]. With a low loading rate, dislocation nucleation becomes easier. Hence, increasing the loading rate affects a larger area but only to a certain rate, and then V^* returns to a lower level [117]. This same effect was also seen in the CoCrNi and CoCrFeMnNi alloys [103].

With the addition of Al to CoCrCuFeNi, V^* increases greatly, from 0.08 nm^3 to 0.51 nm^3 [11]. These values were reported as a volume without a Burgers vector or lattice constant reported, so a comparison to other references is difficult. With that being said, the increase is linked to the transition from the FCC to BCC phases as the Al concentration is increased, for the CoCrCuFeNi and CoCrCuFeNi$Al_{2.5}$ MPEAs, respectively [11].

Multi-Principal-Element-Ceramics, -Bulk metallic Glasses, and -superalloys

Creep exponents in MPECs, MPEBMGs, and MPESAs

In addition to MPEAs, other material classes such as MPECs, MPEBMGs, and MPESAs have been tested for their creep properties although there are fewer studies on these types of materials. Fig. 7 presents the creep rate versus stress of some medium and high entropy MPESA are reported. First, the two MPESA based on the medium-entropy CoCrNi alloy ($Al_{0.9}Co_{19.5}Cr_{22.42}Fe_{0.27}Ni_{50.7}Mo_{3.49}Ti_{2.48}C_{0.24}$ and $Al_{2.21}Co_{19.06}Cr_{27.37}Fe_{0.24}Ni_{45.31}Mo_{3.33}Ti_{2.02}W_{0.17}C_{0.29}$, labeled as C-263 and C-264, respectively) are presented, which follow the conventional γ/γ' microstructure structure [16]. These two alloys were tested at slightly different temperatures of 1,153 K for C-263 and 1,173 K for C-264 and resulted in $n = 4.9$ and 4.4, respectively [16]. In both of these materials, the testing temperature is above where γ' is stable, so the dissolving γ' phase throughout the creep experiment leads to faster steady-state strain rates versus experiments at temperatures where γ' is stable [16]. In these alloys, there is strengthening due to the Orowan mechanisms related to the γ' precipitates, but since the C-264 has a higher temperature where γ' is stable, these mechanisms strengthen the material at high temperatures [16]. This feature is similar to another superalloy based on the CoFeNi medium-entropy alloy ($Co_{29}Fe_{29}Ni_{29}Al_{4.3}Ti_{4.3}V_{4.3}$) where the γ/γ' microstructure was present, and the stress exponent was reported to be 3.9 [140]. Here the deformation mechanism is linked to the γ' precipitates, and the as-printed alloys did not have an n as large as other similar superalloys fabricated in conventional methods [140]. Another MPESA ($Ni_{48}Co_{16.9}Cr_{7.5}Fe_{8.9}Mo_{0.9}W_{0.5}Ti_{5.8}Al_{10.3}Nb_{1.2}$) had the γ/γ' microstructure where the γ' appear as spherical shapes rather than cube-like structures ($n = 9.6$) [19]. The γ' precipitates elongated in the direction of the applied stress, and again, the γ' particles function as barriers to dislocation motion [19]. These three studies show adjacent efforts to improve upon MPESA but are not studied at the same rate as MPEMs. Other studies reported creep experiments without showing the traditional results for creep to compare with other materials [17,106,139,142,159].

Similarly, MPECs have been studied for their creep properties. Because MPECs operate and are tested in different temperature and stress regimes, MPECs cannot be directly compared with MPEAs and MPESAs. Nevertheless, for context, some MPECs' creep strain rate is presented in Fig. 8. These studies must utilize compressive loading conditions to account for the brittleness associated with ceramics [13–15]. (HfTaTiNbZr)C was investigated, revealing that stress exponents are affected by the prior heat treatments of the material where the heat treatment at 2,273 K had $n = 2.90$, 2.01, and 2.86 at creep experiment temperatures of 1,673, 1,773, and 1,873 K, respectively while the heat treatment of 2,373 K resulted in $n = 2.59$, 2.18, and 2.14 with respect to the creep experiment temperatures [13]. Here the stress exponent is decreased by n about equal to 0.5 due to the higher temperature heat treatment prior to the creep experiment except at the intermediate creep experiment temperature of 1,773 K [13]. Interestingly, this trend does not lead to a large difference in the steady-state creep

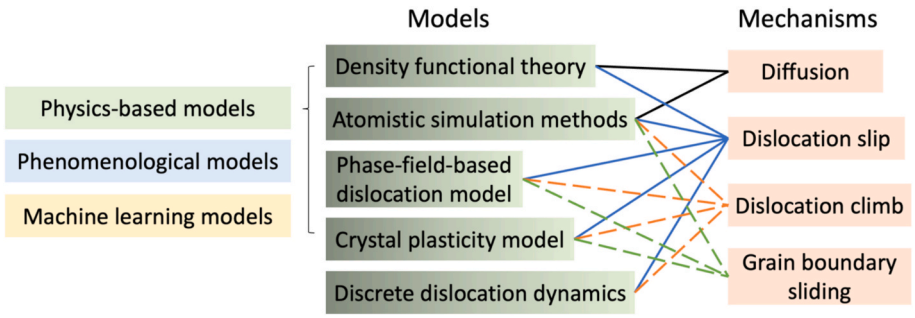

Fig. 12. A summary of different computational models and various mechanisms involved in creep. On the right-hand side, solid lines connect models and mechanisms that have been realized in MPEAs, while dashed lines link models and mechanisms that have been connected in traditional alloys but not yet in MPEAs.

rates between heat-treated materials [13]. In a similar manner, the higher heat-treatment temperature decreased the activation energy of the material (Q = 177.3 kJ/mol to 169.0 kJ/mol at 200 MPa and Q = 194.8 kJ/mol to 180.7 kJ/mol at 250 MPa) [13].

A (HfNbTaZr)C MPEC was also studied, revealing an activation energy of 212 kJ/mol, which is similar to the activation energy of NbC of 240 kJ/mol [14]. Here it was found that the steady-state creep rates of the MPEC were better than NbC, ZrC, and TaC at 1,773 K and 1,873 K [14]. Lastly, (MoNbTaTiZr)C compressed at 200 MPa had an activation energy of 486 kJ/mol and n = 2.76 at a temperature of 1,873 K [15]. This alloy showed steady-state strain rates faster than (HfNbTaZr)C previously mentioned with a difference from 3.86×10^{-9} /s to 2.13×10^{-8} /s at the low temperature and stress range and from 7.56×10^{-8} /s to 2.74×10^{-6} /s at the high temperature and stress range for (HfNbTaZr)C and (MoNbTaTiZr)C, respectively [14,15]. This feature shows that for compressive creep resistance, (HfNbTaZr)C is a superior MPEC.

The $Ti_{16.7}Zr_{16.7}Hf_{16.7}Cu_{16.7}Ni_{16.7}Be_{16.7}$ MPEBMG [123] was creep tested using a compressive stress jump test at a temperature range from 657 to 675 K. The creep behavior of $Ti_{16.7}Zr_{16.7}Hf_{16.7}Cu_{16.7}Ni_{16.7}Be_{16.7}$ is controlled by STZ activation. The activation energy is 1.19 eV, which is relatively low compared to other BMGs [160], indicating easier STZs activation. The $Ti_{16.7}Zr_{16.7}Hf_{16.7}Cu_{16.7}Ni_{16.7}Be_{16.7}$ MPEC undergoes a transition from Newtonian to non-Newtonian flow with increasing strain rate. Creep in $La_{30}Ce_{30}Ni_{10}Al_{20}Co_{10}$ [63] was studied under a tensile load from 25 to 100 MPa and at temperature range from 358 to 403 K. $La_{30}Ce_{30}Ni_{10}Al_{20}Co_{10}$ is also deformed by the STZs activation. At a lower temperature, isolated STZs randomly activate, leading to reversible and anelastic strains. With increasing the temperature and stress, STZs interact with other STZs, which form larger deformation zones, leading to an irreversible viscoplastic strain and quasi-steady-state creep [63].

The effect of physical aging on MPEBMGs was studied by Duan et al. [121] and Zhang et al. [122], which reported the reduction of available STZs after physical aging. Duan et al. investigated the effect of physical aging on the creep behavior of $Pd_{20}Pt_{20}Cu_{20}Ni_{20}P_{20}$ at 503 K for 0.5 to 24 h [121], while Zhang et al. conducted the physical aging on $La_{30}Ce_{30}Ni_{10}Al_{20}Co_{10}$ at 363 K for up to 1.8 h. With increasing aging time, a significant decrease in the creep strain was observed, the material became stiffer, and the relaxation behavior stabilized. Stabilized relaxation behavior means that the distribution of STZs stabilizes so the creep curve is predictable and reproducible, which was consistently observed in the creep curve reported by Duan et al. [121]. This decrease in the creep strain is caused by the annihilation of the "soft" STZs and integration of dispersed STZs into the elastic matrix during physical aging. Then, only the "stronger" STZs that need longer relaxation time will be left during the creep test. However, the lower creep rate in the aged sample is only because there are fewer STZs left during creep. The lower creep rate does not mean that the material will last for longer creep time because it is observed that the creep strain of the aged samples is significantly reduced with increasing aging time [121,122].

During creep, MPEBMGs deform like BMGs, however due to the high configurational entropy from the multi-element composition, MPEBMGs typically have greater strength, lower activation energy, and higher resistance to crystallization, which help maintain glassy behavior at elevated temperature [63,123].

Activation energy and activation volume in MPECs, MPEBMGs, and MPESAs

Although the stress exponent is the most commonly reported for multi-principal element materials, the activation energies also give insight into the materials creep behavior. The activation energy of MPECs and MPEBMGs are listed in Table 8. Only MPECs and MPEBMGs are listed in Table 8 because there is no reported value for activation energy on MPESAs in the literature we reviewed. For the MPEC materials reviewed, only (MoNbTaTiZr)C reported that the activation energies was found to be 486.3 ± 0.31 kJ/mol for an applied stress of 200 MPa [15]. For this ceramic, the Q was found to be higher than the self-diffusion of the elements and C in their respective mono-carbides [15]. This feature implies that C must be diffused in the MPEC [15]. Additionally, the self-diffusion of Mo in MoTaC was shown to be less than Q for the MPEC leading to the conclusion that Mo could be diffusing in areas of Mo, Ta, and C segregation, [15]. These insights into the diffusion processes during creep give a better understanding of the creep mechanisms at play in the MPEC. From the conclusions of this single study, it can be concluded that other MPECs will primarily have diffusion of C and possibly of the smallest metal element in the material.

In MPEBMGs, the activation energy refers to the minimum energy that is required to activate a STZ under a given temperature and load. An STZ is also known as a flow unit [121], deformation unit [121], liquid-like zone [123], and relaxation unit [132]. From the reviewed literature, there are many different methods to calculate the activation volumes based on the testing conditions [63,121–123,129,132,136].

Tong et al. [123] used Arrhenius analysis as shown in Eq. (14), to calculate the Q of the creep to overcome obstacles during a compressive stress-jump test for the $Ti_{16.7}Zr_{16.7}Hf_{16.7}Cu_{16.7}Ni_{16.7}Be_{16.7}$ MPEBMG in the temperature range from 657 to 681 K.

$$\eta_N = \eta_0 exp\left(Q_{app}/kT\right) \tag{14}$$

The activation energy was found to be 1.19 eV, which is smaller than traditional BMGs [160,161]. The smaller value was because the test temperature was below the glass-forming temperature [123]. This allowed the MPEBMG to act more like an alloy rather than a metallic glass.

Duan et al. [121] conducted creep tests for $Pd_{20}Pt_{20}Cu_{20}Ni_{20}P_{20}$ at 503 K under tensile loads. Duan et al. assumed that each STZ is associated with the relaxation time (t) and following Arrhenius behavior, the activation-energy spectrum, as shown in Eq. (15) was obtained from continuous regularization technique for an inverse problems (CONTIN) method [162].

$$P(E_a) = -(1/K_BT)(d\varepsilon(t)/dlnt) \quad (15)$$

CONTIN method is a mathematical technique that solves inverse problems to reveal the underlying distribution of the relaxation process. The activation-energy spectra show an increasing trend with increasing load, indicating that larger STZs are activated with increasing loads. The activation-energy spectra shifted to a higher value with increasing aging time, indicating "stronger" STZs are activated [121].

Zhang et al. [122] conducted a tensile creep test for $La_{30}Ce_{30}Ni_{10}Al_{20}Co_{10}$ at 363 K and used a directional structural relaxation (DSR) [163] model to derive Q and obtain the activation energy spectra. Q is increasing with the product of the relaxation centers volume density per activation-energy interval, activation volume, and orienting influence of an applied stress, indicating more STZs are progressively activated during creep. Interestingly, the activation-energy spectra also shifted to a higher value with increasing pre-aging time, indicating that STZs with higher barriers are activated because the smaller ones either stabilized or annihilated during aging. Interestingly, the fact that the strain rate also decreases with increasing aging time is reasoned to be caused by fewer STZs left after aging. However, lower creep rates in BMGs do not translate to longer creep time due to the fewer and softer STZs that are left after aging [122].

Wang et al. [136] conducted nanoindentation tests on the $La_{57}Co_{18}Al_{25}$, $Zr_{55}Cu_{15}Ni_{13}Al_{17}$, $Ni_{60}Nb_{40}$, and $W_{68}Ru_{25}B_7$ MPEBMGs at room temperature, and used the cooperative shear model (CSM) [164] to calculate the activation energy and activation volume. Wang et al. found that with increasing holding time, the activation volume and energy decrease while the strain rate sensitivity increases. The finding alludes to a transition from larger STZs available with short holding time into a more uniform and stable flow, indicating that there are smaller and more distributed STZs available with increasing holding time [136].

It is well established that the activation energy in MPEBMGs reflects the energy barrier to activate STZs, which governs creep, presenting the cooperative atomic arrangements. In contrast to that, in crystalline materials, the activation energy during creeps corresponds to the type of creep deformation, alluding to atomic diffusion or dislocation motion. MPEBMGs also differ from metallic alloys where heat treatments could potentially induce higher creep resistance from precipitation strengthening. In MPEBMGs, prior heat treatments "spend" the lower-energy STZs, leaving the higher energy STZs to activate during creep.

Lastly, the activation volume is the last major creep property commonly reported for MPEM. The activation volume for MPEBMGs is listed in Table 9. Only MPEBMGs are listed in Table 9 because there are no reported values for the MPECs and MPESAs in the literature we reviewed. In MPEBMGs, an activation volume is associated with the rate-limiting deformation unit and therefore, quantifies the sensitivity of the creep rate to an applied stress [63]. However, what is often reported for BMGs is the STZ volume (Ω_{STZ}), which is the physical estimate of STZ size and is not directly sensitive to the applied stress [124,130,136,137]. Zhang et al. [63] performed a tensile stress-jump creep test on $La_{30}Ce_{30}Ni_{10}Al_{20}Co_{10}$ with 25 – 100 MPa and 358 – 388 K. The activation volume was calculated using Eq. (16) [165]. The activation volume increases with increasing temperature and stress due to larger or more STZs being activated, leading to higher creep rates [63].

$$V^* = 3kT/n\sigma \quad (16)$$

The STZ volume can be estimated by calculation using a CSM model [164] by utilizing the pop-in statistics from spherical nanoindentation tests. By extracting the activation volume (V^*) from the slope of $ln\left\{ln(1-f)^{-1}\right\}$ vs. τ_{max} and then deriving from Argon's theory and Johnson-Samwer [166], the STZ volume can be extracted with Eq. (17).

$$\Omega = (V^*\tau_{C0})/\left(6C\mu\gamma_C^2\xi(1-\tau_{CT}/\tau_C)^{1/2}\right) \quad (17)$$

Tong et al. [128] reported a decreasing STZ volume with increasing the loading rate of the TiZrHfCuNiBe MPEBMG. The findings of this study indicate a transition from a larger-sized STZs activation at lower loading rates into a smaller and more homogeneous distribution flow of the STZs activation with higher loading rates.

Another method to estimate the STZ volume using the CSM model is with primary input of the strain-rate sensitivity and mechanical properties from a nanoindentation test is by using Eq. (18), where R_0 and ξ are constants with values of ¼ and 3 [166], respectively. τ_{CT} and τ_C are shear stresses at 0 K and testing temperature, respectively. γ_C is the yield strain.

$$\Omega_{STZ} = kT/C_0mH, \text{ where } C_0 = 2/\sqrt{3}\left(R_0\xi G_0\gamma_C^2/\tau_C\right)(1-(\tau_{CT}/\tau_C))^{1/2} \quad (18)$$

Wang et al. [124] reported the higher STZ volume in the TiZrHfCuNiBe MPEBMG (5.96 nm^3) compared to Vitreloy 1 BMG (4.26 nm^3) and lower strain-rate sensitivity in the former (0.00523) than the latter (0.00758). This finding indicates that the TiZrHfCuNiBe MPEBMG is less sensitive to applied stress. Wang et al. [136] reported that STZ volumes of $La_{57}Co_{18}Al_{25}$. $Zr_{55}Cu_{15}Ni_{13}Al_{17}$, $Ni_{60}Nb_{40}$, and $W_{68}Ru_{25}B_7$ decrease with increasing the holding time. The study also found the time-dependent transition of the deformation mechanism where during the earlier stage of creep, there are fewer but larger STZs activated, while at a later stage more but smaller STZs are activated. Tao et al. [137] reported the decrease in the STZ volume with the structural state of $Zr_{50}Cu_{40}Al_{10}$ from a relaxed state (annealed, lower energy) to the rejuvenated state (cold rolled, higher energy). This finding implies easier activation of STZs in the higher energy state of $Zr_{50}Cu_{40}Al_{10}$ due to a greater free volume and heterogeneity. Although these studies are probing different aspects of MPEBMG deformation, we can conclude that smaller STZ volumes are associated with easier STZ activation.

Comparison of nanoindentation creep behavior of MPEAs and MPEBMGs at several temperatures

A comparison of the calculated n versus the applied load obtained from nanoindentation-creep tests of MPEAs and MPEBMGs is shown in Fig. 9. These tests include various types of indentation tests, materials, and processing conditions. For the CoCrFeMnNi MPEA family of materials, a large range of stress exponents can be determined from a given applied load during the nanoindentation test. For many experiments, changing the applied load does not dramatically vary n [11,32,36,104]. On the other hand, in some cases the same applied stress can result in different stress exponents, likely due to other changes in the experimental set-up [29,36,38,92,108]. These two phenomena can be seen in other compositions as well, such as HfTaTiVZr and TaTiVWZr [33], CrFeNi [30], $(FeMoCoCrNi)_{98.6}C_{0.6}N_{0.8}$ [9], and B-Co-Cu-Fe-Nb-Si MPEBMG [135]. These results give strong evidence that the applied load from the nanoindenter does not correlate strongly with the deformation mechanism determined from phenomenological creep results. However, it is interesting to note that most of the materials tested with higher peak loads contain Ti, Ta, and Zr, while most of the materials tested with lower peak loads contain Al.

The peak load versus creep exponent for pure Ni and W were also included in Fig. 9, where the values are similar to those for the MPEAs. The pure metals, Ni [32], and W [33], were tested at room temperature and 423 K and only showed 32% and 22% stress-exponent difference on average, respectively. Overall, there are no significant trends from the applied load to the creep-stress exponent.

In very few studies, nanoindentation was used to determine the creep properties. Li et al. [131] also reported findings with the Berkovich nanoindentation test at room temperature for $Cu_{36}Zr_{48}Al_8Ag_8$ at six different locations. Although MPEBMGs are amorphous, the structure is heterogeneous at the atomic scale, leading to varied free volumes, local packing densities, and STZs concentrations. Deformation serrations during the nanoindentation tests were also observed in this study,

indicating the heterogeneity of the structure. Deformation serrations (non-uniform and inhomogeneous flows) are sudden displacement bursts in depth versus time, which indicates intermittent and localized shear events associated with STZ activations, collapsing of free volume, and local instability.

Comparison of different creep-test methods

The most common experimental set-up for creep experiments is tension, followed by compression. Fig. 10 shows the comparison of the minimum creep rate versus the applied stress for many MPEAs. Only CoCrFeMnNi was directly studied in both tension and compression, and the variation of the minimum creep rates observed is minimal. Overall, the minimum creep rate at a given applied stress will vary more due to other factors than the direction of the applied uniaxial load. For example, the study of the difference of creep behavior under tension and compression is relevant in some magnesium alloys due to the formation of precipitates during compression creep [167], different twinning behavior under tensile and compressive load [168], and for applications where bending load is relevant [169]. This means future experiments requiring one experimental set-up versus the other for external reasons, would not suffer from skewed data from that set-up.

Nanoindentation tests to observe creep behavior have become more popular in recent years due to the improvement in experimental techniques and instruments [3,170,171]. However, there are many variables in nanoindentation creep experiments that need to be carefully controlled and considered during the test, especially at temperatures above room temperature [172]. Challenges of doing nanoindentation creep testing include maintaining the thermal equilibrium of the indenter during the test, thermal drift, effect of different indentation sizes, and sample inhomogeneity [173]. Thermal drift is a phenomenon in indentation tests where the measured displacement comes from the thermal expansion of the indenter due to fluctuations of temperature rather than the deformation of the tested material. Thermal drift may occur at room temperature [172] due to instrument's expansion or contraction but become more severe even at temperatures as low as 473 K [174]. Thermal drift correlates closely with the speeds of indentation tests [173]. It is fairly difficult to maintain a low thermal drift and quick indentation tests [175]. Due to this challenge, many of the creep-behavior studies performing nanoindentation tests were done at room temperature
[9,11,29,30,34,36–38,90,91,94,103,104,110,111,113,117].

Lee et al. compared the validity of room-temperature nanoindentation-creep measurements from a spherical indenter and three-sided pyramidal indenter (Berkovich tip) [104]. In the experiment, Lee et al. using a Berkovich tip indenter [104]. The stress exponent was found to be in the range of 16.95 to 28.47, while using a spherical tip gives a stress exponent of 1 to 1.30. The stress exponent increases with a reducing applied stress, which contradicts the classical creep theory where a higher applied stress tends to have a greater n [104]. One of the problems on the sharp-tipped indenter, such as Berkovich tip, is that the characteristic indentation strain and stress are unique and independent of displacement by creep due to the geometrical self-similarity of the indenter [104]. The ratio of the indentation depth to contact area is constant, making it impossible to define a strain-rate change as a function of stress because stress and strain fields under the indenter tip are invariant to scale [104].

A number of studies have reported that nanoindentation-creep tests may be varied because the tested materials is still in the primary creep regime due to the relatively short-test duration of most indentation tests, large difference of the stress and strain rate in the area near the indenter, and the continuous size expansion of the deformation zone [3,175]. Goodall et al. [175] conducted creep tests and repetition tests at room temperature on 15 different materials using constant load and found no correlation between the measured and reported values [173,175]. Goodall et al. [175] concluded that based on the results of the study, the methodology employed is inherently unreliable and is subject to errors from small variations of testing conditions or data interpretation. Primary sources of error may be from the fact that it is likely that the material is still in the primary creep regime. Hence, the strain rates tend to be larger and more varied compared to where the sample is in the secondary-creep regime. Phani et al. [3] conducted a similar experiment on pure Al, plotting the temperature-compensated uniaxial strain rate versus stress normalized to Young's modulus of the creep test obtained from Berkovich indentation creep and uniaxial creep tests. The Berkovich-tip indenter generates approximately 8% of the strain while the uniaxial creep test was conducted at constant strains of 10% and 70%. The temperature-compensated strain rate of the indentation test matches well with the uniaxial test at a 10% strain rate but neither matches with the uniaxial test at 70%. The result suggests that at room temperature, both the uniaxial test at a 10% strain and the nanoindentation test did not reach steady-state creep at temperatures below 373 K. This study suggests that the Berkovich-tip indentation-creep test, which generates a nominal strain of 8% for pure Al, does not reach a steady-state indentation creep at temperatures below 373 K.

Fan et al. [9] conducted high-throughput nanoindentation on $(CoCrFeMnNi)_{98.6}C_{0.6}N_{0.8}$, and the testing caused several different microstructural features. The microstructures prior to nanoindentation tests are nanograins, nanotwins, and dislocation cells due to cold rolling. The microstructural features found near the indented area are divided into five groups, nanograins and nano twins dominated (group I), nanograins and dislocation cells dominated (group II), nanotwins dominated (group III), nanotwins and dislocations cells dominated (group IV), and dislocation cells dominated (group V). The nanoindentation tests revealed that different areas might have largely different stress exponents and creep rates, highly correlated with the local microstructural heterogeneity [9].

To compare the creep behavior of MPEAs obtained from different testing methods, Fig. 9 presents the stress exponent versus the creep-test temperature obtained from tension creep, compression creep, and Berkovich tip nanoindentation-creep experiments. Based on the collected literature included in Fig. 11 (a), the tension creep test, compression creep test, and nanoindentation creep test were conducted at 773 K to 1523 K, 973 K to 1,873 K, and 298 K to 1,023 K, respectively. Variation of stress exponents within the same composition at the same creep temperature may come from the different load levels.

Evaluating the difference of the stress-exponent values using the highest versus lowest reported value at the same temperature, for example using CoCrFeMnNi, tension-creep, and compression-creep tests have differences in n of 9.4 at 773 K (max. stress 400 MPa) and 3 at 873 K (max. stress 325 MPa), respectively. Meanwhile, Berkovich-tip nanoindentation creep tests have a stress exponent difference of 27.7 at room temperature (max. Load 20 mN or max. stress of 2.8 GPa with an indentation depth of 530 nm) and 20 at 423 K (max. Load 1,000 mN or max. stress of 333 GPa with indentation depth of 350 nm). The significantly larger difference of creep exponents in the Berkovich nanoindentation creep test compared to the difference in tension and compression creep suggests that the former is valid only for a localized area [9] and might be subject to large error due to testing conditions [104,172,173,175].

Fig. 11 (b) presents the same dataset in Fig. 9 (a) on different scales (600 to 1,200 K) and formats where the dataset obtained from the tension creep, compression creep, and Berkovich- tip nanoindentation-creep tests are overlapped. Qualitatively we can observe that the CoCrFeMnNi, CoCrNi, and $Al_xCoCrFeMnNi$ variants, which are tested at similar temperature ranges, have good agreement as most of the data points are overlapping. Meanwhile, in this temperature range, the only reported data of CoCrFeMnNi is CoCrFeMnNi-{111}, a study reported by Tsai, et al. [108] which have lower creep exponents than those from tension and compression creep. Note that more than half of the nanoindentation-creep tests were performed at room temperature.

In summary, there is a good agreement between creep behavior

obtained from tension-creep and compression-creep tests. Meanwhile, there is not enough reported data on the nanoindentation-creep test in the temperature range where tension and compression creep tests were performed to make a good comparison. Most of the reported creep behavior from nanoindentation-creep tests are conducted at room temperature, which gives large variance in the creep exponent for the same material composition. The large variance may come from testing errors, such as the thermal drift, or sensitivity to microstructural features at which the nanoindentation-creep test is conducted. Therefore, direct comparison to nanoindentation creep is currently not robust and nanoindentation creep should be treated primarily as a local, comparative screening tool unless the obtained data has been validated against uniaxial creep under matching temperature conditions and standardized analysis protocols.

Computational work on creep in MPEMs

This section is primarily dedicated to MPEAs. One study is reviewed on MPESAs. To the best of the authors' knowledge, no computational work exists for creep in MPECs or MPEBMGs.

Physics-based models

Three physics-based models — atomistic-simulation methods, phase-field modeling, and the crystal-plasticity (CP) method — can be directly used to study creep in metallic materials (Fig. 12). However, compared to pure metals and dilute alloys, computational studies of creep in MPEAs remain scarce [176]. For instance, to the best of the author's knowledge, only three pieces of atomistic-simulation work have examined creep in MPEAs. In the CoCrNi medium-entropy MPEA, Huang et al. [177] found that while lattice distortion has negligible effect on the creep behavior, chemical short-range order (CSRO) significantly impedes creep deformation by hindering atomic diffusion and dislocation glide. The CSRO is typically described using the Warren-Cowley SRO order parameter, α_{ij}^{n}, defined in Eq. (19) [177–179].

$$\alpha_{ij}^{n} = (p_{ij}^{n} - c_j)/(\delta_{ij} - c_j) \tag{19}$$

where i is the atom type of interest and j represents a different type of atom, n is the nth nearest neighbor shell of an i-type atom, p_{ij}^{n} is the probability of a j-type atom being found in the nth shell of an i-type atom, c_j is the concentration of the j-type atoms, and δ_{ij} is the Kronecker delta function. Also, in CoCrNi, Xu et al. [180] further revealed that CSRO inhibits dislocation motion more severely than diffusion and induces a stress-dependent transition of the dominant-creep mechanism, a phenomenon not observed in its random solid-solution counterpart. In the medium-entropy FeCrNi MPEA system, Kumar et al. [181] predicted creep curves under various temperatures and stress conditions.

In addition, only one phase-field modeling study has examined creep in MPEAs. Gao et al. [182] found that the size of Cu-rich particles in the CrCuFeNi MPEA positively influences creep strain. Similarly, only one CP study on creep in MPEAs has been conducted. Specifically, Liu et al. [183] investigated four FCC MPEAs and determined that spherical voids enhance creep resistance more than cubic voids of the same size. Given the extensive phase-field and CP research on the creep behavior of traditional alloys, such as Ni-based superalloys, further studies on MPEAs are needed to deepen our understanding of their creep mechanisms.

Although limited computational efforts have been devoted to directly simulating creep in MPEAs, more computational studies have explored phenomena closely related to creep, such as diffusion (both through the grain interior and along GBs), dislocation glide, dislocation climb, and GB sliding. These four mechanisms, either individually or collectively, have been studied in MPEAs and may provide insights into their creep properties and behavior. Therefore, in what follows, we present an overview of these four mechanisms in MPEAs as studied by physics-based models.

Diffusion

"Sluggish diffusion" is proposed as one of the four core effects in MPEAs [184]. However, the existence and extent of this effect in these alloys have been vigorously debated [185]. In most cases, diffusion sluggishness in MPEAs becomes apparent only after normalizing the diffusion data with respect to the alloys' melting temperatures; there is no clear evidence of sluggish diffusion when considering the absolute temperature scale [186]. A recent review by Verma et al. [46] called for more comprehensive and rigorous experimental studies to address gaps in our understanding of diffusion in MPEAs.

Diffusion through the grain interior. Diffusion in the grain interior of MPEAs has been studied using both density functional theory (DFT) and atomistic- simulation methods. Using DFT in a series of HCP MPEAs, Vaidya et al. [187] found that the diffusion rate depends not only on the number of constituents but also on their types and concentrations. However, experiments in the CoCrFeMnNi system by Dabrowa et al. [188] showed that diffusion sluggishness was independent of the number of components, suggesting that sluggish diffusion may not be a universal phenomenon across MPEAs. Zhao et al. [189] used DFT for point defect properties of NiCoCr and NiCoFeCr. Through an electronic structure analysis, Zhao et al. determined that the deformability of the d electrons varies by material and has a strong influence on vacancy-formation and vacancy-migration energies. They also propose that the e_g to t_g transition governs vacancy-migration energy in NiCoCr and NiCoFeCr MPEAs.

Using both molecular dynamics (MD) and kinetic Monte Carlo (kMC) simulations in Fe-Ni binaries, Osetsky et al. [190] found that the concentration dependence of diffusivity is non-monotonic. In CoCrFeMnNi, Mizuno et al. [191] used DFT to show that (i) vacancy-formation energies of different elements were nearly identical and (ii) vacancy-migration energy increases with atomic number, i.e., from Cr to Ni. In contrast to the first finding, DFT calculations by Middleburgh et al. [192] revealed that in CoCrFeNi, vacancy-formation energies for Co, Fe, and Ni are positive while Cr has a negative vacancy-formation energy. In contrast to the second finding, kMC simulations by Kottke et al. [193] found that in CoCrFeMnNi, Mn has the lowest vacancy-migration energy with Co having the highest. A recent study by Lafferty et al. [189] found similar results for the vacancy-migration energy, concluding that the vacancy-migration barrier is the highest for Co and the lowest for Cr in CoCrNi.

Using hybrid MC/MD simulations in CoCrNi and MoNbTa, Xing et al. [194] found that CSRO lowers diffusivity by increasing the migration barrier, a conclusion also reached by Behara and Van der Ven [195] in the Li-Mg alloy using kMC simulations. In Fe-Ni binary systems, Xu et al. [196] used kMC to show that CSRO leads to sluggish diffusion, while atomic concentrations of fast-diffusing elements and the differences in the averaged migration barriers among species are the dominant factors.

The study by Lafferty et al. also proposes that when used as a baseline, the DFT-calculated 0 K activation energy for diffusion in CoCrNi makes up 75–80% of the experimental creep activation energy in CoCrNi reported by the experimental studies of Xie et al. [77], Sadeghilaridjani [32], and Sahragard-Monfared [197].

Diffusion along GBs. Diffusion along GBs in MPEAs has been studied by MD simulations, while DFT has not been applied to this topic to the best of the author's knowledge. Using MD simulations in the CoCrFeMnNi MPEA, Junhong and Weiqiang [198] found that diffusivity within the GB is significantly higher than that in the grain interior, a trend consistent with that observed in pure metals. However, computational methods have not investigated whether GB diffusivity in MPEAs is lower than that in pure metals. In experimental studies, Vaidya et al. [199] compared CoCrFeNi and CoCrFeMnNi and found that increasing the

number of constituent elements does not necessarily reduce diffusion rates within the GB.

In summary, diffusion in MPEAs has been investigated using both DFT and atomistic-simulation methods, primarily focusing on the grain interior rather than GBs. Given the limited and often contradictory results, it remains difficult to determine from computational data alone whether MPEAs exhibit greater resistance to diffusion-dominated creep (e.g., Nabarro-Herring creep and Coble creep) than pure metals and to assess the impact of CSRO on this type of creep.

Dislocation glide

Dislocation glide is typically considered as the primary mechanism for plastic deformation of metals. Consequently, most computational studies on dislocation glide in MPEAs have focused on their short-term and/or low-temperature plastic-deformation behavior rather than creep.

DFT and atomistic simulations. Using DFT, Akdim et al. [200] found that the dislocation-core structure in NbTiZr is less compact than in pure BCC metals. Similarly, Yin et al., [201] also using DFT, found that CSRO increases the core energy of screw dislocations in MoNbTaW. In these DFT studies, a very short dislocation line (< 1 nm) was considered. The movement of long dislocation lines is typically simulated using atomistic simulations, with a focus on the critical-resolved shear stress (CRSS) for dislocation glide and mobility. The literature concludes that dislocation glides are more challenging in MPEAs than in pure metals, primarily due to the severe lattice distortion present in the former. This effect, however, varies with dislocation type. For instance, in dozens of BCC MPEAs, Wang et al. [202] showed that lattice distortion hinders the glide of edge dislocations while facilitating the movement of screw dislocations, leading to a significantly reduced edge-to-screw mobility compared to pure BCC metals. Additionally, in NbTiZr, Chen et al. [203] have found that while a small degree of CSRO might weaken the local trapping force for dislocation glide and promote dislocation mobility, a sufficiently large CSRO acts to hinder dislocation glide. Hence, based on atomistic simulation results alone, it is difficult to definitively conclude how lattice distortion and CSRO affect resistance to dislocation-glide-dominated creep (e.g., Harper-Dorn creep) in MPEAs.

Discrete-dislocation dynamics. In HfNbTa, Lu et al. [204] found that local-stress fluctuations induced by CSRO hinder dislocation slip, significantly increasing the strength of dislocation junctions in forest networks. In an MPEA not confirmed experimentally, Zhai and Zaiser [205] established the pinning length and demonstrated how it can be used as a predictor of the flow stress. In CoCrFeMnNi, Li et al. [206] revealed that heterogeneous lattice strains give rise to unusual dislocation behaviors, including multiple kinks/jogs and bidirectional cross slips, thereby contributing to the strengthening mechanisms that underpin that strength-ductility synergy. In CoCrFeNi, Chen et al. [207] identified a novel screw dislocation cross-slip mechanism driven by a collinear reaction between dislocations and rhombus-shaped perfect loops. In three FCC MPEAs, Sudmanns and El-Awady [208] demonstrated that local fluctuations in the chemical composition result in sluggish dislocation motion, frequent cross-slip, and the alignment of dislocations with solute-aggregation features.

Phase-field-based dislocation model. In CoNiRu, Su et al. [209] found that large variations in atomic configurations can cause significant changes in the intrinsic stacking fault width. In the CoCrFeMnNi MPEA family, Zeng et al. [210] showed that the material strength can be improved by introducing disorder in the chemical misfit with a characteristic length scale on the order of the average stacking-fault width. In AlCoFeMnNi, Qiu and Wu [211] showed that the CRSS of a dislocation is proven to be sensitive to the value of the intrinsic SFE. Smith et al. [212] confirmed that the Frank-Read sources in MoNbTi operate with a distinct mechanism from those in conventional alloys. In the same alloy, Fey et al. [213] showed that dislocations move in a stop-start motion, alternating between a wavy morphology in a free flight and a nearly recovered straight orientation in a full arrest. Also, in MoNbTi, Jones et al. [214] showed that between 600 and 1,200 K, the edge-dislocation glide is smooth, while screw dislocation glide exhibits three distinct glide mechanisms. Additionally, in MoNbTi, Kim et al. [215] confirmed that imposing a statistical distribution for the gradient-energy coefficients in the phase-field model is required to capture the range of non-Schmid behavior predicted by atomistic simulations. Jones et al. [216] found that in MoNbTaVW, the CRSS for dislocation glide decays slowly but continuously as the temperature increases, whereas in Nb, it decays quickly and then plateaus at a certain temperature. In two BCC MPEAs, Zheng et al. [217] found that a higher CSRO decreases the degree of the unstable SFE dispersion and, hence, the amount of hardening. In three BCC MPEAs, McNutt et al. [218] found that in the low-stress regime, the glide of the edge portions of the dislocation loop is smooth, while the glide of the screw portions of the loop is jerky; in the high-stress regime, the edge-to-screw mobility ratio is about two, while the edge mobility doubles from that in the low-stress regime.

Crystal-plasticity model. In the $Al_{0.3}$CoCrFeNi MPEA, Zhai et al. [219] linked fatigue-crack initiation to slip deformation, while Ma et al. [220] demonstrated that the B2 phase significantly enhances strength. In the CoCrFeNi MPEA, Zhang et al. [221] attributed the formation of deformed twins in the early stages of plastic deformation to the complex shear-strain distribution along GBs, whereas Lu et al. [222] observed that higher strain rates improve both tensile strength and elongation. In CoCrNi, Li et al. [223] found that plastic elongation is governed by the competition between the grain-rotation-induced deformation coordination and stress concentration, both of which are influenced by the CSRO-dependent slip resistance. Meanwhile, in $Fe_{44}Mn_{36}Co_{10}Cr_{10}$, Han et al.'s [224] validated experimental findings that dominant slip planes in adjacent grains vary based on their proximity to a notch under fatigue conditions. In HfNbTa, Lu et al. [225] identified that CSRO induces heterogeneous strains and stress partitioning, forming strong strain gradients within grains and enhancing back-stress-induced strain hardening. In $CoCrNiSi_{0.3}$, Fang et al. [226] linked the increase in the local dislocation density to the development of adiabatic shear bands and texture evolution, whereas Yu et al. [227] found that in $Al_{0.1}$CoCrFeNi, decreasing grain-size gradients and applied loads led to a more uniform dislocation density, suppressing the formation of strong domain boundaries. Gerel-Erdene and Aoyagi [228] emphasized the necessity of considering both the dislocation-density distribution and crystal orientation in the CP models to accurately capture the mechanical anisotropy of the rolled CoCrFeMnNi alloy.

Beyond single-phase MPEAs, studies on two-phase alloys highlight additional strengthening mechanisms. In $Ni_{61}Fe_{10}Cr_{10}Al_{17}Mo_2$, Zhou et al. [229] demonstrated that dynamic recrystallisation alters dislocation structures, grain sizes, and crystallographic textures. In $Fe_{61.5}(CoNi)_{28.5}Cr_{10}$, Bae et al. [230] reported that the BCC phase undergoes significant strain hardening, contributing more than three times the macroscopic stress of the FCC phase. In $Al_{0.6}$CoCrFeMnNi, Zhai et al. [231] distinguished stress-distribution differences, while fine-grained samples exhibited a uniform stress field, and coarse-grained samples showed localized stress concentration primarily in the BCC phase. Finally, in $Fe_{49.5}Mn_{30}Co_{10}Cr_{10}C_{0.5}$, Zhang et al. [232] revealed that higher stress levels and lower temperatures promote martensite nucleation and evolution, further influencing mechanical behavior.

Dislocation climb and GB sliding

While dislocation climb and GB sliding are crucial mechanisms not only in creep but also in general high-temperature deformation, they have not been simulated in MPEAs using any computational methods. Since dislocation climb is closely linked to vacancy diffusion in the grain

interior [73] and that diffusion along GBs facilitates GB sliding, prior atomic-level simulations of diffusion may provide insights into dislocation-climb-dominated creep (e.g., power-law creep) and GB-gliding-dominated creep (e.g., superplastic creep) in MPEAs.

Phenomenological models

In $Al_{0.3}CoCrFeNi$, Meng et al. [91] developed a new phenomenological model to predict micro-indentation creep tests with or without dynamic pre-compression. In their model, the creep stress exponent is described by Eq. (20),

$$n = \frac{1}{2}\cdot\frac{\left[\frac{\left(h_1/\tau_1^2\right)e^{-t/\tau_1}+\left(h_2/\tau_2^2\right)e^{-t/\tau_2}}{(h_1/\tau_1)e^{-t/\tau_1}+(h_2/\tau_2)e^{-t/\tau_2}}+\frac{(h_1/\tau_1)e^{-t/\tau_1}+(h_2/\tau_2)e^{-t/\tau_2}}{h_0+h_1\left(1-e^{-t/\tau_1}\right)+h_2\left(1-e^{-t/\tau_2}\right)}\right]}{\left[\frac{(h_1/\tau_1)e^{-t/\tau_1}+(h_2/\tau_2)e^{-t/\tau_2}}{h_0+h_1\left(1-e^{-t/\tau_1}\right)+h_2\left(1-e^{-t/\tau_2}\right)-(\varepsilon\omega/\beta)h_0^{\nu-1}}\right]} \tag{20}$$

where h_i and τ_i represent the indentation depth and the retardation time for the ith Kelvin element, respectively, as a function of the indentation loading depth for selected materials; t is the time; ϵ is a constant related to the indenter shape; ω, β, and ν are parameters that link mechanical parameters and loading depth.

In CoCrFeMnNi, Zalezak et al. [233] confirmed that the creep behavior under both tension and compression can be fitted with phenomenological power laws for the dislocation glide and climb, which were originally proposed for traditional metallic materials. These laws are described in Eq. (21) for climb-controlled creep,

$$\dot{\varepsilon}_c = A'\cdot(\gamma/\mu b)^3\cdot\mu b D_L/kT\cdot(\sigma/\mu)^5 \tag{21}$$

and for viscous glide-controlled creep in Eq. (22),

$$\dot{\varepsilon}_g = \pi(1-\nu)kTD_S/6\mu b^5\psi^2 c\cdot(\sigma/\mu)^3 \tag{22}$$

where γ is the SFE, μ the shear modulus, b the Burgers vector magnitude, D_L the coefficient of self-diffusion, k Boltzmann's constant, T the temperature, σ the applied stress, ν the Poisson's ratio, D_S is the diffusion coefficient of solute atoms, ψ the solute–solvent size difference, c the concentration of solute atoms.

Also, in CoCrFeMnNi, Zhang et al. [100] found that the experimental data for steady-state tensile creep follows another phenomenological power-law equation (Eq. (23), i.e.,

$$\dot{\varepsilon} = A\sigma^n e^{-Q_c/RT} \tag{23}$$

where A is a material constant, Q_c is the apparent activation energy of creep, R is the ideal gas constant. More research needs to be conducted to assess the suitability of other phenomenological creep models for different types of MPEAs.

Creep in MPESAs

In a recent study by Han et al. [197], the influences of stress, temperature, γ/γ' lattice misfit, and γ' volume fraction on creep in MPESAs were investigated using MD simulations. The MPESA studied was the γ/γ' formulation of $Ni_{33.4}Al_{6.7}Cr_{22.2}Fe_{9.2}Co_{28.5}$ / $Ni_{65.9}Al_{12.1}Cr_8Fe_9Co_5$. Compared to the $Ni_{33.4}Al_{6.7}Cr_{22.2}Fe_{9.2}Co_{28.5}$ MPEA, the $Ni_{33.4}Al_{6.7}Cr_{22.2}Fe_{9.2}Co_{28.5}$ / $Ni_{65.9}Al_{12.1}Cr_8Fe_9Co_5$ MPESA has lower creep strains under identical conditions, with the difference growing as a function of higher stress and temperature. The MPESA also shows superior creep resistance compared to the MPEA because the γ/γ' interfaces impede the dislocation motion and atomic transport. Finally, γ' increases creep resistance compared to the MPEA as the γ' presence reduces diffusion pathways.

Machine-learning models

In the $AlCrFeMnNiW_x$ system, Dewangan et al. [95] developed backpropagation neural networks to predict the room-temperature creep displacement based on the chemical composition, load, and time. In the FeCrNi MPEA system, Xiang et al. [234] established two machine learning (ML) models: a multi-layer perceptron (MLP) and a convolutional neural network (CNN). The input for the MLP consists of texture data, including chemical compositions, while the input for the CNN consists of SEM images. The two ML models were then integrated to predict the creep rupture time as output. In $Fe_{70}Cr_{18}Ni_{12}$, Kumar et al. [181] trained two ML models, a random forest (RF) and a CNN, to predict creep curves based on the applied stress, temperature, and time. It was found that while the CNN model performs better at higher temperatures and with larger datasets, the RF model works better at lower temperatures and with smaller datasets.

The application of ML to the creep behavior of MPEMs can benefit from prior ML studies on creep in other material systems as well as broader advances in ML for materials science. For example, Liu et al. [235] employed a divide-and-conquer self-adaptive ML method to predict the creep life of 266 Ni-based single crystal superalloys using features such as composition, test temperature, and test stress. The divide-and-conquer strategy aims to leverage materials domain knowledge to decompose complex material problems and construct ML models for each sub-problem, effectively reducing model complexity while ensuring that the learning results are both accurate and credible through the integration of domain knowledge [236]. More broadly, creep modeling shares several challenges common to many ML applications in materials science, including the contradictions between high dimensionality and small sample size, model accuracy and usability, and learning results and domain knowledge [237]. One effective way to reconcile these contradictions is to embed ML models within frameworks informed by materials domain knowledge, which emphasizes the importance of incorporating domain expertise throughout the ML modelling process, for example in feature selection methods [238].

Beyond materials science, ML-based modeling of creep also shares many fundamental challenges with data-driven applications across science and non-scientific domains. For example, regardless of the field, the quality of the underlying data strongly influences the performance of ML models. According to Liu et al. [239], effective data quantity governance should consider both the number of samples and the number of features (e.g., descriptors), as well as the balance between them. To address this critical issue, they proposed a synergistic data quantity governance flow that incorporates domain knowledge, enabling coordinated control of dataset size and feature dimensionality (or model parameter quantities). In a more recent study, Liu et al. [240] introduced a framework for governing the quality of ML-oriented materials data. This framework specifies what to evaluate through nine dimensions, indicates when governance should occur using lifecycle models, and outlines how to detect and resolve quality issues via processing models. Together, these advances establish a foundation for improving the reliability and reusability of ML-ready materials datasets, thereby facilitating materials discovery and design, and potentially supporting future studies of creep in MPEMs.

Improving the creep resistance of MPEAs

This section is focused on discussing strategies to improve creep resistance in MPEAs due to the fact that there are significantly more studies on MPEAs compared to MPESAs, MPECs, and MPEBMGs. To brush up on the strategies to improve creep resistance in MPESAs, MPECs, and MPEBMGs, elemental tuning is the most beneficial method to improve creep resistance in these systems. For MPESAs, elemental tuning is especially important to obtain a strong and coherent precipitate [16,19]. For MPECs, the available work on creep is limited to HfTaTiZrNb-ceramics and heat treatment on this system did not change

the creep mechanism significantly [13]. Meanwhile for MPEBMGs, the creep is controlled by how many STZs there are in the system and it has been revealed that heat treatments "spends" the available STZs instead of prolonging creep life in MPEBMGs [121,122].

Future improvements in the creep resistance of MPEAs will rely on focused, combined computational and experimental studies in order to narrow down the vast MPEA composition space. As mentioned in previous sections, complete computational studies focused on enhancing creep analysis are only beginning to emerge in scientific literature. The common theme amongst the published works is that it is possible to tune creep resistance by modeling microstructure evolution. Specifically, creep resistance can be improved through microstructure control. This section summarizes both the simulation efforts and reported experimental evidence on improving creep resistance. However, we do not claim that the creep resistance enhancement is universally transferable to different systems of MPEAs that are being discussed in this section.

Defect distribution

Creep resistance can be tuned via precipitates and voids in the microstructures of various MPEAs. In the phase-field study coupled with the CALculation of PHAse Diagrams (CALPHAD) method, Gao et al. [182] demonstrates that the creep strain in the CrCuFeNi MPEA increases as the Cu-rich particles grow. Cu-rich precipitates strengthen CrCuFeNi, but the spacing and growth rate of the precipitates have a direct impact on creep resistance. Gao et al. concluded the work by suggesting that microstructural engineering, such as controlling nucleation sites of precipitates, can lead to the design of alloys with increased creep resistance. Liu et al. [183] show that the irradiation dose applied to an MPEA changes the shape of microstructural voids from the spherical to cuboidal shape. This feature allows for tuning of the yield stress, as the yield stress will increase as the irradiation dose and temperature increases. Subsequently, creep resistance increases as the irradiation dose increases but decreases as the irradiation temperature increases. In ODS CoCrFeNiMn, Yan et al. [241] studied the effect of the Y_2O_3-oxide size and distribution on the creep resistance. Yan et al. improve existing creep models by considering dislocation climb and shearing mechanisms in addition to Orowan bypassing. Their unified creep model for ODS MPEAs is given by Eq. (24) [241]:

$$\dot{\varepsilon} = (2\tau_L b c_L N/M)((\sigma - \sigma_o)/(\alpha M G b))^3 \quad (24)$$

Where $\tau_L = 0.5Gb^2$ is the dislocation line tension, c_L is the strain-hardening parameter, α is a lattice-dependent Taylor constant, M is the Taylor factor, N is the dislocation mobility that depends on applied stress (σ), threshold stress (σ_o), and temperature. The primary conclusions of their work demonstrate that increasing the volume fraction of oxide particles up to 3% increases creep resistance, and that larger oxide particles increase high-temperature creep resistance.

Chemical short-range order (CSRO)

Local ordering, known as CSRO or local chemical order, within an MPEA can also increase creep resistance. As mentioned previously, Huang et al. [176] demonstrated that creep resistance can be increased with CSRO because the creep-activation energy for diffusion increases with CSRO. Additionally, CSRO can change the calculated stress exponent of the MPEA and increase creep resistance because of the presence of the CoCr cluster. Similarly, using ML interatomic potentials, Zafar et al. [242] parameterized the grain size and CSRO in a recent MD simulation study. They found that CSRO in MoNbTaW near the GBs increases the creep-activation energy for diffusion by suppressing GB sliding, especially if GB sliding is the primary creep mechanism. Finally, Zafar et al. found that promoting CSRO at the GBs is an important design choice for increasing creep resistance, promoting both ductility and creep resistance with small grain sizes.

Other creep-resistance enhancement methods

It is evident that enhancement in creep behavior at different temperatures is possible through various scientific means. At a temperature of 873 K, adding optimum amount of C and/or Al improves the creep resistance compared to equiatomic CoCrFeMnNi [98,107 34,71]. The addition of C atoms to the CoCrFeMnNi system lowered the creep rate up to 72% due to the uniform distribution of carbide precipitation in the matrix, impeding dislocation motion [107]. Al in $Al_{0.4}$CoCrFeMnNi lowered the creep rate and enhanced creep resistance by up to 60%. This trend occurred because the solid-solution strengthening and second phases functioned as an obstruction to dislocation motion [82]. Also at 873 K, Cao et al. [98] reported a grain size dependence in CoCrFeMnNi, demonstrating that a grain size of 25 μm has up to 97% lower creep strain than the strain reported by [73] with a grain size of 21.7 μm while tested at about four times higher stress. The result implies a 15% increase in the grain size significantly improves creep resistance in CoCrFeMnNi.

At 923 K, $Al_{0.4}$CoCrFeMnNi [82] remained as the material with lower minimum creep rates, at values ranging from 4×10^{-7} to 1.5×10^{-8} /s. Comparing amongst the CoCrFeMnNi system at 923 K, the creep rates reported in by Jo et al. [97] have lower minimum creep rates by up to 99% compared to Kang et al. [73], although the materials fabrication methods are similar where the samples were melted, homogenized, rolled, and subsequently annealed. The primary difference is that Kang et al. [73] used cold rolling while Jo et al. [97] employed hot rolling. Note that their grain sizes are 26 μm [97] and 21.7 μm [73], which makes CoCrFeMnNi [97] have about a 20% larger grain size, supporting the findings at 873 K that were discussed previously.

$Ni_2Co_1Fe_1V_{0.5}Mo_{0.2}$ (2×10^{-8} to 4.5×10^{-8} /s from 150 to 200 MPa) [116] and $Al_{0.3}$CoCrFeNi (1.9×10^{-9} to 10^{-8} /s from 65 to 110 MPa) [76] have grain sizes of 2,000 μm and 303 μm, respectively, and both systems showed the lowest creep rates at 973 K. $Ni_2Co_1Fe_1V_{0.5}Mo_{0.2}$ [116] deforms by viscous dislocation glide and sluggish diffusion of Mo. $Al_{0.3}$CoCrFeNi [76] creep resistance was attributed to the precipitation-strengthening effect from $L1_2$ and B2 phases forming during the creep test. At this temperature, CoCrFeMnNi, reported by Xie et. al. [78], had up to 73% lower creep rate compared to the rate reported by Jo et al. in [97]. The grain size of [78] is 140 – 150 μm, while [97] has a grain size of 26 μm, which makes [78] have over 400% larger grain size, supporting the previous findings that larger grain size leads to better creep performance.

ODS in CoCrNi lower the creep rate up to 93% at 1,023 K [112], although CoCrNi by itself had a moderate creep rate (5.5×10^{-7} to 2.4×10^{-9} /s), likely due to its low SFE [109]. CoCrNi [109] had the lowest creep rate at 1,073 K at applied stresses of 50 to 150 MPa, while ODS-CoCrFeMnNi [69] (7.2×10^{-9} to 9.8×10^{-10} /s) had the lowest minimum creep rate at 10 to 35 MPa. It is interesting to note that at 1,073 K, CoCrFeMnNi [69] has grain sizes of 0.8 μm, [101] 12 – 32 μm, and [100] 24 μm while all three have similar creep rates (10^{-6} to 10^{-8} /s) at the applied stress of 15 to 30 MPa. Incorporating ODS to improve creep properties has been exemplified by GRX-810, an ODS-strengthened CoCrNi based alloy, by coupling oxide strengthening with model-driven composition selection which sustained more than 2,800 h to 1% creep strain [243].

At temperatures of 1,123 to 1,523 K, transition-metal MPEAs, such as CoCrFeMnNi and $Al_{0.5}$CoCrFeMnNi, demonstrate adequate creep resistance, with creep rates of 4.5×10^{-3} to 1.5×10^{-6} /s, at lower applied stresses (5 – 30 MPa). In the lower temperature range (1,123 to 1,173 K) HfNbTaTiZr is comparable to transition-metal MPEAs, with creep rates from 4×10^{-8} to 5×10^{-4} /s. Comparing HfNbTaTiZr at the same temperature of 1,373 K, the study by Gadelmeier et. al. [113] with a smaller grain size of 98 μm has a creep rate up to 94% lower than the study by Liu et al. [114] with a grain size of > 1,000 μm. This trend is suggested by Gadelmeier et al. [113] that polycrystalline RMPEAs would have better creep performance with larger grain sizes or a single crystal

structure. However, it should be noted that while the HfNbTaTiZr melting temperature calculated by a thermodynamic approach is about 2,210 K [113], the temperatures from 1,253 to 1,523 K correspond to T/T_m of 0.566 to 0.689. Meanwhile, the melting temperature of CoCrFeMnNi is calculated to be 1,679 K [242], with 0.698 as the T/T_m at 1,173 K. Therefore, CoCrFeMnNi [100] performed significantly better than HfNbTaTiZr [114] at the same T/T_m, which could be because the FCC structure is more closely packed compared to the BCC structure, making diffusion slower in the FCC structure than in the BCC structure.

Heat treatments are a promising method for further improvement of creep properties of MPEAs. A majority of the MPEAs covered in this review utilized post-processing of the material, but the effects from heat treatments were not central to the reported creep resistance improvements. For some systems, improvement in creep resistance was seen from having nanosized grains versus micron grain sizes [72]. This phenomenon was only explored in a very limited set of compositions, and further exploration could yield significant results. Additionally, precipitates that form during the creep experiments increase the creep lifetime of the material. Other composition spaces could look to take advantage of that effect.

The improvement of creep properties through compositional design is also a promising strategy. Zhang et al. [244] focused on the future MPEA design using the CALPHAD technique, highlighting the vast composition space and need for more experimental data. The work demonstrates that incorporating ML models with the CALPHAD technique to improve the models is becoming a viable research alternative.

To summarize, it is experimentally evident that strong improvements in the creep behavior of MPEAs are achieved. Addition of alloying elements, such as C and Al, and incorporation of oxides by means of atom inclusion, such as Y and O, improved the creep resistance in CoCrNi-based and CoCrFeMnNi-based MPEAs. Improvement of creep behavior due to larger grain sizes were observed in HfNbTaTiZr and CoCrFeMnNi at certain temperatures. Having lower SFE within a similar alloy system in FCC systems is also shown in certain experiments to improve creep resistance.

Summary

The creep behavior of MPEAs, MPESAs, MPECs, and MPEBMGs systems tested using uniaxial and indentation creep tests were reviewed. Generally, MPEAs have not exceeded the creep resistance of superalloys, however a recent development on compositionally engineered MPESAs may be comparable to traditional superalloys in terms of the creep resistance. Although MPEBMGs exhibit very high hardness and strength, their creep resistance has not yet matched traditional superalloys under compressive creep. Meanwhile, MPECs have substantially better creep performance than their traditional counterparts.

MPEAs, which are dominated by the FCC CoCrFeMnNi family, are primarily deformed by dislocation interactions. Improved creep resistance at different temperatures was demonstrated with the addition of alloying elements, such as C and Al, addition of oxides, incorporation of second phases, such as $L1_2$ and B2, having low SFE, and having either very small grain size to obtain a stable GB in some systems or larger grain sizes in others. Many reported creep data are populated with equiatomic compositions such as CoCrFeMnNi and its derivatives, the mechanistic design principles that have been discussed in the present work cannot be claimed to work on other non-equiatomic systems. However, the strategies that have worked in enhancing creep resistance are what the literature shows. Therefore, validation in the broader non-equiatomic space is still needed. In MPESAs, the composition, precipitate size, precipitate distribution, and misfit between the matrix and precipitate might play key roles in the creep behavior. For MPECs, creep behavior was studied using compressive loads due to their brittleness. Heat treatments influence the stress exponent and activation energy of MPECs although the creep rates remain similar. The diffusion of smaller atoms might be the key mechanism of creep in MPECs. The creep behavior of MPEBMGs is controlled by the STZ size and activation, and is affected by the composition, loading rate, holding time, and structural state. Over the reviewed testing methods, a smaller STZ volume correlates with a lower activation energy consistently, revealing a unified creep mechanism despite differences in testing methods.

In terms of different creep testing methods, it was observed that the creep properties of the same material in tension and in compression are comparable across different reported work. Meanwhile, indentation and nanoindentation creep tests report vastly different creep exponents for the same material, due to different maximum load, holding time, and possibly the location of indentation in the material. Moreover, the creep behavior in nanoindentation and indentation cannot be directly compared to the creep in uniaxial load due to most studies being done at room and lower temperatures.

Finally, computational work on creep studies in MPEMs is much more limited compared to the experimental studies that have been performed. Computational creep studies are primarily limited to CoCrNi, FeCrNi, and CrCuFeNi MPEAs, and were performed through atomistic simulation, phase-field modeling, and the CP method. The primary findings from these studies are (i) in CoCrNi, CSRO reduces creep deformation by slowing atomic diffusion and dislocation glide and (ii) creep resistance can be increased by adding particles or voids to the MPEA. One MD study was performed on MPESAs, showing that adding the γ' phase to an MPEA increases the creep resistance due to effects from the γ/γ' interface, volume fraction of the precipitate, and lattice mismatch.

Future directions

Despite the growing body of work in creep behavior of MPEMs, several knowledge gaps still limit cross-study comparability and mechanistic generalization of creep behavior in MPEMs. Though the study of creep in MPEMs has grown in recent years in terms of the number of publications (Fig. 1), existing studies are limited to the CoCrFeMnNi system and its subsets. For RMPEAs, current studies are limited to the HfNbTaTiZr system. Many studies report an incomplete mechanistic evidence set which include creep exponent, activation energy, and microstructure evolution together, making mechanism assignments and cross-comparisons uncertain. Nanoindentation creep data is currently poorly comparable with uniaxial creep data due to localized responses, drifts, or compliance sensitivity, and other nanoindentation tests limitations. Although many of the reported studies conducted room-temperature nanoindentation tests to investigate creep behavior of MPEMs, the creep behavior in nanoindentation tests is still ambiguous. Because it is evident that the incorporation of well-dispersed oxides and second phases could improve creep behavior, it is crucial to develop new compositions with dense and uniformly distributed particles or precipitates to improve high-temperature creep resistance at elevated temperatures. Service-relevant creep modes in MPEMs such as creep-fatigue, long term creep behavior, irradiation-assisted creep, and creep in corrosive or oxidizing environments are still sparse despite their application relevance. Therefore, necessary improvements must be made to allow MPEMs to compete with commercial materials.

Future creep experiments should focus on dynamic microstructural control throughout the creep-deformation process. Ideally, tension and compression methods should be utilized to extract the most reliable data in a way that is similar to the environments where creep resistance is desired. In that regard, the vast majority of the experiments reviewed in this paper were performed in an open-air environment. Future experiments could involve tension or compression creep tests in inert gas or vacuum environments. Environment-controlled studies would allow for more consistent experimental results when oxidation is a factor. These environments would also give further insight into compositional responses and provide fundamental investigations of creep behavior.

On the other hand, the opposite approach should also be taken for creep experiments to be performed in complex extreme environments.

These environments could be chosen based on real-life applications where creep is a common failure mechanism. Such extremes could include creep-fatigue experiments, mimicking applications such as turbine engines, creep in irradiative environments mirroring those in nuclear-power plants, and corrosive environments such as pipes with high-temperature corrosive gases. Improvements in these areas would directly impact the lifetime of materials used in these regimes and lead to overall reduced costs. So far, creep-fatigue experiments have not been conducted on MPEAs. Beyond that, to deepen and expand the fundamental understanding of fracture mechanics of MPEAs, experiments such as creep-fatigue on smooth bar and creep-crack propagation could be conducted on MPEAs.

Furthermore, future studies could also be directed to expanding the high-entropy concept. Recently, the creep behavior of MPESAs was studied, showing promising creep resistance [19,140,142,245]. These alloys might improve upon the current superalloys, allowing for a quicker transition to commercial availability for MPEMs. Furthermore, expanding MPEC experiments beyond those already reviewed would allow for a greater effort of finding suitable high-temperature coatings that show promising creep resistance [13,15]. Additionally, MPEBMGs can continue to be explored for their creep properties that may be beneficial in niche applications. Due to the exceptionally large compositional space of MPEMs, ML [245–247] could be a method to determine compositions and post-processing steps to create a greatly improved material especially with phenomenologically based models aiding predictions. The need to explore more MPEMs for their creep properties is evidenced by a concurrently published review paper on creep behavior of MPEM [248]. Conclusions drawn by Zhang et al. [248] mirror the conclusions of this manuscript that MPEMs are not currently in a state to compete with commercial Ni-based superalloys, but continued exploration and research could lead to commercialization of MPEMs. Combined with advanced manufacturing techniques, MPEMs could reach a point of commercial viability [140]. Each of these areas shows the immediate importance of creating new materials with improved creep properties, and the many paths available to achieve those improvements.

CRediT authorship contribution statement

Lia Amalia: Writing – original draft, Visualization, Data curation. **Nathan Grain:** Writing – original draft, Visualization, Data curation. **Yanqing Su:** Writing – original draft, Validation. **Chelsey Z. Hargather:** Writing – review & editing, Writing – original draft, Validation. **Shuozhi Xu:** Writing – review & editing, Project administration, Funding acquisition, Conceptualization. **Peter K. Liaw:** .

Declaration of competing interest

The authors declare that they have no known competing financial interests or personal relationships that could have appeared to influence the work reported in this paper.

Acknowledgements

LA, NG, and PKL are grateful for the support from the US National Science Foundation (DMR 2226508), the Center for Materials Processing and the GATE Fellowship from The University of Tennessee, and the Air Force Office of Scientific Research (AF AFOSR-FA9550-23-1-0503). CH acknowledges support for this work by the U.S. Department of Energy through the Los Alamos National Laboratory. Los Alamos National Laboratory is operated by Triad National Security, LLC, for the National Nuclear Security Administration of U.S. Department of Energy (Contract No. 89233218CNA000001). This manuscript has been approved for unlimited release with release number LA-UR-25-32288. SX acknowledges the support of the U.S. National Science Foundation (DMREF-2522655). We are grateful to Dr. Wei-Ren Chen for his comments on the paper.

Data availability

Data will be made available on request.

References

[1] J.W. Yeh, et al., *Nanostructured high-entropy alloys with multiple principal elements: novel alloy design concepts and outcomes*, Adv. Eng. Mater. 6 (5) (2004) 299–303.
[2] B. Cantor, et al., *Microstructural development in equiatomic multicomponent alloys*, Mater. Sci. Eng. A 375–377 (2004) 213–218.
[3] P.S. Phani, W.C. Oliver, *A direct comparison of high temperature nanoindentation creep and uniaxial creep measurements for commercial purity aluminum*, Acta Mater. 111 (2016) 31–38.
[4] Z. Li, et al., *Interstitial atoms enable joint twinning and transformation induced plasticity in strong and ductile high-entropy alloys*, Sci. Rep. 7 (1) (2017) 40704.
[5] Y.L. Zhao, et al., *Heterogeneous precipitation behavior and stacking-fault-mediated deformation in a CoCrNi-based medium-entropy alloy*, Acta Mater. 138 (2017) 72–82.
[6] X. Dingfeng, et al., *A critical review of the mechanical properties of CoCrNi-based medium-entropy alloys*, Microstructures 2 (1) (2022) 2022001.
[7] O.N. Senkov, et al., *Refractory high-entropy alloys*, Intermetallics 18 (9) (2010) 1758–1765.
[8] O.N. Senkov, et al., *Development and exploration of refractory high entropy alloys—A review*, J. Mater. Res. 33 (19) (2018) 3092–3128.
[9] Q. Fan, et al., *Nanoindentation creep behavior of diverse microstructures in a pre-strained interstitial high-entropy alloy by high-throughput mapping*, Mater. Sci. Eng. A 856 (2022) 143988.
[10] W. Kim, et al., *The effect of Al to high-temperature deformation mechanisms and processing maps of Al0. 5CoCrFeMnNi high entropy alloy*, J. Alloy. Compd. 802 (2019) 152–165.
[11] Y. Ma, et al., *Nanoindentation study on the creep characteristics of high-entropy alloy films: Fcc versus bcc structures*, Int. J. Refract. Met. Hard Mater 54 (2016) 395–400.
[12] Ł. Rogal, D. Kalita, L. Litynska-Dobrzynska, *CoCrFeMnNi high entropy alloy matrix nanocomposite with addition of Al2O3*, Intermetallics 86 (2017) 104–109.
[13] Guo, H., W. Zou, D. Moskovskikh, S. Yudin, Z. Cheng, S. Volodko, and C. Zhang, *High creep resistance of (Hf0. 2Ta0. 2Ti0. 2Nb0. 2Zr0. 2) C high entropy ceramics prepared by spark plasma sintering of the self-propagating high temperature synthesized powders.* Ceramics International, 2025. **51**(4): p. 5148-5158.
[14] X. Han, et al., *Improved creep resistance of high entropy transition metal carbides*, J. Eur. Ceram. Soc. 40 (7) (2020) 2709–2715.
[15] Z. Cheng, et al., *Compressive creep properties and mechanisms of (Ti-Zr-Nb-Ta-Mo) C high entropy ceramics at high temperatures*, J. Eur. Ceram. Soc. 42 (13) (2022) 5280–5289.
[16] J. Hunfeld, et al., *Design of a new wrought CrCoNi-based medium-entropy superalloy C-264 for high-temperature applications*, Mater. Des. 211 (2021) 110174.
[17] C. Liu, et al., *A novel low-density and high-strength Fe-Ni-base high-entropy superalloy with stable γ/γ'coherent microstructure at 1023 K*, Scr. Mater. 252 (2024) 116236.
[18] Tsao, T., A. Yeh, J. Yeh, M. Chiou, C. Kuo, H. Murakami, and K. Kakehi. *High temperature properties of advanced directionally–solidified high entropy superalloys, Superalloys 2016 13th Int.* 2016. Symp.
[19] T. Saito, et al., *Tensile creep behavior of single-crystal high-entropy superalloy at intermediate temperature*, Crystals 11 (1) (2020) 28.
[20] M.M. Trexler, N.N. Thadhani, *Mechanical properties of bulk metallic glasses*, Prog. Mater Sci. 55 (8) (2010) 759–839.
[21] A. Lund, C. Schuh, *The Mohr–Coulomb criterion from unit shear processes in metallic glass*, Intermetallics 12 (10–11) (2004) 1159–1165.
[22] D. Han, et al., *Atomistic structural mechanism for the glass transition: Entropic contribution*, Phys. Rev. B 101 (1) (2020) 014113.
[23] P. Gong, K.F. Yao, H.Y. Ding, *Crystallization kinetics of TiZrHfCuNiBe high entropy bulk metallic glass*, Mater. Lett. 156 (2015) 146–149.
[24] Q. Fang, et al., *Deformation behaviors of Cu29Zr32Ti15Al5Ni19 high entropy bulk metallic glass during nanoindentation*, Appl. Surf. Sci. 443 (2018) 122–130.
[25] E.P. George, W.A. Curtin, C.C. Tasan, *High entropy alloys: a focused review of mechanical properties and deformation mechanisms*, Acta Mater. 188 (2020) 435–474.
[26] M. Pekguleryuz, M. Celikin, *Creep resistance in magnesium alloys*, Int. Mater. Rev. 55 (4) (2010) 197–217.
[27] C. Zhu, T. Lu, *Deformation mechanism of a high-entropy alloy CoCrFeMnNi at intermediate high temperatures investigated by stress relaxation*, Mater. Res. Express 6 (3) (2018) 036531.
[28] F. Dobeš, et al., *Different Types of Particle Effects in Creep Tests of CoCrFeNiMn High-Entropy Alloy*, Materials 15 (20) (2022) 7363.
[29] S. Ma, *Creep resistance and strain-rate sensitivity of a CoCrFeNiAl0. 3 high-entropy alloy by nanoindentation*, Mater. Res. Express 6 (12) (2019) 126508.
[30] J. Gao, et al., *Enhancing creep resistance of aged Fe–Cr–Ni medium-entropy alloy via nano-sized Cu-rich and NbC precipitates investigated by nanoindentation*, J. Mater. Res. Technol. 20 (2022) 1860–1872.

[31] H. Jeong, H. Park, W. Kim, *Class I type creep behavior of coarse-grained Al0. 5CoCrFeMnNi high entropy alloy*, Mater. Sci. Eng. A 845 (2022) 143239.
[32] M. Sadeghilaridjani, S. Mukherjee, *High-temperature nano-indentation creep behavior of multi-principal element alloys under static and dynamic loads*, Metals 10 (2) (2020) 250.
[33] M. Sadeghilaridjani, et al., *High-temperature nano-indentation creep of reduced activity high entropy alloys based on 4-5-6 elemental palette*, Entropy 22 (2) (2020) 230.
[34] Y. Ma, et al., *Nanoindentation creep behavior in a CoCrFeCuNi high-entropy alloy film with two different structure states*, Mater. Sci. Eng. A 621 (2015) 111–117.
[35] W.-R. Wang, W.-L. Wang, J.-W. Yeh, *Phases, microstructure and mechanical properties of AlxCoCrFeNi high-entropy alloys at elevated temperatures*, J. Alloy. Compd. 589 (2014) 143–152.
[36] Z. Xu, et al., *Microstructure and nanoindentation creep behavior of CoCrFeMnNi high-entropy alloy fabricated by selective laser melting*, Addit. Manuf. 28 (2019) 766–771.
[37] L. Zhang, et al., *Nanoindentation creep behavior of an Al 0.3 CoCrFeNi high-entropy alloy*, Metall. Mater. Trans. A 47 (2016) 5871–5875.
[38] P. Zhou, et al., *Nanoindentation creep behavior of CoCrFeNiMn high-entropy alloy under different high-pressure torsion deformations*, J. Mater. Eng. Perform. 28 (2019) 2620–2629.
[39] G.E. Ruiz-Jasso, et al., *Synthesis of CuCrFeNiTiAlx high entropy alloys by means of mechanical alloying and spark plasma sintering*, Can. Metall. Q. 60 (2) (2021) 66–74.
[40] Y. Deng, et al., *Insight into the enhancing mechanical strength of CoCrNi-TiC composites fabricated by laser powder bed fusion*, Mater. Sci. Eng. A 924 (2025) 147786.
[41] A. Anand, S.-J. Liu, C.V. Singh, *Recent advances in computational design of structural multi-principal element alloys*, iScience 26 (10) (2023) 107751.
[42] W. Li, et al., *Mechanical behavior of high-entropy alloys*, Prog. Mater Sci. 118 (2021) 100777.
[43] D.E.P. Klenam, et al., *Corrosion resistant materials in high-pressure high-temperature oil wells: an overview and potential application of complex concentrated alloys*, Eng. Fail. Anal. 157 (2024) 107920.
[44] A. Ayyagari, et al., *Corrosion, erosion and wear behavior of complex concentrated alloys: a review*, Metals 8 (8) (2018) 603.
[45] S.K. Dewangan, et al., *A review on High-Temperature Applicability: a milestone for high entropy alloys*, Engineering Science and Technology, an International Journal 35 (2022) 101211.
[46] V. Verma, et al., *Diffusion in High Entropy Alloy Systems – a Review*, Prog. Mater Sci. 142 (2024) 101245.
[47] R.K. Mishra, *Short review on high entropy alloys for high temperature structural applications*, Adv. Mater. Process. Technol. 10 (2) (2024) 221–230.
[48] Y. Han, H. Fu, *Improvement of high temperature wear resistance of laser-cladding high-entropy alloy coatings: a review*, Metals 14 (9) (2024) 1065.
[49] M. Dada, P. Popoola, N. Mathe, *Recent advances of high entropy alloys for aerospace applications: a review*, World Journal of Engineering 20 (1) (2023) 43–74.
[50] P. Kumari, et al., *A Comprehensive Review: recent Progress on magnetic High Entropy Alloys and Oxides*, J. Magn. Magn. Mater. 554 (2022) 169142.
[51] S. Kumar, *Comprehensive review on high entropy alloy-based coating*, Surf. Coat. Technol. 477 (2024) 130327.
[52] W. Li, et al., *Creep, fatigue, and fracture behavior of high-entropy alloys*, J. Mater. Res. 33 (19) (2018) 3011–3034.
[53] M.E. Kassner, M.T. Pérez-Prado, *Five-power-law creep in single phase metals and alloys*, Prog. Mater Sci. 45 (1) (2000) 1–102.
[54] Dieter, G.E. and D. Bacon, *Mechanical Metallurgy*. Vol. 3. 1976: McGraw-hill New York.
[55] J. Bressers, *Creep and fatigue in high temperature alloys*, (no Title) (1981).
[56] Murty, K.L., *Materials Ageing and Degradation in Light Water Reactors: Mechanisms and Management*. 2013: Elsevier.
[57] A.C. Lund, C.A. Schuh, *The Mohr–Coulomb criterion from unit shear processes in metallic glass*, Intermetallics 12 (10) (2004) 1159–1165.
[58] A. Argon, *Plastic deformation in metallic glasses*, Acta Metall. 27 (1) (1979) 47–58.
[59] M. Jiang, et al., *Energy dissipation in fracture of bulk metallic glasses via inherent competition between local softening and quasi-cleavage*, Phil. Mag. 88 (3) (2008) 407–426.
[60] J. Lewandowski, A. Greer, *Temperature rise at shear bands in metallic glasses*, Nat. Mater. 5 (1) (2006) 15–18.
[61] G. Wang, et al., *Tensile creep characterization and prediction of zr-based metallic glass at high temperatures*, Metals 8 (6) (2018) 457.
[62] Ohta, M., A. Berlev, V. Khonik, and K. Kitagawa, *Isothermal creep of bulk glassy Zr52. 5Ti5Cu17. 9Ni14. 6Al10 below T g*. Philosophical Magazine, 2003. **83**(30): p. 3463-3471.
[63] L. Zhang, et al., *Dynamic mechanical relaxation and thermal creep of high-entropy La30Ce30Ni10Al20Co10 bulk metallic glass*, Science China Physics, Mechanics & Astronomy 64 (9) (2021) 296111.
[64] Kassner, M.E., *Fundamentals of creep in metals and alloys*. 2015: Butterworth-Heinemann.
[65] F. Nabarro, *Report of a Conference on the Strength of Solids*, The Physical Society, London, 1948, p. 75.
[66] C. Herring, *Diffusional viscosity of a polycrystalline solid*, J. Appl. Phys. 21 (5) (1950) 437–445.
[67] R. Coble, *A model for boundary diffusion controlled creep in polycrystalline materials*, J. Appl. Phys. 34 (6) (1963) 1679–1682.
[68] F. Dobeš, et al., *Compressive creep behavior of an oxide-dispersion-strengthened CoCrFeMnNi high-entropy alloy*, Mater. Sci. Eng. A 732 (2018) 99–104.
[69] H. Hadraba, et al., *Oxide dispersion strengthened CoCrFeNiMn high-entropy alloy*, Mater. Sci. Eng. A 689 (2017) 252–256.
[70] Reed-Hill, R.E., R. Abbaschian, and R. Abbaschian, *Physical metallurgy principles*. Vol. 17. 1973: Van Nostrand New York.
[71] C. Wang, M. Zhang, T. Nieh, *Nanoindentation creep of nanocrystalline nickel at elevated temperatures*, J. Phys. D Appl. Phys. 42 (11) (2009) 115405.
[72] B. Zhang, et al., *Inhibiting creep in nanograined alloys with stable grain boundary networks*, Science 378 (6620) (2022) 659–663.
[73] Y.B. Kang, et al., *Dislocation creep behavior of CoCrFeMnNi high entropy alloy at intermediate temperatures*, Materials Research Letters 6 (12) (2018) 689–695.
[74] P.K. Chaudhury, F.A. Mohamed, *Creep and ductility in an Al-Cu solid-solution alloy*, Metall. Trans. A 18 (12) (1987) 2105–2114.
[75] Y. Li, et al., *Microstructural evolution mediated creep deformation mechanism for the AlCoCrFeNi2. 1 eutectic high-entropy alloy under different testing conditions*, Mater. Sci. Eng. A 857 (2022) 144100.
[76] S. Chen, et al., *Extraordinary creep resistance in a non-equiatomic high-entropy alloy from the optimum solid-solution strengthening and stress-assisted precipitation process*, Acta Mater. 244 (2023) 118600.
[77] D. Xie, et al., *Tensile creep behavior of an equiatomic CoCrNi medium entropy alloy*, Intermetallics 121 (2020) 106775.
[78] D. Xie, et al., *Long-term tensile creep behavior of a family of FCC-structured multi-component equiatomic solid solution alloys*, Scr. Mater. 212 (2022) 114556.
[79] K.L. Murty, F. Mohamed, J. Dorn, *Viscous glide, dislocation climb and newtonian viscous deformation mechanisms of high temperature creep in Al-3Mg*, Acta Metall. 20 (8) (1972) 1009–1018.
[80] S. Hong, *Influence of dynamic strain aging on the transition of creep characteristics of a solid solution alloy at various temperatures*, Mater. Sci. Eng. A 110 (1989) 125–130.
[81] S.I. Hong, *Criteria for predicting twin-induced plasticity in solid solution copper alloys*, Mater. Sci. Eng. A 711 (2018) 492–497.
[82] C. Cao, et al., *Creep behaviour and microstructural evolution of AlxCrMnFeCoNi high-entropy alloys*, Mater. Sci. Technol. (2019).
[83] M.E. Kassner, *New developments in understanding harper–dorn, five-power law creep and power-law breakdown*, Metals 10 (10) (2020) 1284.
[84] M. Kassner, R. Ermagan, *Power law breakdown in the creep in single-phase metals*, Metals 9 (12) (2019) 1345.
[85] F. Garofalo, *An empirical relation defining the stress dependence to minimum creep rate in metals*, Trans. Metall. Soc. AIME 227 (1963) 351.
[86] M.E. Kassner, P. Geantil, L.E. Levine, *Long range internal stresses in single-phase crystalline materials*, Int. J. Plast 45 (2013) 44–60.
[87] M.E. Kassner, *The rate dependence and microstructure of high-purity silver deformed to large strains between 0.16 and 0.30Tm*, Metall. Trans. A 20 (10) (1989) 2001–2010.
[88] H. Luthy, A.K. Miller, O.D. Sherby, *The stress and temperature dependence of steady-state flow at intermediate temperatures for pure polycrystalline aluminum*, Acta Metall. 28 (2) (1980) 169–178.
[89] T. Cao, et al., *The influence of Al elements on the structure and the creep behavior of AlxCoCrFeNi high entropy alloys*, Mater. Lett. 164 (2016) 344–347.
[90] Z.-M. Jiao, et al., *Plastic deformation of Al 0.3 CoCrFeNi and AlCoCrFeNi high-entropy alloys under nanoindentation*, J. Mater. Eng. Perform. 24 (2015) 3077–3083.
[91] L. Meng, et al., *Theoretical characterization of indentation depth-dependent creep behavior of CoCrFeNiAl0. 3 High-entropy alloy*, Acta Mech. Solida Sin. 36 (1) (2023) 55–64.
[92] S. Chen, et al., *Nanoscale serration and creep characteristics of Al0. 5CoCrCuFeNi high-entropy alloys*, J. Alloy. Compd. 752 (2018) 464–475.
[93] H. Jeong, et al., *Operation of solute-drag creep in an AlCoCrFeMnNi high-entropy alloy and enhanced hot workability*, J. Alloy. Compd. 824 (2020) 153829.
[94] Z. Jiao, et al., *Strain rate sensitivity of nanoindentation creep in an AlCoCrFeNi high-entropy alloy*, Appl. Phys. A 122 (2016) 1–5.
[95] S.K. Dewangan, et al., *Prediction of nanoindentation creep behavior of tungsten-containing high entropy alloys using artificial neural network trained with Levenberg–Marquardt algorithm*, J. Alloy. Compd. 958 (2023) 170359.
[96] Kral, P., W. Blum, J. Dvorak, N. Yurchenko, N. Stepanov, S. Zherebtsov, L. Kuncicka, M. Kvapilova, and V. Sklenicka, *Creep behavior of an AlTiVNbZr0. 25 high entropy alloy at 1073 K*. Materials Science and Engineering: A, 2020. **783**: p. 139291.
[97] M.-G. Jo, et al., *High temperature tensile and creep properties of CrMnFeCoNi and CrFeCoNi high-entropy alloys*, Mater. Sci. Eng. A 838 (2022) 142748.
[98] C. Cao, et al., *Intermediate-temperature creep deformation and microstructural evolution of an equiatomic FCC-structured CoCrFeNiMn high-entropy alloy*, Entropy 20 (12) (2018) 960.
[99] K.A. Rozman, et al., *Long-term creep behavior of a CoCrFeNiMn high-entropy alloy*, J. Mater. Eng. Perform. 29 (2020) 5822–5839.
[100] M. Zhang, E.P. George, J. Gibeling, *Tensile creep properties of a CrMnFeCoNi high-entropy alloy*, Scr. Mater. 194 (2021) 113633.
[101] J. He, et al., *Steady state flow of the FeCoNiCrMn high entropy alloy at elevated temperatures*, Intermetallics 55 (2014) 9–14.
[102] Y.-K. Kim, S. Yang, K.-A. Lee, *Compressive creep behavior of selective laser melted CoCrFeMnNi high-entropy alloy strengthened by in-situ formation of nano-oxides*, Addit. Manuf. 36 (2020) 101543.
[103] S. Sun, et al., *Nanostructuring as a route to achieve ultra-strong high-and medium-entropy alloys with high creep resistance*, J. Alloy. Compd. 830 (2020) 154656.
[104] D.-H. Lee, et al., *Spherical nanoindentation creep behavior of nanocrystalline and coarse-grained CoCrFeMnNi high-entropy alloys*, Acta Mater. 109 (2016) 314–322.

[105] M. Zhang, E.P. George, J. Gibeling, *Elevated-temperature deformation mechanisms in a CrMnFeCoNi high-entropy alloy*, Acta Mater. 218 (2021) 117181.
[106] S. Reddy, et al., *Superplastic-like flow in a fine-grained equiatomic CoCrFeMnNi high-entropy alloy*, Materials Research Letters 5 (6) (2017) 408–414.
[107] Y.K. Kim, K.R. Lim, K.A. Lee, *Superior resistance to high–temperature creep in an additively manufactured precipitation–hardened CrMnFeCoNi high–entropy alloy nanocomposite*, Mater. Des. 227 (2023) 111761.
[108] M. Tsai, et al., Creep of face-centered-cubic 111 and 100 grains in FeCoNiCrMn and FeCoNiCrMnAl alloys: Orientation and solid solution effects, Intermetallics 103 (2018) 88–96.
[109] K. Rozman, et al., *Long-Term Creep Behavior of a CoCrFeNi Medium-Entropy Alloy*, J. Mater. Eng. Perform. 31 (11) (2022) 9220–9235.
[110] Z. Wang, et al., *Nanoindentation characterized initial creep behavior of a high-entropy-based alloy CoFeNi*, Intermetallics 53 (2014) 183–186.
[111] S. Sun, et al., *Effects of cold-rolling and subsequent annealing on the nano-mechanical and creep behaviors of CrCoNi medium-entropy alloy*, Mater. Sci. Eng. A 839 (2022) 142802.
[112] G. Sahragard-Monfared, et al., *Superior tensile creep behavior of a novel oxide dispersion strengthened CrCoNi multi-principal element alloy*, Acta Mater. 255 (2023) 119032.
[113] C. Gadelmeier, et al., *Creep strength of refractory high-entropy alloy TiZrHfNbTa and comparison with Ni-base superalloy CMSX-4*, Cell Rep. Phys. Sci. 3 (8) (2022).
[114] C.-J. Liu, et al., *Tensile creep behavior of HfNbTaTiZr refractory high entropy alloy at elevated temperatures*, Acta Mater. 237 (2022) 118188.
[115] A. Karantzalis, et al., *A first approach on the assessment of the creep behavior of MoTaNbV x Ti high entropy alloys by indentation testing*, SN Appl. Sci. 2 (2020) 1–10.
[116] Jiang, W., Y. Cao, S. Yuan, Y. Zhang, and Y. Zhao, *Creep properties and deformation mechanisms of a Ni2Co1Fe1V0. 5Mo0. 2 medium-entropy alloy*. Acta Materialia, 2023. **245**: p. 118590.
[117] D. Wang, et al., *Enhanced creep resistance of Ti30Al25Zr25Nb20 high-entropy alloy at room temperature*, J. Alloy. Compd. 885 (2021) 161038.
[118] X. Zhang, et al., *Nano-scaled creep response of TiAlV low density medium entropy alloy at elevated temperatures*, Materials 13 (1) (2019) 36.
[119] X. Shen, et al., *Intermediate-temperature creep behaviors of an equiatomic VNbMoTaW refractory high-entropy alloy*, J. Mater. Res. Technol. 24 (2023) 4796–4807.
[120] P. Gong, et al., *Alloying effect on the room temperature creep characteristics of a Ti-Zr-Be bulk metallic glass*, Phys. B Condens. Matter 530 (2018) 7–14.
[121] Y. Duan, et al., *Anelastic relaxation considering physical aging effects in a high-entropy metallic glass*, Sci. China Technol. Sci. 67 (12) (2024) 3967–3975.
[122] L. Zhang, et al., *Effect of physical aging and cyclic loading on power-law creep of high-entropy metallic glass*, Journal of Materials Science & Technology 115 (2022) 1–9.
[123] Tong, Y., J. Qiao, C. Zhang, J.-M. Pelletier, and Y. Yao, *Mechanical properties of Ti16. 7Zr16. 7Hf16. 7Cu16. 7Ni16. 7Be16. 7 high-entropy bulk metallic glass*. Journal of Non-Crystalline Solids, 2016. **452**: p. 57-61.
[124] Wang, X., P. Gong, L. Deng, J. Jin, S. Wang, and P. Zhou, *Nanoindentation study on the room temperature creep characteristics of a senary Ti16. 7Zr16. 7Hf16. 7Cu16. 7Ni16. 7Be16. 7 high entropy bulk metallic glass*. Journal of Non-Crystalline Solids, 2017. **470**: p. 27-37.
[125] Q. Luo, et al., *Tuning nanoscale heterogeneity by non-affine thermal strain to modulate defect activation and maximize magnetocaloric effect of metallic glass*, Mater. Des. 225 (2023) 111500.
[126] P. Gong, et al., *Room temperature nanoindentation creep behavior of TiZrHfBeCu (Ni) high entropy bulk metallic glasses*, Mater. Sci. Eng. A 688 (2017) 174–179.
[127] J. Pi, et al., *Nanoindentation mechanical properties of glassy Cu29Zr32Ti15Al5Ni19*, J. Alloy. Compd. 657 (2016) 726–732.
[128] Y. Tong, et al., *Rate-dependent plastic deformation of TiZrHfCuNiBe high entropy bulk metallic glass*, J. Alloy. Compd. 785 (2019) 542–552.
[129] J. Wu, et al., *Structure related potential-upsurge during tensile creep of high entropy Al20Ce20La20Ni20Y20 metallic glass*, J. Alloy. Compd. 827 (2020) 154298.
[130] W. Sun, et al., *Thermal annealing affected microstructure evolution and creep behavior in amorphous TaTiZr medium-entropy alloy*, Journal of Materials Science & Technology 225 (2025) 174–187.
[131] F. Li, et al., *A detailed appraisal of the stress exponent used for characterizing creep behavior in metallic glasses*, Mater. Sci. Eng. A 654 (2016) 53–59.
[132] X. Zhao, et al., *Dependence of room-temperature nanoindentation creep behavior and shear transformation zone on the glass transition temperature in bulk metallic glasses*, J. Non Cryst. Solids 445 (2016) 19–29.
[133] C. Li, et al., *Effect of peak loads and cooling rates on creep behavior of Zr-based bulk metallic glass*, J. Non Cryst. Solids 522 (2019) 119596.
[134] K. Tao, V. Khonik, J. Qiao, *Indentation creep dynamics in metallic glasses under different structural states*, Int. J. Mech. Sci. 240 (2023) 107941.
[135] C. Yuan, et al., *Pronounced nanoindentation creep deformation in Cu-doped CoFe-based metallic glasses*, J. Alloy. Compd. 806 (2019) 246–253.
[136] C. Wang, et al., *Time-dependent shear transformation zone in thin film metallic glasses revealed by nanoindentation creep*, J. Alloy. Compd. 696 (2017) 239–245.
[137] K. Tao, et al., *Unraveling the microstructural heterogeneity and plasticity of Zr50Cu40Al10 bulk metallic glass by nanoindentation*, Int. J. Plast 154 (2022) 103305.
[138] M. Yang, et al., *Unusual relation between glass-forming ability and thermal stability of high-entropy bulk metallic glasses*, Materials Research Letters 6 (9) (2018) 495–500.
[139] S.-I. Baik, et al., *Increasing the creep resistance of Fe-Ni-Al-Cr superalloys via Ti additions by optimizing the B2/L21 ratio in composite nano-precipitates*, Acta Mater. 157 (2018) 142–154.
[140] H.J. Im, D.C. Dunand, *Microstructure, hardness, and creep of Co-Fe-Ni-based high-entropy superalloy processed by laser powder-bed fusion*, Mater. Sci. Eng. A 916 (2024) 147378.
[141] U. Glatzel, et al., *Quantification of solid solution strengthening and internal stresses through creep testing of Ni-containing single crystals at 980° C*, Metals 11 (7) (2021) 1130.
[142] T.-K. Tsao, et al., *The high temperature tensile and creep behaviors of high entropy superalloy*, Sci. Rep. 7 (1) (2017) 12658.
[143] E.A. Estrada Rodas, S. Gorgannejad, R.W. Neu, *Creep-fatigue behaviour of single-crystal Ni-base superalloy CMSX-8*, Fatigue & Fracture of Engineering Materials & Structures 42 (9) (2019) 2155–2171.
[144] M. Barboza, et al., *Creep behavior of Ti–6Al–4V and a comparison with titanium matrix composites*, Mater. Sci. Eng. A 428 (1–2) (2006) 319–326.
[145] S. Karashima, H. Oikawa, T. Motomiya, *Steady-state creep characteristics of polycrystalline nickel in the temperature range 500 to 1000 C*, Trans. Jpn. Inst. Metals 10 (3) (1969) 205–209.
[146] Y. Kondo, et al., *High temperature creep properties of high purity chromium*, Tetsu-to-Hagané 78 (6) (1992) 947–954.
[147] M. Kvapilova, et al., *Creep behaviour and life assessment of a cast nickel–base superalloy MAR–M247*, High Temp. Mater. Processes 2019 (38) (2019) 590–600.
[148] T. Matsunaga, et al., *Creep Behavior of Commercially Pure Titanium at Low and Intermediate Temperatures*, ASM International, 2019.
[149] J.R. Stephens, W.D. Klopp, *High-temperature creep of polycrystalline chromium*, Journal of the Less Common Metals 27 (1) (1972) 87–94.
[150] T. Sugahara, et al., *Creep and mechanical behavior study of Inconel 718 Superalloy*, Mater. Res. 25 (2021) e20210280.
[151] Y. Zhang, et al., *High-temperature deformation and fracture mechanisms of an advanced heat resistant Fe-Cr-Ni alloy*, Mater. Sci. Eng. A 686 (2017) 102–112.
[152] K.-Y. Tsai, M.-H. Tsai, J.-W. Yeh, *Sluggish diffusion in co–cr–fe–mn–ni high-entropy alloys*, Acta Mater. 61 (13) (2013) 4887–4897.
[153] D.G. Shaysultanov, et al., *Phase Composition and Superplastic Behavior of a Wrought AlCoCrCuFeNi High-Entropy Alloy*, JOM 65 (12) (2013) 1815–1828.
[154] F.A. Mohamed, T.G. Langdon, *The transition from dislocation climb to viscous glide in creep of solid solution alloys*, Acta Metall. 22 (6) (1974) 779–788.
[155] O.N. Senkov, et al., *Microstructure and elevated temperature properties of a refractory TaNbHfZrTi alloy*, J. Mater. Sci. 47 (9) (2012) 4062–4074.
[156] M. Vaidya, et al., *Bulk tracer diffusion in CoCrFeNi and CoCrFeMnNi high entropy alloys*, Acta Mater. 146 (2018) 211–224.
[157] N. Larianovsky, et al., *Microstructure, tensile and creep properties of Ta20Nb20Hf20Zr20Ti20 high entropy alloy*, Materials 10 (8) (2017) 883.
[158] K.H. Lee, S.-K. Hong, S.I. Hong, *Precipitation and decomposition in CoCrFeMnNi high entropy alloy at intermediate temperatures under creep conditions*, Materialia 8 (2019) 100445.
[159] Y. Li, et al., *Rafting of γ' precipitates in a Co-9Al-9W superalloy during compressive creep*, Mater. Sci. Eng. A 719 (2018) 43–48.
[160] F. Spaepen, *A microscopic mechanism for steady state inhomogeneous flow in metallic glasses*, Acta Metall. 25 (4) (1977) 407–415.
[161] C. Zhang, et al., *Thermal activation in the Zr65Cu18Ni7Al10 metallic glass by creep deformation and stress relaxation*, Scr. Mater. 113 (2016) 180–184.
[162] S.W. Provencher, *CONTIN: a general purpose constrained regularization program for inverting noisy linear algebraic and integral equations*, Comput. Phys. Commun. 27 (3) (1982) 229–242.
[163] V. Khonik, et al., *Isothermal creep of metallic glasses: a new approach and its experimental verification*, Acta Mater. 46 (10) (1998) 3399–3408.
[164] D. Pan, et al., *Experimental characterization of shear transformation zones for plastic flow of bulk metallic glasses*, Proc. Natl. Acad. Sci. 105 (39) (2008) 14769–14772.
[165] X.-S. Yang, et al., *Multi-temperature indentation creep tests on nanotwinned copper*, Int. J. Plast 104 (2018) 68–79.
[166] W. Johnson, K. Samwer, *A Universal Criterion for Plastic Yielding of Metallic Glasses< ? format?> with a (T/T g) 2/3 Temperature Dependence*, Phys. Rev. Lett. 95 (19) (2005) 195501.
[167] Y. Xu, et al., *Experimental research on creep aging behavior of Al-Cu-Mg alloy with tensile and compressive stresses*, Mater. Sci. Eng. A 682 (2017) 54–62.
[168] H. Dieringa, N. Hort, K.U. Kainer, *Investigation of minimum creep rates and stress exponents calculated from tensile and compressive creep data of magnesium alloy AE42*, Mater. Sci. Eng. A 510–511 (2009) 382–386.
[169] Y. Li, et al., *Experimental investigation of tension and compression creep-ageing behaviour of AA2050 with different initial tempers*, Mater. Sci. Eng. A 657 (2016) 299–308.
[170] J. Wheeler, J. Michler, *Elevated temperature, nano-mechanical testing in situ in the scanning electron microscope*, Rev. Sci. Instrum. 84 (4) (2013).
[171] J. Wheeler, P. Brodard, J. Michler, *Elevated temperature, in situ indentation with calibrated contact temperatures*, Phil. Mag. 92 (25–27) (2012) 3128–3141.
[172] S. Verma, P. Sarkar, P. Pant, *Thermal drift in room temperature nanoindentation experiments: Measurement and correction*, J. Mater. Res. 36 (17) (2021) 3436–3444.
[173] Frost, H.J. and M.F. Ashby, *Deformation-mechanism maps: the plasticity and creep of metals and ceramics*. 1982.
[174] Z.C. Duan, A.M. Hodge, *High-temperature nanoindentation: New developments and ongoing challenges*, JOM 61 (12) (2009) 32–36.
[175] R. Goodall, T.W. Clyne, *A critical appraisal of the extraction of creep parameters from nanoindentation data obtained at room temperature*, Acta Mater. 54 (20) (2006) 5489–5499.
[176] J. Li, Q. Fang, P.K. Liaw, *Microstructures and properties of high-entropy materials: modeling, simulation, and experiments*, Adv. Eng. Mater. 23 (1) (2021) 2001044.
[177] G. Huang, et al., *Effects of lattice distortion and chemical short-range order on creep behavior of medium-entropy alloy CoCrNi*, Mech. Mater. 177 (2023) 104549.

[178] J.M. Cowley, *An approximate theory of order in alloys*, Phys. Rev. 77 (5) (1950) 669.
[179] D. de Fontaine, *The number of independent pair-correlation functions in multicomponent systems*, Applied Crystallography 4 (1) (1971) 15–19.
[180] L. Xu, et al., *Decoupling the chemical-ordering-dependent dislocation and diffusion contributions to creep in multi-principal element alloy*, Materials Research Letters 13 (2) (2025) 122–130.
[181] A. Kumar, et al., *Prediction of creep degradation in Fe-Cr-Ni single-crystal alloys for high-temperature applications: a molecular-dynamics and machine-learning approach*, Mechanics of Time-Dependent Materials 29 (1) (2025) 8.
[182] J. Gao, et al., *Effect of Cu-Rich phase growth on Creep Deformation of Fe-Cr-Ni-Cu Medium-Entropy Alloy: a phase Field Study*, Metals 13 (7) (2023) 1219.
[183] Y. Liu, et al., *Irradiation Hardening and Creep Modeling of High-Entropy Alloy at High Temperature and Dose*, Acta Mech. Solida Sin. (2025) 1–10.
[184] W.-L. Hsu, et al., *Clarifying the four core effects of high-entropy materials*, Nat. Rev. Chem. 8 (6) (2024) 471–485.
[185] J. Zhang, et al., *Zr diffusion in BCC refractory high entropy alloys: a case of 'non-sluggish' diffusion behavior*, Acta Mater. 233 (2022) 117970.
[186] J. Dąbrowa, M. Danielewski, *State-of-the-art diffusion studies in the high entropy alloys*, Metals 10 (3) (2020) 347.
[187] M. Vaidya, et al., *Phenomenon of ultra-fast tracer diffusion of Co in HCP high entropy alloys*, Acta Mater. 196 (2020) 220–230.
[188] J. Dąbrowa, et al., *Demystifying the sluggish diffusion effect in high entropy alloys*, J. Alloy. Compd. 783 (2019) 193–207.
[189] S. Zhao, et al., Effect of d electrons on defect properties in equiatomic NiCoCr and NiCoFeCr concentrated solid solution alloys, Phys. Rev. Mater. 2 (1) (2018) 013602.
[190] Y.N. Osetsky, et al., *On the existence and origin of sluggish diffusion in chemically disordered concentrated alloys*, Curr. Opin. Solid State Mater. Sci. 22 (3) (2018) 65–74.
[191] M. Mizuno, K. Sugita, H. Araki, *Defect energetics for diffusion in CrMnFeCoNi high-entropy alloy from first-principles calculations*, Comput. Mater. Sci 170 (2019) 109163.
[192] S.C. Middleburgh, et al., *Segregation and migration of species in the CrCoFeNi high entropy alloy*, J. Alloy. Compd. 599 (2014) 179–182.
[193] J. Kottke, et al., *Experimental and theoretical study of tracer diffusion in a series of (CoCrFeMn)100−xNix alloys*, Acta Mater. 194 (2020) 236–248.
[194] B. Xing, et al., *Short-range order localizing diffusion in multi-principal element alloys*, Scr. Mater. 210 (2022) 114450.
[195] S.S. Behara, A. Van der Ven, *Role of Short-Range Order on Diffusion Coefficients in the Li–Mg Alloy*, Chem. Mater. 36 (22) (2024) 11236–11245.
[196] B. Xu, et al., *Influence of short-range order on diffusion in multiprincipal element alloys from long-time atomistic simulations*, Phys. Rev. Mater. 7 (3) (2023) 033605.
[197] G. Sahragard-Monfared, et al., The influence of processing methods on creep of wrought and additively manufactured CrCoNi multi-principal element alloys, Acta Mater. 261 (2023) 119403.
[198] F. Junhong, Z. Weiqiang, *Simulation of bulk and grain boundary diffusion phenomena in a high entropy CoCrFeMnNi alloy by molecular dynamics*, Phys. Scr. 98 (3) (2023) 035006.
[199] M. Vaidya, et al., *Radioactive isotopes reveal a non sluggish kinetics of grain boundary diffusion in high entropy alloys*, Sci. Rep. 7 (1) (2017) 12293.
[200] B. Akdim, et al., *Predicting core structure variations and spontaneous partial kink formation for ½<111> screw dislocations in three BCC NbTiZr alloys*, Scr. Mater. 199 (2021) 113834.
[201] S. Yin, et al., *Ab initio modeling of the energy landscape for screw dislocations in body-centered cubic high-entropy alloys*, npj Comput. Mater. 6 (1) (2020) 110.
[202] T. Wang, et al., *Unraveling dislocation-based strengthening in refractory multi-principal element alloys*, npj Comput. Mater. 10 (1) (2024) 143.
[203] B. Chen, et al., *Trade-off between local chemical order and lattice distortion in affecting dislocation motion in NbTiZr multi-principal element alloys*, Acta Mater. 272 (2024) 119910.
[204] W. Lu, et al., *Chemical short-range-order induced multiscale strengthening in refractory medium entropy alloys*, Acta Mech. Sin. 40 (6) (2024) 223569.
[205] J.-H. Zhai, M. Zaiser, *Properties of dislocation lines in crystals with strong atomic-scale disorder*, Mater. Sci. Eng. A 740–741 (2019) 285–294.
[206] J. Li, et al., *Heterogeneous lattice strain strengthening in severely distorted crystalline solids*, Proc. Natl. Acad. Sci. 119 (25) (2022) e2200607119.
[207] Y. Chen, et al., *Irradiation hardening behavior of high entropy alloys using random field theory informed discrete dislocation dynamics simulation*, Int. J. Plast 162 (2023) 103497.
[208] M. Sudmanns, J.A. El-Awady, *The effect of local chemical ordering on dislocation activity in multi-principle element alloys: a three-dimensional discrete dislocation dynamics study*, Acta Mater. 220 (2021) 117307.
[209] Y. Su, S. Xu, I.J. Beyerlein, *Ab initio-informed phase-field modeling of dislocation core structures in equal-molar CoNiRu multi-principal element alloys*, Model. Simul. Mater. Sci. Eng. 27 (8) (2019) 084001.
[210] Y. Zeng, X. Cai, M. Koslowski, *Effects of the stacking fault energy fluctuations on the strengthening of alloys*, Acta Mater. 164 (2019) 1–11.
[211] D. Qiu, J. Wu, *γ-surface informed phase-field modeling on structures and properties of defects in FeCoNiMnAl alloys*, Comput. Mater. Sci 250 (2025) 113732.
[212] L.T.W. Smith, et al., *The effect of local chemical ordering on Frank-Read source activation in a refractory multi-principal element alloy*, Int. J. Plast 134 (2020) 102850.
[213] L.T. Fey, et al., *Transitions in the morphology and critical stresses of gliding dislocations in multiprincipal element alloys*, Phys. Rev. Mater. 6 (1) (2022) 013605.
[214] M.R. Jones, L.T. Fey, I.J. Beyerlein, *High temperature dislocation glide in the MoNbTi refractory multiprincipal element alloy*, Phys. Rev. Mater. 8 (1) (2024) 013604.
[215] H. Kim, et al., *Non-Schmid effects in a model refractory multi-principal element alloy: phase-field dislocation dynamics informed by atomistic simulations*, Materials Research Letters 12 (3) (2024) 190–198.
[216] M.R. Jones, P. Garg, I.J. Beyerlein, *Transitions in thermally activated glide mechanisms in the MoNbTaVW refractory multiprincipal element alloy up to 0.3 T m*, Phys. Rev. Mater. 8 (10) (2024) 103603.
[217] H. Zheng, et al., *Multi-scale investigation of short-range order and dislocation glide in MoNbTi and TaNbTi multi-principal element alloys*, npj Comput. Mater. 9 (1) (2023) 89.
[218] P.F. McNutt, et al., *Room temperature dislocation loop dynamics in body-centered cubic refractory multi-principal element alloys*, Comput. Mater. Sci 244 (2024) 113280.
[219] H. Zhai, et al., *Microstructure sensitivity of the low cycle fatigue crack initiation mechanisms for the Al0.3CoCrFeNi high entropy alloy: in-situ SEM study and crystal plasticity simulation*, Int. J. Fatigue 176 (2023) 107871.
[220] X. Ma, et al., *In situ study on plastic deformation mechanism of Al0.3CoCrFeNi high-entropy alloys with different microstructures*, Mater. Sci. Eng. A 857 (2022) 144134.
[221] Y. Zhang, et al., *A study on the microstructure and mechanical behavior of CoCrFeNi high entropy alloy fabricated via laser powder bed fusion: Experiment and crystal plasticity finite element modelling*, Mater. Sci. Eng. A 893 (2024) 146111.
[222] P. Lu, et al., *Effects of stress states and strain rates on mechanical behavior and texture evolution of the CoCrFeNi high-entropy alloy: Experiment and simulation*, J. Alloy. Compd. 851 (2021) 156779.
[223] C. Li, et al., *Crystal plasticity model analysis of the effect of short-range order on strength-plasticity of medium entropy alloys*, Metals 12 (10) (2022) 1757.
[224] Q. Han, et al., *Temperature-dependent fatigue response of a Fe44Mn36Co10Cr10 high entropy alloy: a coupled in-situ electron microscopy study and crystal plasticity simulation*, Int. J. Fatigue 151 (2021) 106385.
[225] W. Lu, et al., *A hierarchical multiscale crystal plasticity model for refractory multi-principal element alloys*, Int. J. Mech. Sci. 271 (2024) 109140.
[226] H. Fang, et al., *Experimental and crystal plasticity finite element study of dynamic shear behavior of CoCrNiSi0.3 medium-entropy alloy*, J. Mater. Res. Technol. 32 (2024) 2815–2829.
[227] L. Yu, et al., *Stress gradient versus strain gradient in polycrystalline high entropy alloy revealed by crystal plasticity finite element simulation*, Acta Mech. Sin. 41 (10) (2024) 124267.
[228] N. Gerel-Erdene, Y. Aoyagi, *Crystal Plasticity Finite Element simulation considering Geometrically Necessary Dislocation distribution for Reproducing Mechanical Anisotropy of rolled CrMnFeCoNi High-Entropy Alloy*, Mater. Trans. 65 (9) (2024) 1008–1014.
[229] Z. Zhou, et al., *Experimental investigation and crystal plasticity modelling of dynamic recrystallisation in dual-phase high entropy alloy during hot deformation*, Mater. Sci. Eng. A 922 (2025) 147634.
[230] J.W. Bae, et al., *On the phase transformation and dynamic stress–strain partitioning of ferrous medium-entropy alloy using experimentation and finite element method*, Materialia 9 (2020) 100619.
[231] H. Zhai, et al., *On the plastic deformation mechanism of Al0.6CoCrFeNi high entropy alloy: In-situ EBSD study and crystal plasticity modeling*, Mater. Sci. Eng. A 915 (2024) 147108.
[232] X. Zhang, et al., *Temperature effect on tensile behavior of an interstitial high entropy alloy: Crystal plasticity modeling*, Int. J. Plast 150 (2022) 103201.
[233] T. Záležák, et al., *Creep strength variations related to grain boundaries in the equiatomic CoCrFeMnNi high-entropy alloy*, Scr. Mater. 249 (2024) 116165.
[234] S. Xiang, et al., *A deep learning-aided prediction approach for creep rupture time of Fe–Cr–Ni heat-resistant alloys by integrating textual and visual features*, J. Mater. Res. Technol. 18 (2022) 268–281.
[235] Y. Liu, et al., Predicting creep rupture life of Ni-based single crystal superalloys using divide-and-conquer approach based machine learning, Acta Mater. 195 (2020) 454–467.
[236] Y. Liu, et al., Descriptors divide-and-conquer enables multifaceted and interpretable materials structure–activity relationship analysis, Adv. Funct. Mater. 35 (26) (2025) 2421621.
[237] Y. Liu, et al., Machine learning assisted materials design and discovery for rechargeable batteries, Energy Storage Mater. 31 (2020) 434–450.
[238] Y. Liu, et al., Feature selection method reducing correlations among features by embedding domain knowledge, Acta Mater. 238 (2022) 118195.
[239] Y. Liu, et al., Data quantity governance for machine learning in materials science, Natl. Sci. Rev. 10 (7) (2023) 125.
[240] Y. Liu, et al., A general framework to govern machine learning oriented materials data quality, Materials Science and Engineering: r: Reports 166 (2025) 101050.
[241] Z. Yan, et al., *A microstructure-based constitutive model for creep rate and damage of oxide dispersion strengthened high-entropy alloy*, Eng. Fract. Mech. 306 (2024) 110199.
[242] S. Zafar, M.T. Ehsan, S. Das Suvro, M. Islam, M.N. Hasan, Effect of grain size and local chemical order on creep resistance in MoNbTaW refractory high-entropy

alloy: A molecular dynamics study, Modelling and Simulation in Mater. Sci. Eng. 34 (2026) 035013.
[243] T.M. Smith, et al., *A 3D printable alloy designed for extreme environments*, Nature 617 (7961) (2023) 513–518.
[244] C. Zhang, Y. Yang, *The CALPHAD approach for HEAs: challenges and opportunities*, MRS Bull. 47 (2) (2022) 158–167.
[245] Y. Li, et al., *Developing novel low-density high-entropy superalloys with high strength and superior creep resistance guided by automated machine learning*, Acta Mater. 285 (2025) 120656.
[246] Z. Rao, et al., *Machine learning–enabled high-entropy alloy discovery*, Science 378 (6615) (2022) 78–85.
[247] Y. Zhang, et al., *Phase prediction in high entropy alloys with a rational selection of materials descriptors and machine learning models*, Acta Mater. 185 (2020) 528–539.
[248] M. Zhang, et al., Creep behavior of high-entropy alloys: a critical review, Intermetallics 192 (2026) 109242.
[249] U.S. Department of Energy, Genesis Mission National Science and Technology Challenges. U.S. Department of Energy, 2026. Available online: https://www.energy.gov/documents/genesis-mission-science-and-technology-challenges.